Investigating ACE2 Localization in Respiratory Cilia and Characterizing Cilia Motion Phenotypes

by

Chenxiao Li

(Under the Direction of Shannon Quinn)

Abstract

Cilia are hair-like projections lining the respiratory tract that move microbes and debris out of the airways. The coordinated beating of cilia provides the driving force for mucociliary clearance, which is the primary defense mechanism of the lung. Cilia are also an important entry site for viral infection including SARS-CoV-2, which is the causative agent of the COVID-19 pandemic. SARS-CoV-2 enters host cells by interacting with angiotensin-converting enzyme 2 (ACE2) and transmembrane serine protease 2 (TMPRSS2) receptors, which are localized to respiratory cilia. The localization of ACE2 on these cilia has important implications in SARS-CoV-2 transmission and the development of therapeutic strategies to treat COVID-19. However, the specific localization of ACE2 in cilia and whether ACE2 plays a role in ciliary function remain unknown. To investigate the localization of ACE2 in cilia, we performed immunofluorescence staining and imaged with a super-resolution microscope using commercial ACE2 antibodies. We found that ACE2 localizes to the proximal region of cilia while TMPRSS2, an ACE2 sheddase, localizes to the distal region of cilia, which may in part explain the proximal distribution of the ectodomain of ACE2 on respiratory cilia. To study ciliary function, we built a large-scale video dataset of ciliary motion phenotypes under several categories (temperatures, drugs, and ACE2 manipulation). This validation dataset consists of 872 videos and ground-truth masks labelling the ciliary area. We also

calculated the ciliary beat frequency as a benchmark metric. Cilia segmentation is important for ciliary waveform analysis, which will help in the diagnosis of ciliopathies. We built a deep learning pipeline that incorporated Gabor filters into a the U-Net model for automated cilia segmentation. Our framework improved the performances of the baseline model in terms of Intersection over Union (IoU), accuracy, F1, and precision scores. Our work is crucial to understanding the precise nature of ACE2, SARS-CoV-2 pathogenesis, and ciliary motility.

INDEX WORDS: [Cilia, ACE2, TMPRSS2, image segmentation, cilia beat frequency, validation dataset]

Investigating ACE2 Localization in Respiratory Cilia and Characterizing Cilia Motion Phenotypes

by

Chenxiao Li

M.S., University of Georgia, 2023

B.S., Fudan University, China, 2013

A Dissertation Submitted to the Graduate Faculty of the
University of Georgia in Partial Fulfillment of the Requirements for the Degree.

Doctor of Philosophy

Athens, Georgia

2023

Investigating ACE2 Localization in Respiratory Cilia and Characterizing Cilia Motion Phenotypes

by

Chenxiao Li

Major Professor: Shannon Quinn

Committee: Jonathan Eggenschwiler
Russell Karls
Fred Quinn
Kaori Sakamoto
Ralph Tripp

Electronic Version Approved:

Ron Walcott
Dean of the Graduate School
The University of Georgia
August 2023

Dedication

This work is dedicated to my parents, Xia Liu and Zhengping Li.

Acknowledgments

First, I would like to express my sincere gratitude to my wonderful mentor, Dr. Shannon Quinn, for taking me in as a graduate student working in his lab when my former advisor left UGA. His passion and enthusiasm in science and research always inspires me. I also want to thank Dr. Jonathan Eggenschwiler for allowing me to work in his lab for bench work. I would like to thank Dr. Karl Lechtreck for letting me use his high-speed video microscope constantly. I also want to thank Dr. Muthugapatti K. Kandasamy for teaching me how to use super-reslution and confocal microscopes and helping to solve any imaging issues.

I would like to acknowledge the rest of my committee, Dr. Russell Karls, Dr. Fred Quinn, Dr. Kaori Sakamoto and Dr. Ralph Tripp, for their feedback and guidance.

It has been a great pleasure to work with all members from the Quinn Research Group. I would also like to thank Anna, Michael and Kush from Dr. Eggenschwiler's group for helping out with the bench work. I sincerely thank Drs. Xia Guo, Xiaobing Cui, and Kun Dong for helping me settle down when I first arrived here in Athens, Georgia.

Last but not least, I want to thank all my friends and family members for supporting me along the way. I want to thank my fiancé, Nathan Chasen, for being here for all the ups and downs. He has been my biggest support throughout this journey. I would not make it without them.

Contents

Acknowledgments **v**

List of Figures **viii**

List of Tables **x**

1 Introduction **1**

1.1 Introduction 1

1.2 Overview of dissertation 2

2 Literature Review **4**

2.1 Angiotensin-Converting Enzyme 2 and Motile Cilia 4

2.2 A Review of Assessing Ciliary Characteristics and Segmentation 11

2.3 Conclusions 29

3 The Localization of ACE2 in Respiratory Cilia **30**

3.1 Introduction 30

3.2 Methods 32

3.3 Results 35

3.4 Discussion 38

3.5 Supplementary Information 42

4 Constructing a Validation Dataset of Ciliary Motion Phenotypes **56**

4.1 Introduction 56

4.2 Methods 60

4.3 Results 65

4.4 Discussion 69

5 Gabor Filter Incorporated U-Net for Cilia Segmentation **73**

5.1 Introduction 73

5.2 Related Work 75

5.3 Methodology 77

5.4 Experiments 82

5.5 Discussion 84

5.6 Supplementary Information 87

6 Conclusions **91**

Bibliography **93**

List of Figures

2.1 ACE2 four isoforms. 7

2.2 Schematic structure of a cilium 13

2.3 Normal ciliary beat cycle. 14

2.4 Schematic of a U-Net architecture (1). 18

3.1 Representative immunofluorescence staining of ACE2 and cilia marker acetylated α-tubulin (ACTUB) in ferret and mouse trachea. 47

3.2 Immunofluorescence analysis of ACE2 in the trachea from WT and ACE2 KO mice. . 48

3.3 ACE2 localizes to cilia in mouse tracheal epithelial cells (MTECs) at an air-liquid interface (ALI). 49

3.4 Epitope-tagged forms of ACE2 lentivirus packing. 50

3.5 Immunofluorescence analysis of V5-tagged (C-terminus) forms of ACE2 on cilia. . . . 51

3.6 Immunofluorescence analysis of HA-tagged forms of ACE2 on cilia from mouse epithelial cells *ex vivo* and *in vitro*. 52

3.7 TMPRSS2 localizes to the distal region of cilia. 53

3.8 ACE2 and TMPRSS2 localizes to cilia and extends through microvilli. 54

3.9 Model for ACE2 localization in cilia. 55

4.1 Example of tracking a full cycle of a cilium. 63

4.2 Example of cilia density determination. 64

4.3 Sample videos of cilia motion and their ground-truth masks. 65

4.4 Cilia dataset statistics. 66
4.5 CBF analysis at different temperatures. 67
4.6 Analysis of the effects of selected drugs on CBF relative to control. 69
4.7 ACE2 shRNA effects on ciliary beat frequency. 70

5.1 Example of a cilia image (left) and its ground-truth mask (right). 74
5.2 Gabor filter bank 79
5.3 Illustration of GFs applied to a sample cilia patch. 80
5.4 Confusion matrix 81
5.5 The visual illustration of filtered outputs of cilia images. 83
5.6 The visual comparison of cilia segmentation outputs. 85
5.7 Segmentation results during the training process. 86
5.8 Cilia and non-cilia distribution. 87

List of Tables

2.1 ACE2 isoforms and transcript variants. 8

2.2 Validation of ACE2 localization in airway using ACE2 antibodies 9

2.3 Comparison of various cilia segmentation techniques 20

2.4 Parameters for the quantitative assessment of cilia 25

2.5 Software tools for analyzing cilia parameters 28

3.1 Antibodies and fluorophores used in these studies 42

3.2 Primers sequences for ACE2 lentivirus construction 43

3.3 Primer sequences for ACE2 knockout mouse genotyping 43

4.1 Drug list 60

4.2 Working concentration and incubation time for drugs 62

4.3 Effects of drugs on CBF 68

5.1 The number of images and masks for training, validation, and testing 78

5.2 Selected Gabor filters 82

5.3 Performances of Gabor U-Net models over the cilia dataset 84

Chapter 1

Introduction

1.1 Introduction

The coronavirus disease 19 (COVID-19), caused by SARS-CoV-2, has been responsible for a worldwide pandemic causing over 768 million cumulative cases and 6.9 million deaths as of July 2023 [1]. COVID-19 is a severe infectious disease first reported in December 2019 in Wuhan, China (2). SARS-CoV-2 enters host cells by interacting with angiotensin-converting enzyme 2 (ACE2) and transmembrane serine protease 2 (TMPRSS2) receptors in host cells (3). ACE2 is a transmembrane protein found on the surface of many cell types. ACE2 plays an important role in regulating blood pressure and renal function.

Recent studies have shown that ACE2 plays an important role in mediating the infection of SARS-CoV and SARS-CoV-2 (4; 5; 3). There are four known isoforms of ACE2 and a soluble form of ACE2 lacking the transmembrane collectrin domain (6). ACE2 localizes to the respiratory cilia (7; 8). A recent study reported a novel ACE2 isoform named short ACE2, which localizes mainly to the apical region of cells (9). The specific expression and localization of ACE2 isoforms in cilia have not yet been investigated in respiratory cilia. SARS-CoV-2 infection disrupts cilia function, impairing the lung from trapping and clearing out the virus (10; 8; 11). However, whether ACE2 affects ciliary function and motility remains unknown.

[1] `https://covid19.who.int/`

Cilia are hair-like structures found on the surface of eukaryotic cells in vertebrates. Cilia participate in many biological processes such as fluid movement and cell locomotion. The synchronized beating of cilia is an important biological function in cells and vertebrates. In the airway, motile cilia beat in a coordinated manner to propel the pathogens and debris out of the airway. The coordinated beating of cilia plays a key role in maintaining effective mucociliary clearance (MCC), which is the primary innate defense mechanism of the lung (12). Defects in cilia can cause disorders known as ciliopathies, characterized by structural or functional abnormalities in cilia. Therefore, the effective analysis of ciliary function is critical in the diagnosis of ciliopathies. The functional analyses of cilia, including ciliary beat frequency (CBF) and ciliary beat pattern (CBP), are critical in biological studies and the diagnosis of ciliopathies. CBF can be calculated using automated methods such as fast fourier transform (FFT) or optical flow (13; 14; 15). However, the beat pattern of cilia is mainly analyzed manually, which is error-prone and time-consuming. Also, CBF measurement protocols are not standard so that metric can also vary.

Currently, the assessments of ciliary function and characteristics remain challenging, and a fundamental part of overcoming this challenge is effective cilia segmentation. In recent years, the rapid development of machine learning (ML) and deep learning (DL) algorithms has enabled great progress on automated cilia detection and segmentation (16; 17; 18; 19). A large-scale dataset is important for researchers to build model benchmarks and compare state-of-the-art methods. Currently, there is no open source dataset of ciliary motion. In this work, we built a large-scale validation dataset of ciliary motion phenotypes under different categories: temperatures, drugs, and ACE2 manipulation.

1.2 Overview of dissertation

In this dissertation, I investigate the localization of ACE2 in airway cilia and characterize ciliary motion phenotypes. This dissertation is presented in 5 chapters.

The second chapter is a literature review of the present knowledge of ACE2 and computational studies of cilia. I describe the structure and function of ACE2, and the current knowledge of the interaction of ACE2 and cilia. In the second part of the literature review, I describe image segmentation techniques in-

cluding traditional methods and deep-learning based methods. I also summarize computational methods to quantify cilia characteristics.

In Chapter 3 of this dissertation, I investigate ACE2 localization on airway cilia. Current studies on the specific localization of ACE2 on cilia and epithelial cells have reported conflicting results. Utilizing super-resolution microscopy, we demonstrate that Ecto-ACE2 localizes to the proximal region of cilia while Cyto-ACE2 localizes to cilia but is also enriched in the proximal region. In addition, we engineered epitope-tagged forms of ACE2 for ACE2 isoform 1 and 2 and found similar localization pattern of Ecto- and Cyto- ACE2. TMPRRS2, the sheddase of ACE2, localized to the distal region of cilia, which in part explains the distribution of Ecto-ACE2 on the proximal compartment of cilia only, and Cyto-ACE2 on whole cilia.

In Chapter 4, I describe construction of a large-scale validation dataset of ciliary motion phenotypes. I treated cilia with different stimuli (drugs, temperatures, ACE2 manipulation) and recorded cilia motion with a high-speed video microscope at 250 frames per second. I also generated ground-truth masks labelling ciliary area. As a benchmark, we calculated the CBF and presented the work of the quantitative analysis of cilia characteristics.

In Chapter 5, I propose a deep-learning framework of incorporating Gabor filter with the U-Net model for cilia segmentation.

Lastly, I summarize the work completed in this dissertation and provide future directions.

Chapter 2

Literature Review

2.1 Angiotensin-Converting Enzyme 2 and Motile Cilia

The COVID-19 pandemic, caused by the novel coronavirus SARS-CoV-2, has had an enormous impact on public health worldwide. Severe acute respiratory syndrome virus 2 (SARS-CoV-2), the causative agent of COVID-19, was shown to utilize the angiotensin converting enzyme-2 (ACE2) receptor for host cell entry. ACE2 is a zinc metalloenzyme and carboxypeptidase found on the surface of many cell types such as lung alveolar epithelial cells and enterocytes. Recent studies have shown that ACE2 is localized to respiratory cilia (7; 8), which are an important site of the infection. In recent years, ACE2 has become a promising target for the treatment and prevention of COVID-19. Numerous efforts have been made to research ACE2 in order to tackle SARS-CoV-2 globally.

ACE2 is cleaved by transmembrane serine protease 2 (TMPRSS2) to relase the ectodomain of ACE2 (20). The spike (S) protein of SARS-CoV-2 uses TMPRSS2 for S protein priming (3). Both ACE2 and TMPRSS2 are found localized to airway cilia (7; 21; 8). Respiratory cilia are important components of MCC, which is the primary innate defense mechanism of the lung (12). In this review, I provide a summary of the current knowledge of ACE2 localization respiratory cilia and its connection to SARS-CoV-2.

2.1.1 ACE2 structure and function

ACE2 is a type I membrane glycoprotein encoded by the ACE2 gene, which is located on the X chromosome (Xp22.2). ACE2 is 110-120 kD, with an N-terminal catalytic domain (amino acids 1-740) on the extracellular surface, a hydrophobic transmembrane region (amino acids 741-762), and a short C-terminal domain (amino acids 763-805) (22). ACE2 functions in regulating the renin-angiotensin system (RAS). ACE2 and ACE share 42% amino acid identity in the N-terminal extracellular catalytic domain (23). ACE2 converts angiotensin II (Ang II) to Ang 1-7, or generates Ang 1-9 from Ang I (24). As a negative regulator, ACE2 inactivates RAS to maintain homeostasis (25; 26).

ACE2 is expressed on the surface of many cell types, but ACE2 can be shed from the membrane, which releases soluble ACE2 (sACE2) in the circulation (27; 28). ACE2 shedding is induced by ADAM17, a disintegrin and metallopeptidase domain 17 (ADAM17) between the residues 716 and 741. The soluble form of ACE2 is 555 amino acids. TMPRSS2 also cleaves ACE2 by removing a C-terminal fragment of ACE2 (20; 29).

ACE2 plays an important role in the cardiovascular system as a component of RAS, which regulates cardiovascular function and can influence the development of cardiovascular disorders. The catalytic activity of ACE2 can form Ang 1-7 by hydrolyzing Ang II, which acts on Ang II Type I Receptor (AT1R) to cause increased blood pressure (30). In addition, upregulated Ang II is involved in the development of hypertension and heart failure (31). In contrast, Ang 1-7 increases cardiac baroreflex sensitivity and decreases blood pressure (32; 33). In ACE2-deficient mouse models, alterations in cardiovascular functions are associated with the genetic background of the mice (34; 35). For example, ACE2-deficient mice on the C57BL/6 background exhibited modestly elevated blood pressure. ACE2-deficient mice on the 129/SvEv background showed normal blood pressure (34). With Ang II infusion, significantly higher blood pressure was observed in ACE2 deficient mice. On the other hand, ACE2 overexpression in myocardial cells of transgenic mice is correlated with ventricular tachycardia and fibrillation (36). Upregulated ACE2 has been observed in failing human heart ventricles (37). ACE2 overexpression in the central nervous system

blunted Ang II-induced hypertension via regulating AT1, AT2 and Mas receptor subtypes (38). Therefore, ACE2 plays a protective role in the development of hypertension.

ACE2 also protects against renal disease progression, as experimental studies showed that ACE2 KO mice are more susceptible to kidney injury in the type 1 diabetes model and develop glomerulosclerosis (39; 40). Zhong *et al.* treated Ang II-infused wild-type mice with recombinant human ACE2 and found normalized renal oxidative stress and Ang II levels (41).

2.1.2 ACE2 isoforms

There are four isoforms of ACE2, translated from 6 different transcript variants (transcript variant 1: NM001371415.1, transcript variant 2: NM021804.3, transcript variant 3: NM001386259.1, transcript variant 4: NM001386260.1, transcript variant 5: NM001388452.1, transcript variant 6: NM001389402.1) (42). In addition, there is a soluble form of ACE2. ACE2 isoform 1, also the full-length ACE2, contains 805 amino acids. ACE2 isoform 2, composed of 786 amino acids, is the full length ACE2 with a truncation at the C-terminal domain and lacking the collectrin homology domain. ACE2 isoform 3, consisting of 694 amino acids, is 95 % identical with ACE2 isoform 1 and contains deletions in the transmembrane and collectrin domain. ACE2 isoform 4, known as short ACE2 or dACE2, lacks the carboxypeptidase activity with the SARS-CoV-2 binding site (Figure 2.1). ACE2 isoforms and the transcript variants are summarized in Table 2.1.

Blume and colleagues utilized quantitative PCR (qPCR) to quantify the expression levels of ACE2 full-length and short isoforms (9). The expression level of full-length ACE2 is higher than short ACE2 in most tissues except the kidneys. In another study, Manna and colleagues investigated two ACE2 isoforms: Isoform 1 and Isoform 2. Both isoforms are detected during the differentiation of human nasal epithelial cells, with ACE2 isoform 1 in higher abundance and ACE2 isoform 2 in lower abundance (43). The authors also analyzed a predicted transcript variant (XM_011545551), but this variant record has been removed by NCBI and thus is not discussed here. Interestingly, Manna *et al.* noticed the different localization patterns of different isoforms in U2os cells recognized by an ACE2 N-term antibody (ProSci, 3227) and a C-term

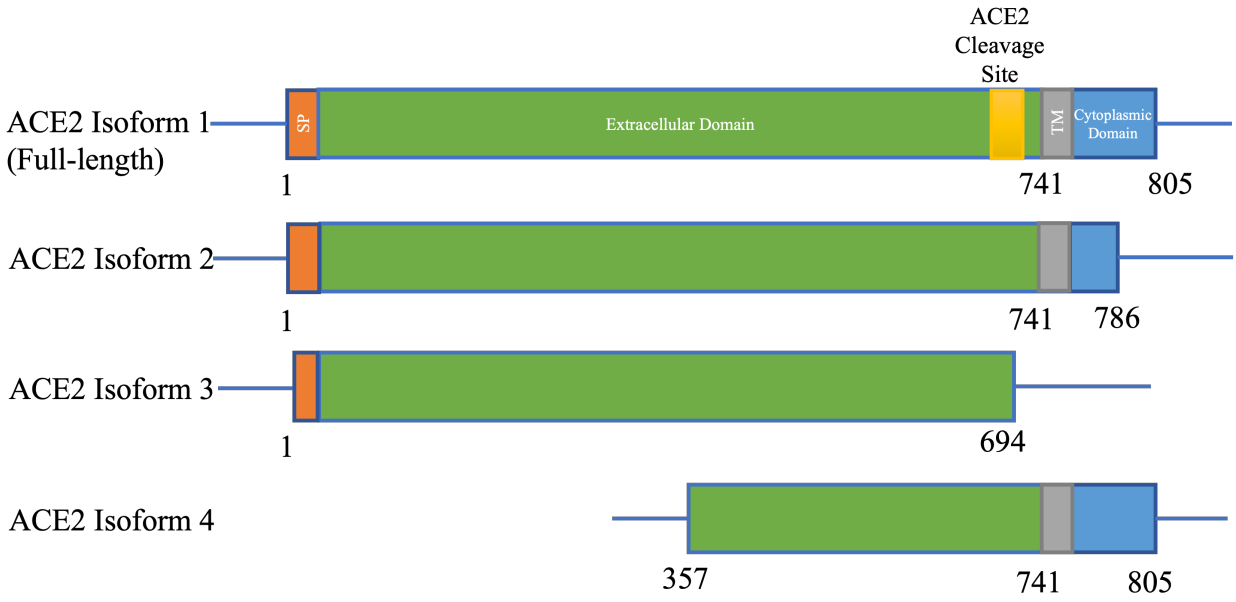

Figure 2.1: ACE2 four isoforms. ACE2 isoform 1, also known as the full-length ACE2, contains 805 amino acids. The extracellular sequence contains the carboxypeptidase domain while the cytoplasmic domain (762–805) contains the collectrin homology domain. ACE2 isoform 2 is the full length ACE2 with a truncation at the C-terminal domain and lacking the collectrin homology domain. ACE2 isoform 3 contains deletions in the transmembrane and collectrin domain. ACE2 isoform 4, known as short ACE2 or dACE2, lacks the carboxypeptidase activity with the SARS-CoV-2 binding site.

antibody (Invitrogen, MA5-32307). The different localization patterns of these isoforms might reflect differences in trafficking and translational processes.

2.1.3 ACE2 distribution and localization

ACE2 is distributed throughout the human body, with the most abundant expression in the kidney, testis, intestines, and heart (4; 44; 45). Harmer and colleagues used real-time PCR to show that transcribed ACE2 is expressed in 72 human tissues (46). They also confirmed that ACE2 is highly expressed in renal, cardiovascular, and gastrointestinal tissues. Hikmet *et al.* analyzed ACE2 expression profiling in over 150 cell types using multiple techniques and found that ACE2 was mainly expressed in enterocytes, renal

Table 2.1: ACE2 isoforms and transcript variants.

ACE2 isoforms	Transcript variants	Length (amino acids)
ACE2 Isoform 1	NM_001371415.1, NM_021804.3	805
ACE2 Isoform 2	NM_001386259.1	786
ACE2 Isoform 3	NM_001386260.1, NM_001389402.1	694
ACE2 Isoform 4	NM_001388452.1	459

tubules, and cardiomyocytes. In the lung, ACE2 expression is limited to a few subsets of cells (47). Ortiz *et al.* examined ACE2 expression in the human respiratory tract using single-cell RNA sequencing and showed that ACE2 is mostly detected in the sinonasal cavity and pulmonary aleveoli. In addition, they found ACE2 localized to the apical surface of aleveolar type II cells (48).

Previous studies showed that ACE2 localizes to the apical membrane of polarized cells (49). ACE2 also localizes to respiratory cilia, the main site of SARS-CoV-2 infection (7; 8). However, the specific localization of ACE2 on respiratory cilia has not been clarified. In the respiratory system, several studies have reported low mRNA levels of ACE2. Wang *et al.* reported low levels of ACE2 via both mRNA and protein measurements in the lung (50). However, Sungnak and colleagues found enriched ACE2 expression in epithelial cells across the airway (51). Different studies used different ACE2 antibodies to investigate the specific localization of ACE2 on respiratory cilia and ciliated cells from different tissue types. The specific localization of ACE2 on respiratory ciliated epithelia is summarized in Table 2.2.

2.1.4 ACE2 and SARS-CoV-2 infection

SARS-CoV-2 is the virus responsible for the COVID-19 pandemic. SARS-CoV-2 utilizes the ACE2 receptor on the cell surfaces to enter host cells. Specifically, the S protein of SARS-CoV-2 binds to the catalytic component of ACE2, after that, the S protein of the virus is primed by TMPRSS2, and the S2

Table 2.2: Validation of ACE2 localization in airway using ACE2 antibodies

ACE2 Antibody	Manufacturer	Immuogen (a.a.)	Localization	Sample Type	References
AF933	R&D	18-740	Motile cilia	*In vitro*	(9)
			Epithelial cells	*In vitro*	(5)
ab15348	abcam	788-805	Motile cilia	*In vitro*	(8)
			Motile cilia and epithelial cells	*In vivo*	(21)
			Apical epithelial cells	*In vitro*	(9)
			Apical epithelial cells	*In vivo*	(52)
			Motile cilia	*In vivo*	(7; 8)
			Microvilli	*In vitro*	(53)
HPA000288	Atlas	1-111	Microvilli	*In vitro*	(53)

subunit of S protein is released to fuse with the membrane (54). The binding of SARS-CoV and ACE2 leads to a down-regulation of ACE2, causing reduced conversion of Ang to Ang 1-7 and increased Ang II (55). In the case of SARS-CoV-2, however, ACE2 expression is increased upon infection then is reduced (56).

ACE2 functions in mediating SARS-CoV-2 infection (3; 57). SARS-CoV-2 infection induces ACE2 expression (58; 59). ACE2 is up-regulated in SARS-CoV-2 patients, as analysis of nasopharyngeal swab specimens showed 3.6 fold higher ACE2 expression than those from healthy controls. Soluble ACE2 plays a role in SARS-CoV-2 infection (60). In mouse models, wild-type mice are not susceptible to SARS-CoV-2 infection due to structural differences between human and mouse ACE2 (61). Also, mouse ACE2 does not bind efficiently to SARS-CoV-2, therefore, an ACE2-humanized mouse model is used for the studies of SARS-CoV-2 infection.

SARS-CoV-2 infection affects cilia function. Studies have shown that SARS-CoV-2 causes loss of cilia, trapped between the motile cilia, impeding ciliary motility functions (10; 62). SARS-CoV-2 infection is associated with reduced expression of FOXJ1 in airway epithelia, which is an important regulator of cilia motility and length (63; 10). The effective replication of the viruses requires motile cilia and cilia-generated fluid flow (8).

The SARS-CoV-2 receptor ACE2 can be upregulated by interferon (IFN) (58). After viral infection, an early IFN response is essential for host antiviral defense. However, severe COVID-19 patients exhibited impaired type I IFN activity (64). Scagnolari and colleagues reported that only the truncated ACE2 isoform was upregulated after IFN treatments *in vitro*, which might not facilitate SARS-CoV-2 infection (65). IL-13, a cytokine of type 2 immunity, can inhibit SARS-CoV-2 infection of airway epithelial cells (66). IL-13 can decrease the expression of ACE2 and increase the expression of TMPRSS2 (the sheddase of ACE2) on ciliated cells (6; 67).

2.1.5 The role of ACE2 in motile cilia

Current studies have shown that ACE2 localizes to the motile cilia and apical surface of epithelial cells (7; 8; 9). Also, SARS-CoV-2 viruses attach to motile cilia via ACE2 receptor and utilize motile cilia for spreading (8). However, whether ACE2 affects motile cilia function and MCC remains unknown. ACE2 KO mice showed a significant increase in Ang II levels in the lungs after acute lung injury induced by acid aspiration. Recombinant ACE2 protein can rescue lung function and edema formation after acid-treated lung injury (68). Does ACE2 play a role in regulating ciliary function? Could the loss of ACE2 affect ciliary beat frequency or MCC function? Further studies are needed to explore these questions.

2.1.6 ACE2 inhibitors

Since SARS-CoV-2 utilizes ACE2 receptor for cell entry, ACE2 becomes a promising therapeutic target for controlling COVID-19. ACE2, unlike its homologue ACE, cannot be blocked by ACE inhibitors (23). Huentelman and colleagues screened 140,000 small molecules and identified N-(2-aminoethyl)-1 aziridine-ethanamine (NAAE) as a novel ACE2 inhibitor (69). NAAE can modulate the catalytic activity of ACE2 and inhibit SARS-CoV S-protein-mediated cell fusion. MLN-4760 is another small molecule inhibitor of ACE2. Dales found that MLN-4760 at 100 nM did not affect S-protein-induced infection (70). Berenyiova and colleagues reported beneficial effects of MLN-4760 administered at a low dose in spontaneously hypertensive rats (SHRs) (71). Although MLN-4760 has a pro-obesogenic effect on

small artery function and angiogenesis, chronic low-dose MLN-4760-treatment induced NO and H_2S-mediated beneficial cardiovascular mechanisms.

Antihypertensive medicines such as angiotensin converting enzyme inhibitors (ACEIs) or angiotensin receptor blockers (ARBs) can regulate components of RAS. Several studies have reported that ACEI and ARBs can increase the expression of ACE2 (72; 3). The mechanism under which ACE2 up-regulation is correlated with ACEI and ARB treatment requires further investigation. Lee *et al.* found that the expression of ACE2 localized on respiratory cilia is not increased in patients (7). Wysocki and colleagues reported that captopril (an ACEI) and telmisartan (an ARB) do not increase ACE2 protein expression in kidney and lung epithelia (73). GLP-1, a Type 2 diabetes medicine, stimulates ACE2 expression (74).

2.2 A Review of Assessing Ciliary Characteristics and Segmentation

Cilia are hairlike organelles found on the surface of most cell types. In the respiratory system, the motile cilia on the respiratory epithelial cells beat in a rhythmic pattern, which propels pathogens and inhaled particles out of the airways. The coordinated beating of cilia plays a key role in maintaining effective MCC, which is the primary innate defense mechanism of the lung (12). Dysfunction of cilia causes severe diseases known as ciliopathies, including primary ciliary dyskinesia (PCD) and polycystic kidney disease (PKD), which lead to chronic lung infections and fluid-filled cysts, respectively (75; 76; 77).

There are several techniques for the diagnosis of cilia-related diseases: electron microscopy (EM), genetic test, the nasal nitric oxide (NO) test, and the ciliary motility test. EM can be used to detect the ultrastructural defects of the cilia. PCD patients with mutations in a heavy dynein chain gene can have normal cilia ultrastructure, but an abnormal cilia beat pattern (CBP) and low nasal NO (78). Therefore, the analysis of ciliary motility is essential for the diagnosis of ciliopathies. Recent technological advances have improved the assessment and measurement of ciliary motion. High-speed video (HSV) imaging has been applied for the analysis of ciliary beat frequency (CBF) and CBP (79; 80; 81). Optical coher-

ence tomography (OCT) has been used as a non-invasive approach for measuring CBF and liquid layer thicknesses *in vivo* (82). In this review, we provide an overview of ciliary characteristics and functions. We then provide an up-to-date review of the traditional and deep learning-based methods used for cilia segmentation and discuss the quantitative parameters for ciliary characteristics.

2.2.1 Cilia structure and function

The structure of a cilium is composed primarily of the axoneme and the basal body (83; 84). The axoneme consists of nine pairs of microtubules, either surrounding a central pair of microtubules ('9+2' arrangement) or without a central pair ('9+0' arrangement). Each outer doublet is composed of an A and B tubule, forming the outer ring. These microtubules are held together by cross-linking proteins such as inner sheath, nexin, and radial spokes (85). Axonemal dyneins, a family of cytoskeletal motor proteins, move along microtubules to drive the beat of cilia. There are two primary dynein complexes: outer dynein arms (ODAs) and inner dynein arms (IDAs). ODA drives beat frequency, while IDA regulates the waveform (86). The basal body participates in transporting proteins into the cilium (87). Figure 2.2 shows the schematic structure of a cilium.

Cilia can be broadly divided into two types: motile and non-motile (also known as primary cilia) (88). Historically, motile cilia are considered to have 9+2 microtubules, whereas primary cilia have a 9+0 arrangement. Recent studies report some exceptions and add two more types: 9+2 immotile and 9+0 motile (89; 87). In the embryonic ventral node, the 9+0 motile cilia, also known as nodal cilia, are essential in the formation of the left-right asymmetry of the body by rotating in the clockwise direction to generate a leftward fluid flow (90; 91). Non-motile cilia with 9+2 arrangement have been found on the cochlear hair cells in the mammalian auditory system (92; 93). These specialized primary cilia are known as kinocilia, which lack inner dynein arms and can passively swing in response to sound stimuli (92). Primary cilia have sensory function and play an important role in signal transduction (94). Motile cilia are mostly found on the apical surface of epithelial cells in the airways, brain, and oviduct (95; 96; 97). The coordinated beating pattern of motile cilia sweeps off the luminal contents over the epithelial surface and generate fluid flow.

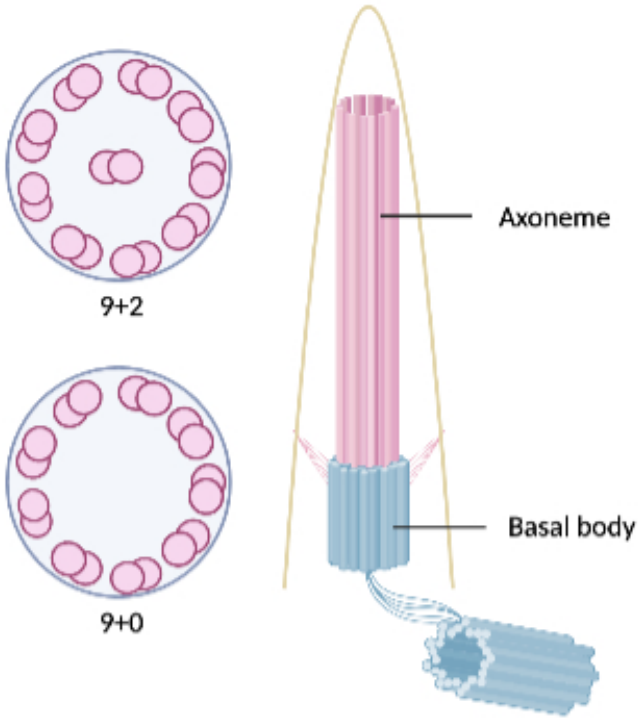

Figure 2.2: Schematic structure of a cilium

In the human respiratory tract, a ciliated epithelium has 200-300 motile cilia with a surface density around 5-8 cilia/μm^2 (98; 99; 100). The ciliary beat cycle has two phases: the effective stroke and the recovery stroke (Figure 2.3). During the forward stroke, cilia beat in a straight position to propel the fluid. During the recovery stroke, cilia move back to the original position by bending the proximal axoneme. The motile cilia beat in a coordinated manner to generate fluid flow for the transport of foreign particles and pathogens (12). Motile cilia lining the epithelial cells, the protective mucus, and the airway surface form MCC, which is the primary defence mechanism of the lung (101; 102). Normally, respiratory cilia beat at a frequency between 12 and 15 Hz, yielding MCC rates of 4 to 20 mm/min (103). Defects in MCC are associated with diseases such as cystic fibrosis (CF), chronic obstruction pulmonary disease (COPD), and sinusitis (104; 105; 106).

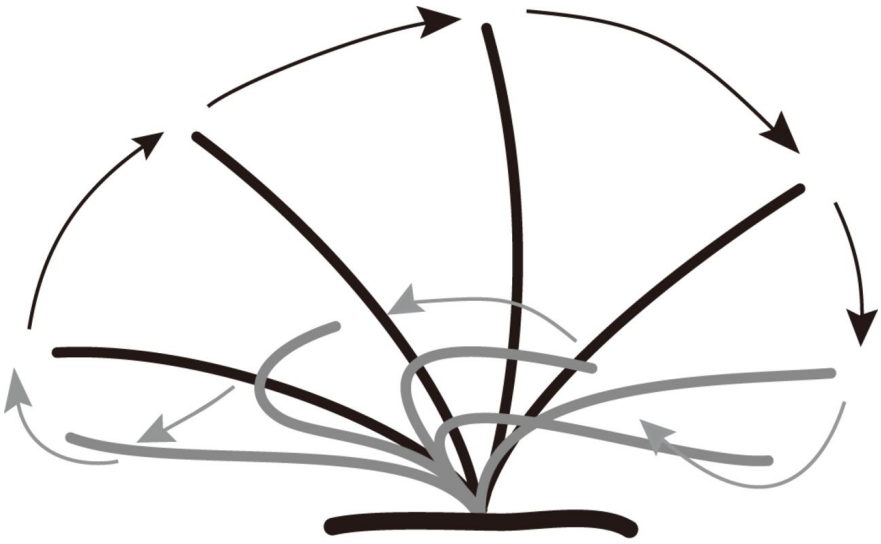

Figure 2.3: Normal ciliary beat cycle. A normal cycle consists of a beating stroke (black) followed by a recovery stroke (gray) (107).

2.2.2 Cilia segmentation

[1]

Image segmentation has many practical applications, including biomedical imaging, autonomous vehicles, facial recognition, and traffic control systems. There are two types of image segmentation: semantic segmentation, which is to label each pixel in a image with a corresponding class, and instance segmentation, which distinguishes between different instances of the same category. Semantic image segmentation is important for image analysis in removing background noise, improving precision, and area detection. It is also a challenging task in computer vision and digital image processing. Traditional approaches, such as thresholding and watershed, compare pixel values in order to achieve the segment map. With the development of deep learning and neural networks, there are many tools and architectures developed for image segmentation (1; 109; 110).

[1]Content of this section is based in part on my master thesis (108)

To characterize the morphology and function of cilia, the fundamental step is to identify cilia in images. Cilia segmentation is to detect and divide an image into groups of cilia and non-cilia. It is critical for further quantitative cilia analysis and characterizing motion patterns, which can help the identification of ciliopathies. Previously, biologists and clinicians detected and classified cilia manually, which is time-consuming and error-prone. In recent years, there have been attempts to segment cilia using traditional and deep learning-based methods (16; 111; 17; 112; 18; 113).

Traditional image segmentation methods for segmenting cilia

Traditional image segmentation techniques are based on thresholding, edge, region, and clustering to divide an image into areas of similar nature. Conventional methods produce fast and simple segmentation masks. To detect features or characteristics in images, a large number of studies have reported numerous, manually designed or handcrafted features with variations in scale and illumination. Handcrafted algorithms such as Gabor (114), Histogram of Oriented Gradients (HOG) (115), and scale invariant feature transform (SIFT) (116) are commonly used to extract features from images. The drawbacks of image segmentation with traditional methods are that they are not flexible and exhibit low accuracy. Moreover, they often require manual labor to fine-tune parameters for specific segmenting tasks.

For cilia segmentation, Zhang *et al.* utilizes two thresholding-based methods to segment fluorescent signal-labelled cilia (117). Specifically, they used the Transflour module and MultiWavelength Scoring (MWS) module within MetaXpress software. Both modules require the users to set parameters, such as size, intensity, and area to threshold cilia signal from the fluorescent images. Automated cilia detection in cells (ACDC) is a software for automated cilia detection in fluorescent images (111). To detect cilia, the authors applied the Gaussian filter as an adaptive thresholding method to binarize the cilia image. Then, the directional score parameter is applied as a threshold for optimizing cilia detection. This method achieved a high F1 score of 0.96 on fluorescently-labeled cilia images. CiliaQ is an open source software for automatic quantification of ciliary function in 2D and 3D images (16). The first step of CiliaQ workflow is to segment images into cilia and background using classic algorithms such as Renyi Entropy or Canny3D. However, this approach only provides a coarse segmentation and requires user input for manual correction.

Therefore, the above-mentioned thresholding methods have very limited application for the study of cilia. They can only be applied to fluorescent images where cilia are stained with a specialized antibody against Arl13b or acetylated α-tubulin. Those labeled cilia signals are acquired in a channel different from the rest of cells. For a live-cell setting such as differential interference contrast (DIC), thresholding methods work poorly to segment cilia. In a study analyzing cilia video data, Quinn *et al.* designed a pruning method to segment cilia and discard the noisy background (17). The prune algorithm is an intensity-based thresholding method that calculates the standard deviation of the time-varying changes at each pixel and sets an adaptive threshold to filter out background pixels. This method achieves a segmented map of cilia quickly with decent accuracy. However, the threshold of the prune method is adaptive and specific to each video set, therefore, it is not ideal for batch work.

Gabor filters (GFs), named after Dennis Gabor, are bandpass filters used in image processing. It is essentially a Gaussian modulated by a sinusoidal plane with frequency and orientation (114). After being convolved with GFs, patterns in images are highlighted at edges and points where the texture changes. GFs are extensively used for pattern analysis and feature extraction due to its reliability in localizing spatial-frequency domain properties. There are several advantages of GFs: first, the frequency and orientation representations of GFs are similar to those of the human visual system; second, GF can achieve fast and robust segmentation results by varying parameters according to the specific visual objects (118); third, GFs specialize in detecting small, localized stretches or blobs.

Traditional methods are often combined with classifiers such as random forest and Support Vector Machine (SVM) for image segmentation to increase accuracy and flexibility. Nguyen-Thanh *et al.* proposed to use an orientation adaptive GF to extract features and implement with k-nearest neighbor (k-NN), SVM and neural network-based classifiers for mitochondria segmentation (119). Their proposed method showed high accuracy in segmenting mitochondria. Since cilia can be viewed as a specialized hair-like texture with certain frequency and orientation, we proposed the use of GF for cilia feature extraction.

Deep learning-based segmentation methods for cilia

With the rapid advancements in deep learning, great efforts have been made in segmenting biological images. For cell segmentation, several bio-image segmentation tools, including StarDist (120), PlantSeg (121), Cellpose (110), and LABKIT(122), have achieved state-of-the-art segmentation performances. However, most of the state-of-the art segmentation methods require a large dataset with human-labelled ground-truth data for training.

Fully Convolutional Network (FCN), first introduced by Long and colleagues (123), can train end-to-end and use skip connections to enhance image segmentation. U-Net is a U-shaped architecture developed for biomedical image segmentation (1). The architecture of standard U-Net contains encoder layers and decoder layers (Figure 2.4). The encoder block reduces the spatial dimensions of the image, while the decoder repairs the details in the spatial dimension of the image. However, the drawback of U-Net is that it fails to separate objects when they are crowded or overlapped. The usage of skip connections would need redundant information, causing training overhead. Ram and colleagues introduced convolutional neural random forest classifier to classify the primary cilia in fluorescence images. Input images are fed in a CNN model with the U-Net architecture, and then the learned features are passed to the random decision forests classifier. Their approach achieved the F_β - score of 0.9102, outperforming the k-means and multi-layer perceptron (MLP) classifiers (124). Gupta *et al.* proposed to use a 2-D CNN model derived from the LeNet architecture to detect cilia automatically in low resolution transmission electron microscopy (TEM) images, which can significantly increase the AUC to 0.71 and reduce the false positive rate (125).

In the StarDist method, the cell nucleus is localized via star-convex polygons instead of bounding boxes, then the U-Net-based framework is trained to predict cell instances as polygons (120). The advantage of Stardist is that it can segment crowded cells with high accuracy. However, StarDist works for segmenting roundish-shape targets, thus it cannot be used to segment rod- or hair-like structures. PlantSeg uses a 3D U-Net to predict cell boundaries of dense plant tissues on images from confocal and light sheet settings (121). It achieves high accuracy in segmenting plant and non-plant samples. Cellpose is a deep learning-based pipeline utilizing a modified U-Net as a backbone for cell segmentation (110). The pre-trained models provided by the Cellpose platform were trained on a broad set of images with cells of different shapes

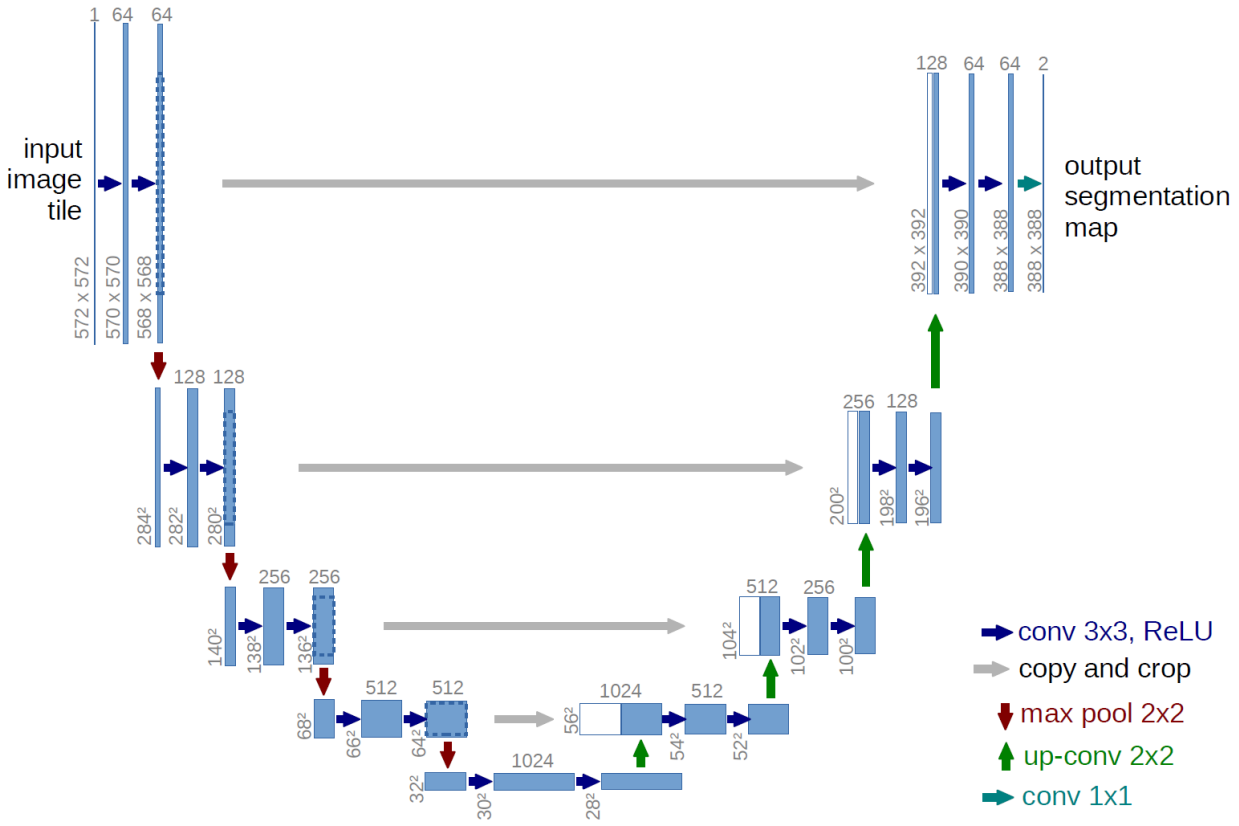

Figure 2.4: Schematic of a U-Net architecture (1). U-Net is a convolutional neural network with a U-shaped architecture consisting of an encoder (the left part), which extracts relevant features from images, and a decoder (the right part), which takes the extracted features and reconstructs a segmentation mask.

and types, and thus, cannot provide a generalized high quality cell segmentation. Cellpose 2.0 solves this problem by providing a zoo of pretrained models and a human-in-the-loop pipeline (126). This approach significantly reduced manual segmentation work to 100-200 regions of interest (ROIs) while achieving near-maximal performance.

Motile cilia are highly overlapping hair-like structures with low convexity and, hence, extremely difficult to segment. Furthermore, cilia motility videos are usually recorded as DIC images, which often achieves poor segmenting results due to low contrast. Quinn *et al.* developed a computational pipeline to classify cilia motion (17). In this framework, ciliary motion is considered as a dynamic texture, which can

be estimated by using an autoregressive (AR) model with the optical flow features. Lu *et al.* developed an end-to-end pipeline utilizing a densely-connected convolutional network (DenseNet) with 74 layers to automatically recognize cilia area (112). This proposed framework achieved an accuracy of 86.2% in cilia segmentation. Zain *et al.* modified Lu's model and built a fully Connected DenseNet with 103 layers. This model achieved a IoU score of 33.06% and a accuracy of 88.3% (18). In their most recent work, Zain and Miller combined zero-phase PCA sphering (ZCA) and Sparse Autoencoders (SEA), which served as low-level feature extraction, with U-Net (113). This new model achieved a 10% improvement with an IoU of 0.441 and an accuracy of 77% . Table 2.3 summarizes the above-mentioned cilia segmentation techniques.

To improve the performances of deep learning models, several studies incorporate low-level feature extraction to aid deep learning frameworks. Luan *et al.* proposed to incorporate Gabor filters into the deep convolutional neural networks (DCNNs) (127). By manipulating GF parameters, the proposed Gabor Convolutional Networks (GCN) framework effectively reduced the training complexity and improved performances over several benchmarks. Reyes and colleagues proposed an approach combining GF with U-Net for image segmentation (128). They applied the framework on two benchmark datasets, the ISLES 2018 dataset and the 2018 Atrial Segmentation Challenge dataset, and outperformed U-Net and other state-of-the-art architectures in mIoU and Dice scores. However, this work is relatively computationally expensive and inefficient, because the input contains the original dataset plus additional features extracted by a whole set of GFs. Some of the filters extract meaningless feature information compared to the other filters in the bank. An optimized GF bank with selected parameters is critical in the performance of the GF-embedded U-Net architecture for specific segmentation tasks.

2.2.3 Current techniques

Recent technologies enable researchers to visualize and quantify ciliary motion both *in vivo* and *ex vivo*, providing accurate assessment of ciliary characteristics. Confocal microscopy is commonly used for cilia morphology studies. HSV microscopy and photomultiplier and photodiode techniques can be used to

Segmentation Technique	Description	Results	Advantages	Disadvantages	Reference
Intensity-based thresholding	Separates images into cilia and non-cilia regions based on threshold values	-	Simple and fast calculations.	Threshold is adaptive and specific to each video	(17)
FC-Densenet 109	Fully Convolutional Dense Net with 109 layers	Accuracy: 0.862	Efficient in the parameter usage and feature reuse.	Data is replicated multiple times. High computational cost.	(112)
FC-DenseNet 103	Fully Convolutional Dense Net with 103 layers	IoU: 0.3306, Accuracy: 0.883, Precision: 0.5326	Efficient in the parameter usage and feature reuse.	Data is replicated multiple times. High computational cost.	(18)
U-Net	U-shaped architecture consists of a contracting path and an expansive path	IoU: 0.339, Accuracy: 0.759, Precision: 0.692, Recall: 0.501, F1: 0.529	Flexible and general approach. State-of-the-art image segmentation algorithm	High training time.	(113)
ZCA/SAE + U-Net	Adding ZCA and SAE for feature extraction to aid U-Net	IoU: 0.441, Accuracy: 0.767, Precision:0.661, Recall: 0.580, F1: 0.585	Adding low feature extraction improves U-Net model's performance	Difficult to find optimal parameters of ZCA and SAE	(113)

visualize cilia beat frequency and patterns. TEM analysis is used to detect ciliary ultrastructural defects. The diagnosis of PCD often involves a combination of tests: nasal nitric oxide (nNO) measurement, TEM, and HSV analysis (129; 130). In addition, optical coherence tomography (OCT) provides cross-sectional images of tissue reflectance, thus, it is being used for the quantitative assessment of cilia movement and mucus secretion (131). The application of current techniques are described below.

Confocal microscopy. Confocal microscopy is a specialized fluorescence microscopy technique with increased effective spatial resolution. With an additional Z-axis actuator, the 3D architecture of cilia can be acquired for morphological analysis and protein localization (16). Super-resolution microscopy is a powerful tool to analyze large protein complexes such as the ciliary base and centrioles in the tens of nanometers (132; 133; 134).

Transmission electron microscopy (TEM) is used to detect ultrastructural defects of cilia, which is regarded as the gold standard for PCD diagnosis. Most of the defects are found to be dynein arms-related (81.2%), while a small percentage are found to be associated with the central complex (CC) (18.8%) (135). In addition to two-dimensional micrographs generated from TEM, three-dimensional models have been developed. Burgoyne *et al.* (136) generated three-dimensional reconstruction of human respiratory cilia ultrastructure using TEM and subtomographic averaging. In recent years, cryo-electron microscopy (cryo-EM) has been used for the structural studies of motile cilia (137; 138). Cryo-electron tomography (cryo-ET) can localize and visualize protein complexes and their conformational changes within the cilia (139; 140; 141; 142). Although TEM is considered as a hallmark of PCD diagnosis by visualizing defects in ciliary ultrastructure, over 30 % of PCD patients have normal ciliary ultrastructure (143). Therefore, TEM is often combined with other tests in the diagnosis of PCD. TEM is also a time-consuming and expensive technique.

High-speed video (HSV) microscopy. HSV is the most commonly used technique for visualizing cilia motion and is applied as a diagnostic tool for ciliopathies such as PCD (81). Although HSV is not included in the American Thoracic Society (ATS) guidelines, it is included in the diagnostic guidelines by the European Respiratory Society (144). HSV enables the analysis of CBP and CBF, which are critical for

the diagnosis of PCD (130; 144). To access CBF and CBP, nasal brush biopsies are collected and viewed under a microscope and recorded with a high-speed camera at 120-500 frames/s. However, this diagnostic technique requires a panel of professional experts with specialized expertise to perform. A limited number of institutions are equipped with HSV, and the protocols for HSV testing and image processing vary from different institutions. Subtle changes in temperature and medium during recording can alter the results.

Optical coherence tomography (OCT). Most studies on ciliary motility relying on bright field microscopy are limited to investigating ciliary motion *in vitro* or *ex vivo*. OCT, however, utilizes interferometry to image the cross-sectional structures; therefore, it can be applied to ciliary motion detection and quantification *in vivo* (145; 146; 147; 148). In addition, OCT can capture fine heterogeneities in MCC such as the condition of the mucus and ciliary activity (131). Doppler OCT (D-OCT) can be used to quantify transverse flow and visualize CBP in vivo (149; 150). Micro-OCT (μOCT), engineered for capturing microanatomy, enables the observation of intact MCC apparatus and is applied to investigate ciliary motion and measure CBF (151; 82). In addition, μOCT can measure MCC parameters, such as airway surface liquid (ASL) and periciliary fluid (PCL) depth, with ultra-high resolution of 1-3 μm in tissue (152). He *et al.* (153) developed the phase resolved Doppler spectrally encoded interferometric microscopy (PRD-SEIM) system to visualize ciliary beating. The PRD method can provide the spatial and temporal information of cilia motion in the oviduct by analyzing the interferometric data. OCT with microscopic resolution (mOCT) utilizes temporal tissue fluctuation as contrast to enable the study of cell morphological changes and mucus transport (154). There are several drawbacks to OCT: first, it cannot avoid bulk motion and, therefore, requires certain steps to minimize phase noise in the system. Second, low resolution makes it not ideal for individual cilium detection. Third, the low-frame frequency due to limited laser scanning speeds makes it easy to have phase wrapping. Overall, OCT has the potential for *in vivo* endoscopic application in the clinics.

2.2.4 Cilia parameters

The characteristics of cilia are important hallmarks in evaluating the structure and function of cilia. Ciliary dysfunction causes diseases such as PCD and CF, which lead to chronic respiratory infection. Therefore, the effective quantitative analysis of ciliary parameters is critical in the diagnosis of cilia-related diseases. There have been numerous attempts to quantify cilia parameters such as CBF and length. Table 2.5 summarizes the automatic tools for analyzing cilia parameters. For primary cilia, the quantitative analysis is mostly fluorescence image-based, and parameters are related to morphology (such as length and volume). Acetylated α-tubulin (ACTUB) and ADP Ribosylation Factor Like GTPase 13B (Arl13b) are the most common cilia markers used for staining. For motile cilia, in addition to morphological evaluation, the analysis of ciliary motion is critical in estimating the ciliary function and motility. A normal ciliary beating cycle includes a strong beating stroke followed by a recovery stroke within the same plane, resulting in a fluid flow in the direction of the forward stroke (155). The rhythmic beating of neighboring cilia causes a velocity of the mucus layer around 1 mm per minute (99). Currently, the assessment of cilia beat waveforms remains challenging. Oltean *et al.* manually traced each beat cycle in order to estimate waveform parameters such as bend amplitude and stroke width (156). Bottier and colleagues analyzed cilia waveform using a series of mechanical metrics including power, force, and torque (157). The commonly used parameters in quantitatively describing ciliary motion and characteristics are discussed below and summarized in Table 2.4.

Ciliary beat frequency (CBF). CBF is a key parameter in determining the efficiency of MCC. In the human respiratory tract, human cilia beat in coordinated patterns at a frequency normally ranging between 10-15 Hz (99). CBF is driven by ATP signaling, which opens the calcium-activated K^+ channels and results in membrane depolarization (158; 159; 160). CBF can be counted manually by playing the cilia movie in slow motion. It can also be measured using algorithms such as Fast Fourier Transform (FFT) and video-kymography (161; 162; 163). CBF changes in response to temperature, infections, drugs, inflammatory factors, and age (164).

Kymograph requires the user to draw a line and analyze the gray level variations to estimate CBF. Kymograph analysis requires the user's input of regions of interest and calculates the frequency using Fourier Transform analysis of pixel intensity (165; 166). This method is relatively easy and allows the analysis of the whole beat pattern. Several studies measure CBF using optical flow (167; 17). Straßer and colleagues developed CilOCT, an open-source software for semi-automatic segmentation and analysis of ciliary muscle using OCT imaging data (168). CilOCT utilizes manual guiding selection for the automatic calculation of biometric parameters such as ciliary muscle apex and scleral spur. Sampaio and colleagues (169) developed a semi-automated software CiliarMove for CBF analysis. CiliarMove works on a user-selected ROI and calculating the FFT for each pixel, CBF is calculated using the following equation:

$$CBF = \frac{\text{number of frames per second}}{\text{average number of frames per beat}}$$

Kim *et al.* (15) combined optical flow, peak detection and FFT algorithms for signal frequency in order to estimate CBF. However, this method is sensitive to noise. Meste *et al.* (170; 166) developed a method consisting of a harmonic model and compressed spectrum for measuring CBF. Chen *et al.* developed a method analyzing the images with an iPhone camera and manually selecting the regions of interest (ROI) to analyze the CBF based on FFT (171). CiliaQ is a mostly automatic software for the quantification of ciliary parameters in 2D and 3D images (16). CiliaQ is composed of a three-step workflow: 1) CiliaQ Preparator, 2) CiliaQ Editor, and 3) CiliaQ. CiliaQ Preparator segments the images into cilia and background. CiliaQ Editior is a manual tool for correcting the segmentation. The final step CiliaQ is fully automatic for cilia reconstruction, quantification, and visualization. CiliaQ can be applied to semi-automatic or automatic segmentation and quantification of ciliary parameters in fixed samples. However, it cannot be applied to cilia motion analysis.

Ciliary beat pattern (CBP). The analysis of CBP is assessed by observing the ciliary beat cycle. Respiratory cilia beat forwards and backwards within the same plane, without a sideways recovery sweep (79). The 9+0 motile cilia (nodal cilia) move in a clockwise pattern, generating a leftward fluid flow for the left-right asymmetry during embryonic development (172; 173). CBP abnormalities are associated with

Table 2.4: Parameters for the quantitative assessment of cilia

Parameter	Description	Equation	Reference
Amplitude	Distance between the intersection points	distance(b-a)	(180)
Accumulated bend	The average of the absolute value of curvature multiplied by length	avg (C)*L	(181)
Avg bend amplitude	The average of bending amplitude, SD of angles averaged over a cycle	avg (SD(θ))	(156)
Velocity	Distance between subsequent intersection points divided by the time interval	$\frac{distance(b-a)}{time(c-d)}$	(180)
Curvature	Derivative of the angle with respect to arc length	$\frac{\partial\theta}{\partial s}$	(180; 182)
Avg curvature	Average curvature	avg (C)	(180; 181)
Force	Ciliary force in x-direction	Resistive Force Theory	(180; 183)
Stroke width	Max distance spanned by the waveform in the x-direction	max(x) – min(x)	(181; 178)
Metachronal wavelength	Metachronal wavelength on ciliated edges		

PCD mutations. Quantitative analysis of CBP can provide a sensitive and precise result that can be used for PCD diagnosis; however, there is no universal standard of parameters to quantify CBP. Chilvers and colleagues developed a scoring system with several markers: Immotility Index (IMI), Dyskinesia Score (DKS), and Percentage of dyskinetic edges (%DK) (174; 175; 176). Some studies used descriptive categories to distinguish different CBPs such as normal, immotile, stiff, circular, and asynchronous (174; 107). Reula and colleagues classified the beat pattern into three categories: normal, vibratile, and uncoordinated (177). Papon *et al.* determined 12 quantitative parameters such as beating angle and swept area to characterize CBP (178). Current studies involving CBP analysis still rely heavily on direct visualization and manual analysis. There are very limited open-source tools/methods for researchers to automatically analyze CBP (179; 156).

MCC rate. Normal mucociliary transport (MCT) produced by cilia beat in a rate of 4 to 20 mm/min (103). Decreased MCC can be caused by abnormal mucus production or ciliary dysfunction. Inefficient MCC has been observed in PCD, CF, pollutant exposure, and respiratory infection (184). PCD pa-

tients with abnormal ciliary motility have slow MCC, resulting in recurrent respiratory infections. The thickened or viscous mucus layer in asthma or CF patients can reduce the MCC rate (185; 102). The most common method to measure the clearance rate *in vivo* is to measure the clearance of inhaled, non-permeating, radiolabeled markers (104; 186). In experimental settings, MCC rate can be estimated by adding fluorescent beads to the bathing medium of airway cell cultures or *ex vivo* trachea. MCC rate can be measured by calculating the velocity of the fluorescent bead movement (187; 188).

Ciliary length. The length of cilia varies between 1-9 μm among different cell types (189; 190). Cilia length is associated with unique functional implications, ciliary mobility, and waveforms. Bottier and colleagues reported that short cilia under 2 μm did not beat periodically; cilia parameters (force, torque, and power), except for CBF, increased in proportion to length growth (157). Ciliary length changes in response to injury, diseases or pharmacological stimuli (191). Cilium length is regulated by multiple proteins and mechanisms such as the intraflagellar transport (IFT) machinery (192). Verghese *et al.* found that renal primary cilium length was increased dramatically after renal epithelial injury. Hypoxia and hypoxia-inducible factor 1α might regulate cilia length (193). Abnormalities in cilia length are associated with cilia-related diseases.

To measure ciliary length, the simplest and most common way is based on maximum intensity projection (MIP), which assumes the cilia are flat and takes the projection distance as the length. Researchers and biologists tend to use MIP to assess cilia length (194; 195; 16; 196; 197). The simple application of MIP enables it to be used for high throughput. However, this method neglects the angle of cilia and thus might underestimate the actual cilium length (189). The Pythagorean theorem (PyT) method overcomes this drawback by utilizing the projected distance (r) and the z-distance required to move the object plane from basal to distal to calculate the length (L):

$$L = \sqrt{r^2 + z^2} \tag{2.1}$$

However, this method assumes the cilia are straight and bending cilia might be underestimated. Due to the fact that cilia have a 3D orientation, both methods can potentially underestimate the length of bent or

angled cilia. For irregularly shaped cilia, 3D reconstruction is applied for measuring the length accurately (198; 189). However, this approach is labor-intensive and time consuming.

Cilia density. Cilia density is the number of cilia per unit surface area, also referred to as ciliation rate or ciliated cell density in some literature (199; 200). In the airways, each multiciliated cell is covered with 200 to 300 cilia, with a density of 5-8 cilia/μm^2 (201; 202; 100; 98). Decreased cilia density is an indication of cilia loss. To estimate cilia density in a DIC setting, Bottier *et al.* calculated the percentage of pixels in the ciliated edge that were darker than the background to estimate the density (163). However, this method fails to consider the diameter of cilia and is only a rough estimate of cilia density. Loiseau *et al.* calculated the cilia density by capturing the trajectories of the tips of cilia and then thresholding the binarized image (203). Ferreira *et al.* measured cilia density in 3D by constructing a spherical Voronoi diagram of cilia distribution (204). Minkeviciene *et al.* calculated cilia density as the cilia number divided by the length of the ventricle edge (205). The density of multiciliated cells is considered as cilia density in a number of studies (199; 200). For example, Pellicciotta *et al.* estimated the cilia density by calculating the fraction of area covered by beating cilia (199). This method underestimate cilia density by overlooking the unbeating cilia. To estimate the ciliation rate in fluorescent images, Yusifov *et al.* manually counted the number of cilia and ciliated cells based on the corresponding markers (206). Multiciliated cell density is an important parameter for cell maturation and cilia-generated flow. During cell differentiation, multiciliated cell density is increasing.

2.2.5 Machine learning and deep learning for cilia motion analysis

In recent decades, artificial intelligence and machine learning have been applied extensively in biomedical research and clinical diagnosis. Moreover, deep learning in computer vision has achieved great advancements. Algorithms such as Convolutional Neural Networks (CNNs) and Long Short Term Memory (LSTM) are used in cilia detection and classification (112; 19; 125; 124).

Chioccioli *et al.* (180; 212) developed a quantitative HSVM analysis system using machine learning algorithms to build a quantitative 'barcode' to classify PCD variants. They set a criteria of parameters

Table 2.5: Software tools for analyzing cilia parameters

Software	Cilia parameters	Applications	Availability	Reference
ACDC	Cilia count, length	Fluorescent images	Available upon request	(111)
BeatCilia	CBF	Cilia movies	In-house	(207)
CiliaCoordination	CBF, synchronization, segmentation, wave direction and length	Cilia movies	Open-source	(208)
CiliaFA	CBF	Cilia movies	open-source	(14)
CiliaQ	Length, intensity, volume, colocalization, bending index	Fluorescent images	open-source	(16)
CiliarMove	CBF	Cilia movies	Open-source	(169)
Multi-DDM	CBF, temporal coherence	Cilia movies	Open-source	(209; 210)
SAVA	CBF	Cilia movies	Commercial software	(211)

including ciliary beating amplitude, curvature, velocity, force, and curvature. Trinh *et al.* investigated an Artificial Neural Network (ANN) model and two other machine learning approaches for analyzing the behavioral pattern of Stentor roeselii (213). Even though ANN achieved the highest F1 scores among all three models, the best performance was only 59% accuracy.

In the model proposed by Quinn *et al.* (17), ciliary motion is considered as a dynamic texture, which can be estimated by using an autoregressive (AR) model with the optical flow features. This work, though largely automated, still depends on the user's input of manually-selected ROI. Lu *et al*. (112) improved this work by using deep learning approaches. They combined segmentation and classification to achieve a higher accuracy with a few hundred training epochs. To track ciliary motion, Almakady *et al.* (214) use the Gaussian Markov Random Fields (GMRF) model to generate the texture features, which are fed through the block-matching search technique to track ciliary motion trajectory. The tracking results are largely affected by the choice of neighborhood window size. The smaller window cannot be captured by the GMRF model, while the big window involves irrelevant pixels.

2.3 Conclusions

In this chapter, I reviewed current studies on ACE2 and characterizing cilia using traditional and state-of-the-art methods. The significance of ACE2 and its localization on cilia are also discussed. ACE2 appears to be a promising therapeutic target for treating and preventing COVID-19. Still, a fundamental understanding of ACE2 localization on cilia and its role in cilia function requires further research.

In the second section, I described the structure and function of cilia. A review of cilia parameters for characterizing cilia motion waveforms is provided. I discussed traditional methods and machine learning/deep learning-based methods for cilia segmentation. For characterizing cilia motion, there is a need for an open-source validation dataset of cilia motion phenotypes.

Chapter 3

The Localization of ACE2 in Respiratory Cilia

3.1 Introduction

COVID-19, caused by a novel coronavirus termed as SARS-CoV-2, was first reported in December of 2019 in Wuhan, Hubei province of China. It was soon transmitted all over the world and was declared a pandemic by WHO on March 11, 2020. In the third year of the COVID-19 pandemic, over 690 million people have been infected and over 6 million lives were lost globally (`https://www.worldometers.info/coronavirus/`). As SARS-CoV-2 mutates over time, updated vaccine boosters need to be developed to target the new variants and subvariants; thus, a strategy of fighting this virus at the level of host receptors has drawn more and more attention. Angiotensin-converting enzyme 2 (ACE2), which can be found on respiratory cilia, is the binding receptor of coronaviruses, including SARS-CoV and SARS-CoV-2, for cell entry (7; 215; 216). The spike protein of SARS-CoV-2 is responsible for this binding to the ACE2 receptor and allows SARS-CoV-2 to enter into host cells (217).

ACE2 is an inhibitor of the Renin-Angiotensin-Aldosterone System (RAAS), which plays an essential role in regulating blood pressure and renal function. ACE2 cleaves angiotensin I (Ang I) to generate Ang 1-9 and degrades Ang II to the vasodilator Ang 1-7 (218). ACE2 is widely expressed in many tissues and

organs including lung, intestine, kidney, and testis (219). In the respiratory system, ACE2 is abundantly expressed on the apical surface of airway epithelial cells (5) and type II alveolar cells of the lungs (220). ACE2 has an N-terminal catalytic domain on the extracellular surface and a short C-terminal cytoplasmic domain. There are four distinct protein isoforms of ACE2, translated from six ACE2 messenger RNA (mRNA) transcript variants (6; 42). ACE2 isoform 1 is the full-length ACE2, composed of 805 amino acids. The full-length ACE2 consists of an ectodomain (Ecto), a single transmembrane helix, and a cytoplasmic (Cyto) domain. ACE2 isoform 2 is a 786 amino acid protein with a distinct C-terminus. It is identical to the full-length ACE2 except that it is truncated at the cytoplasmic domain and lacks the collectrin homology domain (6). ACE2 isoform 3 consists of 694 amino acids, lacking the ADAM17 cleavage site. ACE2 isoform 4, also known as truncated ACE2 or short ACE2, lacks the N-terminal signal peptide and is unable to bind to SARS-CoV-2. Since the COVID-19 pandemic, numerous studies have analyzed the protein expression of ACE2 in tissues using commercially available anti-ACE2 antibodies (9; 7; 43). However, some of these studies did not distinguish between antibodies recognizing different epitopes, leading to conflicting results.

In addition, ACE2 can also be cleaved by type II transmembrane serine protease (TMPRSS2), which requires the arginine and lysine residues within ACE2 amino acids 697 to 716 for the cleavage to occur. The ectodomain of ACE2 is shed via proteolytic cleavage, causing the release of the soluble form of ACE2 into airway surface liquid (22). Blume and colleagues reported that the antibodies against Cyto-ACE2 (Abcam, ab15348) and Ecto-ACE2 (RD, AF933) localized mainly to the apical regions of the cells and motile cilia (9). Manna *et al.* showed that both the ACE2 N-term antibody (ProSci 3227) and ACE2 C-term antibody (ProteinTech 66699) displayed signals in the apical regions of ciliated cells. Their ACE2 C-term antibody showed plasma membrane signal on ciliated cells (43). Pinto and colleagues reported that antibody against the intracellular ACE2 domain (Abcam, ab15348) stained the base of microvilli, whereas an antibody against the extracellular ACE2 domain (Atlas, HPA000288) displayed signals that extended throughout the microvilli. They drew the conclusion that ACE2 and TMPRSS2 are localized to microvilli but are excluded from cilia, although the extracellular ACE2 domain antibody detected signals extending

throughout the microvilli (53). Different studies on this subject have used a variety of ACE2 antibodies; however, some of the commercial antibodies have uncertain specificity (221). Therefore, it is important to study the specific localization of ACE2 isoforms using ACE2 commercial antibodies with confirmed specificity and engineered ACE2 expression with epitope tags.

In this study, we utilized two commercial ACE2 antibodies to detect the specific localization of Ecto ACE2 and Cyto ACE2 in airway cilia. In addition, we engineered lentiviral tools for expression of ACE2 with epitope tags to investigate the specific localization of ACE2 isoforms. We found that the C-terminal domain of ACE2 isoform 1 localizes to the distal region of cilia, while the C-terminal domain of ACE2 isoform 2 localizes to the proximal compartment of cilia and apical regions of ciliated cells. We also showed that the N-terminal ACE2 domain, labeled with an HA tag, presents as sparse signals on cilia and the apical surface of cells. Finally, TMPRSS2, a protease that releases the Ecto-domain of ACE2, localizes to the distal region of cilia.

3.2 Methods

3.2.1 Ferret and mouse sample preparation

Ferret samples were kindly provided by Dr. Fred Quinn. ACE2 knockout mice were purchased from TACONIC (Model 18180). All procedures were performed in compliance with institutional guidelines and were approved by the University of Georgia (UGA)'s Institutional Animal Care and Use Committee. All animals were housed under conventional conditions in the animal care facilities of UGA. All experimental procedures were approved by the UGA Institutional Animal Care and Use Committees (IACUC).

3.2.2 ACE2 lentivirus package

ACE2 plasmid (pLEX307-ACE2-blast, 158449) was purchased from addgene. We inserted an HA tag at the N-terminus and a V5-tag at the C-terminus of the ACE2 gene. We also modified the C termi-

nus of ACE2 to have an isoform 1 (full-length) ACE2 lentivirus and isoform 2 ACE2 lentivirus. We replaced ACE2 with mNeon in the ACE2 plasmid as control. The modified ACE2 or control plasmids and lentivirus packaging vectors psPAX2 (`https://www.addgene.org/12260/`) and pMD2.G (`https://www.addgene.org/12259/`) were transfected into 293T cells using Lipofectamine™3000 Transfection Reagent (Cat L3000015, ThermoFisher, USA). Forty-eight hours after transfection, the supernatants were collected and filtered through 0.22 μm filters. Lentivirus medium was concentrated using Lenti-X Concentrator (Clontech, PT4421-2).

For lentivirus infection, cells or trachea explants were treated with medium containing 8 μg/mL of polybrene and 1 x 10^6 units of the viruses. After incubation for 48 hours, cells or explants were collected for protein extraction or immunofluorescence staining.

3.2.3 Mouse tracheal epithelial cell culture

The protocol for mouse tracheal epithelial cell (MTEC) culture was adapted from previously published methods (222; 223). Briefly, mouse tracheas were collected and placed in the dish of ice-cold Ham's F12 medium with penicillin/streptomycin and amphotericin B. After removing the attached tissues, tracheas were transferred into a 50 mL conical tube containing 0.15% pronase and digested overnight at 4°C. The next day, supernatant containing cells were collected and plated on Primaria plates to remove fibroblasts. The cell pellet was seeded at 7.5 x 10^4 – 1.0 x10^5 cells per well on the transwell plate, and cultured with MTEC proliferation media. After 10 days (or reaching confluency), cells were cultured at the air-liquid interface with MTEC differentiation media.

3.2.4 Immunofluorescence staining and imaging

Cells were fixed with 4% paraformaldehyde in PBS for 15 min at room temperature and washed with PBS three times. Tissue samples were fixed overnight at 4°C. Samples for cryosections were embedded in OCT compound medium, cut at 10 μm on a Leica cryostat, and mounted on Superfrost Plus microscope slides (Fisher Scientific, Cat: 22-37-246). Then samples were permeabilized and blocked with 3% bovine serum

albumin (BSA) in 0.1% Triton X-100 in PBS for 1 hour at room temperature. Then samples were incubated with primary antibody solution overnight at 4°C. The next day, cells were washed with PBS three times and incubated with secondary antibody solution for 1 hour at room temperature. After washing 3 times with PBS, samples were mounted with Invitrogen™ ProLong™ Gold Antifade Mountant (Invitrogen). The primary antibodies and final titrations used were goat anti-ACE2 (1:25; RD Systems AF933), rabbit anti-ACE2 (1:200; abcam ab15348), mouse anti-ACTUB (1:1500; Sigma-Aldrich T7451-25UL), mouse anti-TMPRSS2 (1:100, Sigma MABF2158), rabbit anti-Arl13b (1:500; Invitrogen PA5-32035), rat anti-HA (1:50; Roche 11867423001), and rabbit anti-V5(1:200; Genetex GTX117997). Secondary antibodies included rhodamine red™-X (RRX) AffiniPure Donkey anti-goat IgG (H+L) (1:200; Jackson ImmunoResearch 706295147), donkey anti-rat IgG Alexa Fluor™ 568 (1:200; Invitrogen A-11077), donkey anti-rabbit IgG (H+L) Alexa Fluor™ 568 (1:200; Invitrogen A10042), donkey anti-mouse 488(1:200, abcam ab96794), goat anti-mouse 555 (1:200; Invitrogen A-21424), donkey anti-rabbit 488 (1:200, abcam ab96919), phalloidin 488 (1:200; Invitrogen A12379), and DAPI (1:500; Sigma-Aldrich D9542). Images were captured using a Zeiss ELYRA S1 (SR-SIM) Super Resolution Microscope by Zen software. ImageJ/Fiji was used for image analysis.

3.2.5 Western blotting

Samples were lysed in RIPA buffer containing a protease inhibitor cocktail. Protein concentration was determined by BCA protein assay. Twenty μg/sample was loaded in Mini-PROTEAN TGX Precast Protein Gels (Bio-Rad). Gels were transblotted on PVDF membrane. Membranes were blocked in 3% BSA for 1 hour at room temperature and stained with primary antibody in 1% BSA in TBST overnight at 4°C. Secondary antibodies were diluted 1:2000 in 1% BSA in TBST and incubated at room temperature for 1 h with agitation. Immunoblots were developed with Clarity™ Western ECL Substrate (Bio-Rad, 1705061) and visualized on a ChemiDoc™ MP Imaging System with exposure times automatically selected to optimize band intensity relative to background.

3.2.6 Statistics

Statistical analyses were performed in Excel or with Python using Matplotlib and scipy. P values of less than 0.05 were considered as significant. Two-sided t-tests were used. The number of replicate images per independent experiment was ≥ 3.

3.3 Results

3.3.1 ACE2 is expressed in the airway cilia of ferret and mouse

To investigate the specific localization of ACE2 on cilia, we performed double immunofluorescence staining of ACE2 and a cilia marker acetylated α-tubulin (ACTUB) in ferret and mouse trachea. We used two commercially available antibodies (R&D AF933 and abcam ab15348) that have shown robust confirmation of ACE2 specificity (7; 221). AF933 antibody recognizes the immunogen from Gln18 to Ser740, which is part of the extracellular domain (Ecto). Ab15348 antibody recognizes a peptide consisting of aa 750 to the C-terminus, which is the cytoplasmic domain (Cyto). We found that staining using AF933 antibody exhibited the proximal localization of Ecto-ACE2 in ferret airway cilia. Using the same antibody, we found that Ecto-ACE2 also localized to the proximal compartment of mouse airway cilia (Figure 3.1A). In the ferret, staining with ab15348 antibody showed that Cyto-ACE2 is expressed in the whole cilia and enriched in the proximal region. We also stained mouse airway cilia for the Cyto-ACE2 and ACTUB by immunofluorescence. The staining shows Cyto-ACE2 localized to the whole cilia and was enriched in the proximal region (Figure 3.1B). We observed similar staining patterns in both ferret and mouse airway cilia using antibodies against Ecto-ACE2 and Cyto-ACE2. Our results showed that Ecto-ACE2 localizes to the proximal region of cilia, while Cyto-ACE2 localizes to the whole cilia (Figure 3.1C).

To validate the specificity of those two commercial ACE2 antibodies, we stained sections from the trachea of ACE2 KO mice and wild type (WT) mice for the Ecto-ACE2 and Cyto-ACE2 by immunofluorescence. The staining was done in combination with anti-ACTUB antibody to identify cilia. The

antibody against Ecto-ACE2 stained intensely at the proximal region of cilia in the trachea of WT mouse but showed no positive staining in the ACE2 KO mouse samples (Figure 3.2A). The antibody against Cyto-ACE2 stained throughout the cilia in the trachea of WT mouse also but showed no positive staining in ACE2 KO mouse samples (Figure 3.2B). We found a similar staining pattern as seen in the previous figure using Ecto-ACE2 and Cyto-ACE2 antibodies in trachea tissues from WT mice, while both antibodies stained negatively in trachea from ACE2 KO mice. This experiment supports the assertion that the two commercial antibodies are specific for ACE2 without off target labeling.

3.3.2 ACE2 is expressed in the cilia of mouse tracheal epithelial cells (MTECs) *in vitro*

We next chose to investigate whether the same staining pattern exists for *in vitro* cilia, so we cultured primary MTECs and differentiated them into ciliated cells in an air-liquid interface. We co-stained for ACTUB and phalloidin, which labels actin filaments, at different stages during the culture process (Figure 3.3A-B). To investigate the staining pattern of ACE2, we performed double immunofluorescence staining of ACE2 and ACTUB in MTECs, finding that Ecto-ACE2 localized to the proximal region of cilia, while Cyto-ACE2 was found in the whole cilia (Figure 3.3C-D). In summary, we found the staining pattern of Ecto-ACE2 and Cyto-ACE2 in cilia of MTECs *in vitro* to be consistent with that of mouse trachea samples.

3.3.3 Localization of epitope-tagged forms of ACE2 in airway cilia

The different staining pattern between the Ecto-ACE2 and Cyto-ACE2 antibodies could result from the Cyto-ACE2 only detecting the full-length ACE2 or ACE2 isoform 1, while Ecto-ACE2 detected both ACE2 isoforms 1 and 2. To answer the question, we examined whether epitope-tagged forms of ACE2 have similar staining pattern as commercial Ecto-ACE2 and Cyto-ACE2 antibodies. We packaged ACE2 isoforms 1 and 2 with an HA epitope tag at the N-terminus (downstream of the signal peptide) and a V5

tag at the C-terminus, respectively. The efficiency of the ACE2 lentivirus was confirmed in 293T cells through western blot analysis and immunofluorescence staining (Figure 3.4).

We next sought to examine the expression of epitope-tagged forms of ACE2 ex vivo, and transduced mouse trachea explants with the epitope-tagged ACE2 lentivirus or mNeon control lentivirus. The V5-tagged ACE2 isoform 1 localized to the distal compartment of cilia while V5-tagged ACE2 isoform 2 was expressed less intensively on cilia from mouse tracheal explants (Figure 3.5A). We also co-stained for the HA tag, which is inserted at the N-terminus downstream of the signal peptide. The expression of HA-tagged ACE2 isoform 1 was very sparse on cilia, and the majority of the labeling by HA-tagged ACE2 isoform 1 was at the apical side of the epithelial cells from mouse tracheal explants (Figure 3.6A).

To investigate the expression of epitope-tagged forms of ACE2 in cilia *in vitro*, we transduced the ciliated MTECs with ACE2 isoforms 1 and 2 or an mNeon control lentivirus respectively. Consistent with the staining pattern in cilia *ex vivo*, the C-terminal domain of ACE2 isoform 1 (V5-tagged) localized to the distal region of cilia, while the C-terminal domain of ACE2 isoform 2 was expressed less intensively on cilia compared to Cyto-ACE2 isofrom 1 on ciliar from *in vitro* MTECs (Figure 3.5B). We also quantified the V5 expression in cilia and found that the expression level of V5 was significantly higher in *ex vivo* cilia than in vitro cilia, and the intensity of Ctyo-ACE2 isoform 1 is stronger than Cyto-ACE2 isoform 2 especially in cilia from *in vitro* MTECs (Figure 3.5C). As before, we also co-stained for the HA-tag, the expression of HA-tagged ACE2 isoform 1 was very sparse on cilia from *in vitro* MTECs. HA-tagged ACE2 isoform 2 can be spotted on cilia from MTECs, but the majority of the labeling by HA-tagged ACE2 isoform 2 was at the apical side of the epithelial cells from MTECs *in vitro* (Figure 3.6B). The overall expression level of HA is relative low compared to V5 expression, but HA expression in *ex vivo* cilia is significantly higher than *in vitro* cilia for both ACE2 isoform 1 and isoform 2 (Figure 3.6C). On this basis, it is possible to assume that ACE2 shedding is more efficient in *in vitro* cilia compared with *ex vivo* cilia.

3.3.4 TMPRSS2 localizes to the distal region of cilia

The type II transmembrane serine protease (TMPRSS2) is an important host factor that contributes to SARS-CoV-2 infection via cleaving and activating the spike (S) protein for membrane fusion (3). In addition, TMPRSS2 can cleave ACE2 within amino acids 697 to 716, resulting in augmented SARS-S-driven entry (20). Since TMPRSS2 is also found to be localized to motile cilia in the airway (224; 225), we sought to identify the specific localization of TMPRSS2 within cilia. We co-stained for TMPRSS2 and Arl13b, a cilia marker, in cilia from samples *in vivo*, *ex vivo* and *in vitro*. We found that TMPRSS2 is enriched in the distal region of cilia (Figure 3.7).

Microvilli are short membrane protrusions from the surface of epithelial cells. Previously, Pinto *et al.* reported that both ACE2 and TMPRSS2 are localized to the microvilli but not cilia (53). To examine if ACE2 and TMPRSS2 localize in microvilli, we co-stained with ACE2 and phalloidin (a marker for microvilli). Figure 3.8 demonstrated that ACE2-positive staining extended throughout microvilli. TMPRSS2 did not localize to microvilli. Overall, our results affirm that ACE2 and TMPRSS2 are localized to cilia, and ACE2 extended through microvilli.

3.4 Discussion

We report here that ACE2 has a specific localization pattern within airway cilia, Ecto- ACE2 localizes to the proximal region of cilia, while Cyto ACE2 localizes to the whole cilia with proximal enrichment. We used two commercial antibodies: anti-Ecto ACE2 antibody (AF933) and anti-Cyto ACE2 antibody (ab15348). Studies have shown that ACE2 is expressed in various organs including lungs, brain, kidney, and intestinal tract using immunohistochemical analysis and single-cell RNA-seq (scRNA-seq) (47; 226; 227; 228). Lee and colleagues reported that ACE2 is expressed in the human respiratory cilia (7). Using anti-Ecto ACE2 antibody, we found that Ecto-ACE2 localizes to the proximal region of cilia. Using anti-Cyto ACE2 antibody, we found that Cyto ACE2 localizes to the whole cilia. Meanwhile, the anti-Ecto ACE2 antibody recognizes the extracellular domain of ACE2 isoform 1 (full-length) and isoform 2. The anti-Cyto ACE2

antibody recognizes the cytoplasmic domain of ACE2 isoform 1 and short ACE2. Due to the complexity and uncertain specificity of ACE2 commercial antibodies, we engineered epitope-tagged forms of ACE2 lentiviruses. We found that Cyto-ACE2 isoform 1 localizes to the distal compartment of cilia, while Cyto-ACE2 isoform 2 localizes to cilia and the apical surface of cells. The Ecto-ACE2 isoform 1 localizes to the proximal region of cilia while the Ecto-ACE2 isoform 2 localizes mainly to the apical surface of cells. We also found that TMPRSS2, sheddase of ACE2, localizes to the distal region of cilia (Figure 3.7). This may in part explain the distribution of Ecto-ACE2 on the proximal compartment of cilia and Cyto-ACE2 on the whole cilia. These results provide a mechanism that TMPRSS2, localized to the distal compartment of cilia, cleaves Ecto-ACE2, causing Ecto-ACE2 to olcalize to the proximal region of cilia. We also compared the fluorescence intensity of TMPRSS2, Ecto- and Cyto-ACE2 isoform 1 and 2 in samples *ex vivo* and *in vitro*. This process is more efficient *in vivo* than *in vitro*. These results support a model that Ecto-ACE2 localizes to the proximal region of airway cilia, while Cyto-ACE2 localizes to the whole cilia but is enriched in the proximal compartment of cilia. The distribution of Ecto-ACE2 in the proximal compartment could be due the shedding effect of TMPRSS2, which localizes to the distal region of cilia (Figure 3.9). ACE2 shedding seems more efficient *in vitro* than *in vivo*.

There have been conflicting results on the specific localization of ACE2 on cilia. Lee *et al.* tested 6 ACE2 commercial antibodies and demonstrated that ACE2 localizes to the respiratory cilia by using the Cyto ACE2 antibody (ab15348) (7). Ahn *et al.* reported that ACE2 and TMPRSS2 localize to the apical side of nasal ciliated epithelial cells by immunofluorescence staining and single-cell RNA sequencing (scRNA-Seq) (52). They found that both ACE2 and TMPRSS2 can be found on the apical side of ciliated cells by using the cyto ACE2 antibody and two anti-TMPRSS2 antibodies (abcam EPR3861 and Santa Cruz sc-515727). Manna and colleagues used antibodies against N-term ACE2 (ProSci 3227) and C-term ACE2 (Invitrogen MA5–32,307) and found that only ACE2 C-term antibody displayed plasma membrane signal on ciliated cells (43). More recently, Pinto *et al.* reported that both ACE2 and TMPRSS2 localized to the plasma membrane of microvilli but not cilia (53). In this study, they used antibodies detecting ACE2 intracellular domain (ab15348) and ACE2 extracellular domain (HPA000288). While the intracellular

ACE2 antibody stained intensely at the base of microvilli, the staining of extracellular ACE2 extended throughout the entire microvilli. Most of the studies on ACE2 localization use confocal or fluorescent microscope for imaging, which have limited resolution and magnification. Super resolution microscopy encompasses multiple fluorescence imaging techniques that offer a significant improvement in resolution and magnification. In this study, we acquired our images using Zeiss ELYRA S1 (SR-SIM) structured illumination super resolution microscope. We found that Ecto-ACE2 antibody stained intensely on the proximal region of cilia, while Cyto-ACE2 antibody stained the whole cilia.

To validate the specificity of the two commercial ACE2 antibodies in the current study, we performed immunofluorescence staining of tracheal samples for ACE2 in WT and ACE2 KO mouse. Our results exhibited positive ACE2 staining using the anti-Ecto ACE2 and anti-Cyto ACE2 antibodies in WT mouse but not ACE2 KO mouse. Previously, Sherman *et al.* tested 13 ACE2 commercial antibodies and found only 2 (AF933 and MAB9332 from RD) of them exhibited significant staining in an ACE2-overexpressing cell line by flow cytometry (221). However, they did not test the specificity of the Cyto-ACE2 antibody we used.

In addition, ACE2 has four protein isoforms translated by six ACE2 mRNA variants (6; 42). Ecto-ACE2 antibodies can detect most large ACE2 isoforms, whereas Cyto-ACE2 antibodies can detect full length ACE2 and short ACE2. Due to the complexity of ACE2 commercial antibodies and ACE2 isoforms, we engineered lentiviral tools expressing epitope-tagged forms of ACE2. By *in vitro* and *ex vivo* experiments, we show that the C-terminal domain of ACE2 isoform 1 localizes to the distal compartment of cilia, while the C-terminal domain of ACE2 isoform 2 localizes to the proximal region of cilia and the apical surface of ciliated epithelial cells.

TMPRSS2, the sheddase of ACE2, also localizes to motile cilia of the human respiratory tract (224; 225; 58). TMPRSS2 removes a short C-terminal fragment from ACE2, releasing the Ecto ACE2 (20). We found that TMPRSS2 localizes predominantly to the distal compartment of cilia, which can partly explain the distribution of Ecto-ACE2 on the proximal region of cilia. Future work will be focused on investigating the role of TMPRSS2 in regulating the localization of ACE2 in the compartments of cilia

and whether inhibiting TMPRSS2 can alter the distribution of ACE2 on cilia. Although Cyto-ACE2 localizes to whole cilia, it is also enriched in the proximal region of cilia. Future studies should investigate the mechanisms in which ACE2 is restricted to certain ciliary subcompartments and the trafficking of ACE2 within the cilia.

Table 3.1: Antibodies and fluorophores used in these studies

Antibodies	**Manufacturer**	**Catlog**	**Dilution**
Primary Antibodies			
Rabbit anti-ACE2	Abcam	ab15348	1:100
Goat anti-ACE2	R&D	AF933	1:25
Mouse anti-TMPRSS2	Sigma	MABF2158	1:100
Rat anti-HA	Roche	11867423001	1:50
Rabbit anti-V5	Genetex	GTX117997	1:200
Rabbit anti-Arl13b	Invitrogen	PA5-61840	1:500
Mouse anti-ACTUB	Sigma	T7451	1:1500
Secondary Antibodies			
Rhodamine Red™-X (RRX) Donkey Anti-Goat IgG (H+L)	Jackson ImmunoResearch	705-295-147	1:200
Alexa Fluor™ 568 Donkey anti-Rabbit IgG (H+L)	Invitrogen	A10042	1:200
DyLight® 488 Donkey Anti-Mouse IgG H&L	abcam	ab98794	1:200
Alexa Fluor™ 555 Goat anti-Mouse IgG (H+L)	Invitrogen	A-21424	1:200
Alexa Fluor™ 568 Donkey anti-Rat IgG (H+L)	Invitrogen	A78946	1:200
DyLight® 488 Donkey Anti-Rabbit IgG H&L	abcam	ab96919	1:200
Alexa Fluor™ 488 Phalloidin	Invitrogen	A12379	1:200
DAPI	Sigma-Aldrich	D9542	1:500

3.5 Supplementary Information

3.5.1 Antibodies and fluorophores used in these studies

(Table 3.1)

Table 3.2: Primers sequences for ACE2 lentivirus construction

Primer	Forward	Reverse
Guide gBlock	5'- CGT TGG CTA CCC GTG ATA TT -3'	5'- GCC CAG TCA TAG CCG AAT AG -3'

Table 3.3: Primer sequences for ACE2 knockout mouse genotyping

Primer	Forward	Reverse
26784_Neo3A	GCAGCGCATCGCCTTCTATC	
26784_3	GATGTCCAGCTCCTCCTGG	
26784_37		GCTCAATAACGACTTAGAACAT
1281_1	GTGGCACGGAACTTCTAGTC	
1281_2		CTTGTCAAGTAGCAGGAAGA

3.5.2 Primers sequences for ACE2 lentivirus construction

(Table 3.2)

3.5.3 Primer sequences for ACE2 knockout mouse genotyping

(Table 3.3)

3.5.4 Ace-2. N-terminal fragment

TGTCACGTTGGCTACCCGTGATATTGGCTAGCATCGATTGATCAACAAGTTTGTAC
AAAAAAGCAGGCTACAAAATGTCAAGCTCTTCCTGGCTCCTTCTCAGCCTTGTTGC
TGTAACTGCTGCTCAGTACCCGTATGATGTTCCGGATTACGCTGGCTACCCATACG
ACGTCCCCGACTACGCTGGCTACCCTTACGACGTCCCAGACTACGCTTCCACCAT
TGAGGAACAGGCCAAGACATTTTTGGACAAGTTTAACCACGAAGCCGAAGACCTGT
TCTATCAAAGTTCACTTGCTTCTTGGAATTATAACACCAATATTACTGAAGAGAAT
GTCCAAAACATGAATAATGCTGGGGACAAATGGTCTGCCTTTTTAAAGGAACAGTC
CACACTTGCCCAAATGTATCCACTACAAGAAATTCAGAATCTCACAGTCAAGCTTC

AGCTGCAGGCTCTTCAGCAAAATGGGTCTTCAGTGCTCTCAGAAGACAAGAGCAA
ACGGTTGAACACAATTCTAAATACAATGAGCACCATCTACAGTACTGGAAAAGTTT
GTAACCCAGATAATCCACAAGAATGCTTATTACTTGAACCAGGTTTGAATGAAATA
ATGGCAAACAGTTTAGACTACAATGAGAGGCTCTGGGCTTGGGAAAGCTGGAGAT
CTGAGGTCGGCAAGCAGCTGAGGCCATTATATGAAGAGTATGTGGTCTTGAAAAAT
GAGATGGCAAGAGCAAATCATTATGAGGACTATGGGGATTATTGGAGAGGAGACT
ATGAAGTAAATGGGGTAGATGGCTATGACTACAGCCGCGGCCAGTTGATTGAAGA
TGTGGAACATACCTTTGAAGAGATTAAACCATTATATGAACATCTTCATGCCTATG
TGAGGGCAAAGTTGATGAATGCCTATCCTTCCTATATCAGTCCAATTGGATGCCTC
CCTGCTCATTTGCTTGGTGATATGTGGGGTAGATTTTGGACAAATCTGTACTCTTT
GACAGTTCCCTTTGGACAGAAACCAAACATAGATGTTACTGATGCAATGGTGGACC
AGGCCTGGGATGCACAGAGAATATTCAAGGAGGCCGAGAAGTTCTTTGTATCTGTT
GGTCTTCCTAATATGACTCAAGGATTCTGGGAAAATTCCATGCTAACGGACCCAGG
AAATGTTCAGAAAGCAGTCTGCCATCCCACAGCTTGGGACCTGGGGAAGGGCGAC
TTCAGGATCCTCTATTCGGCTATGACTGGGCGG

3.5.5 Ace2. C-terminal fragment for isoform 1

CACGTTGGCTACCCGTGATATTGGATCCTTATGTGCACAAAGGTGACAATGGACGA
CTTCCTGACAGCTCATCATGAGATGGGGCATATCCAGTATGATATGGCATATGCTG
CACAACCTTTTCTGCTAAGAAATGGAGCTAATGAAGGATTCCATGAAGCTGTTGGG
GAAATCATGTCACTTTCTGCAGCCACACCTAAGCATTTAAAATCCATTGGTCTTCT
GTCACCCGATTTTCAAGAAGACAATGAAACAGAAATAAACTTCCTGCTCAAACAAG
CACTCACGATTGTTGGGACTCTGCCATTTACTTACATGTTAGAGAAGTGGAGGTGG
ATGGTCTTTAAAGGGGAAATTCCCAAAGACCAGTGGATGAAAAAGTGGTGGGAGA
TGAAGCGAGAGATAGTTGGGGTGGTGGAACCTGTGCCCCATGATGAAACATACTG
TGACCCCGCATCTCTGTTCCATGTTTCTAATGATTACTCATTCATTCGATATTACA

CAAGGACCCTTTACCAATTCCAGTTTCAAGAAGCACTTTGTCAAGCAGCTAAACAT
GAAGGCCCTCTGCACAAATGTGACATCTCAAACTCTACAGAAGCTGGACAGAAACT
GTTCAATATGCTGAGGCTTGGAAAATCAGAACCCTGGACCCTAGCATTGGAAAATG
TTGTAGGAGCAAAGAACATGAATGTAAGGCCACTGCTCAACTACTTTGAGCCCTTA
TTTACCTGGCTGAAAGACCAGAACAAGAATTCTTTTGTGGGATGGAGTACCGACTG
GAGTCCATATGCAGACCAAAGCATCAAAGTGAGGATAAGCCTAAAATCAGCTCTTG
GAGATAAAGCATATGAATGGAACGACAATGAAATGTACCTGTTCCGATCATCTGTT
GCATATGCTATGAGGCAGTACTTTTTAAAAGTAAAAAATCAGATGATTCTTTTTGG
GGAGGAGGATGTGCGAGTGGCTAATTTGAAACCAAGAATCTCCTTTAATTTCTTTG
TCACTGCACCTAAAAATGTGTCTGATATCATTCCTAGAACTGAAGTTGAAAAGGCC
ATCAGGATGTCCCGGAGCCGTATCAATGATGCTTTCCGTCTGAATGACAACAGCCT
AGAGTTTCTGGGGATACAGCCAACACTTGGACCTCCTAACCAGCCCCCTGTTTCCA
TATGGCTGATTGTTTTTGGAGTTGTGATGGGAGTGATAGTGGTTGGCATTGTCATC
CTGATCTTCACTGGGATCAGAGATCGGAAGAAGAAAAATAAAGCAAGAAGTGGAG
AAAATCCTTATGCCTCCATCGATATTAGCAAAGGAGAAAATAATCCAGGATTCCAA
AACACTGATGATGTTCAGACCTCCTTTGGTAAGCCTATCCCTAACCCTCTCCTCGG
TCTCGATTCTACGTAGCAATCAACGCGTTCTATTCGGCTATGACTGGGCGG

3.5.6 Ace2. C-terminal fragment for isoform 2

CACGTTGGCTACCCGTGATATTAGGATCCTTATGTGCACAAAGGTGACAATGGAC
GACTTCCTGACAGCTCATCATGAGATGGGGCATATCCAGTATGATATGGCATATGC
TGCACAACCTTTTCTGCTAAGAAATGGAGCTAATGAAGGATTCCATGAAGCTGTTG
GGGAAATCATGTCACTTTCTGCAGCCACACCTAAGCATTTAAAATCCATTGGTCTT
CTGTCACCCGATTTTCAAGAAGACAATGAAACAGAAATAAACTTCCTGCTCAAACA
AGCACTCACGATTGTTGGGACTCTGCCATTTACTTACATGTTAGAGAAGTGGAGGT
GGATGGTCTTTAAAGGGGAAATTCCCAAAGACCAGTGGATGAAAAAGTGGTGGGA

GATGAAGCGAGAGATAGTTGGGGTGGTGGAACCTGTGCCCCATGATGAAACATAC
TGTGACCCCGCATCTCTGTTCCATGTTTCTAATGATTACTCATTCATTCGATATTA
CACAAGGACCCTTTACCAATTCCAGTTTCAAGAAGCACTTTGTCAAGCAGCTAAAC
ATGAAGGCCCTCTGCACAAATGTGACATCTCAAACTCTACAGAAGCTGGACAGAAA
CTGTTCAATATGCTGAGGCTTGGAAAATCAGAACCCTGGACCCTAGCATTGGAAAA
TGTTGTAGGAGCAAAGAACATGAATGTAAGGCCACTGCTCAACTACTTTGAGCCCT
TATTTACCTGGCTGAAAGACCAGAACAAGAATTCTTTTGTGGGATGGAGTACCGAC
TGGAGTCCATATGCAGACCAAAGCATCAAAGTGAGGATAAGCCTAAAATCAGCTCT
TGGAGATAAAGCATATGAATGGAACGACAATGAAATGTACCTGTTCCGATCATCTG
TTGCATATGCTATGAGGCAGTACTTTTTAAAAGTAAAAAATCAGATGATTCTTTTT
GGGGAGGAGGATGTGCGAGTGGCTAATTTGAAACCAAGAATCTCCTTTAATTTCTT
TGTCACTGCACCTAAAAATGTGTCTGATATCATTCCTAGAACTGAAGTTGAAAAGG
CCATCAGGATGTCCCGGAGCCGTATCAATGATGCTTTCCGTCTGAATGACAACAG
CCTAGAGTTTCTGGGGATACAGCCAACACTTGGACCTCCTAACCAGCCCCCTGTTT
CCATATGGCTGATTGTTTTTGGAGTTGTGATGGGAGTGATAGTGGTTGGCATTGTC
ATCCTGATCTTCACTGGGATCAGAGATCGGAAGAAGCCAACTCCACTCTTGGGAAA
AAGTTGGCTGACAGCCATCTTGAAAGATGGTAAGCCTATCCCTAACCCTCTCCTCG
GTCTCGATTCTACGTGAATCAACGCGTTAACTATTCGGCTATGACTGGGCGG

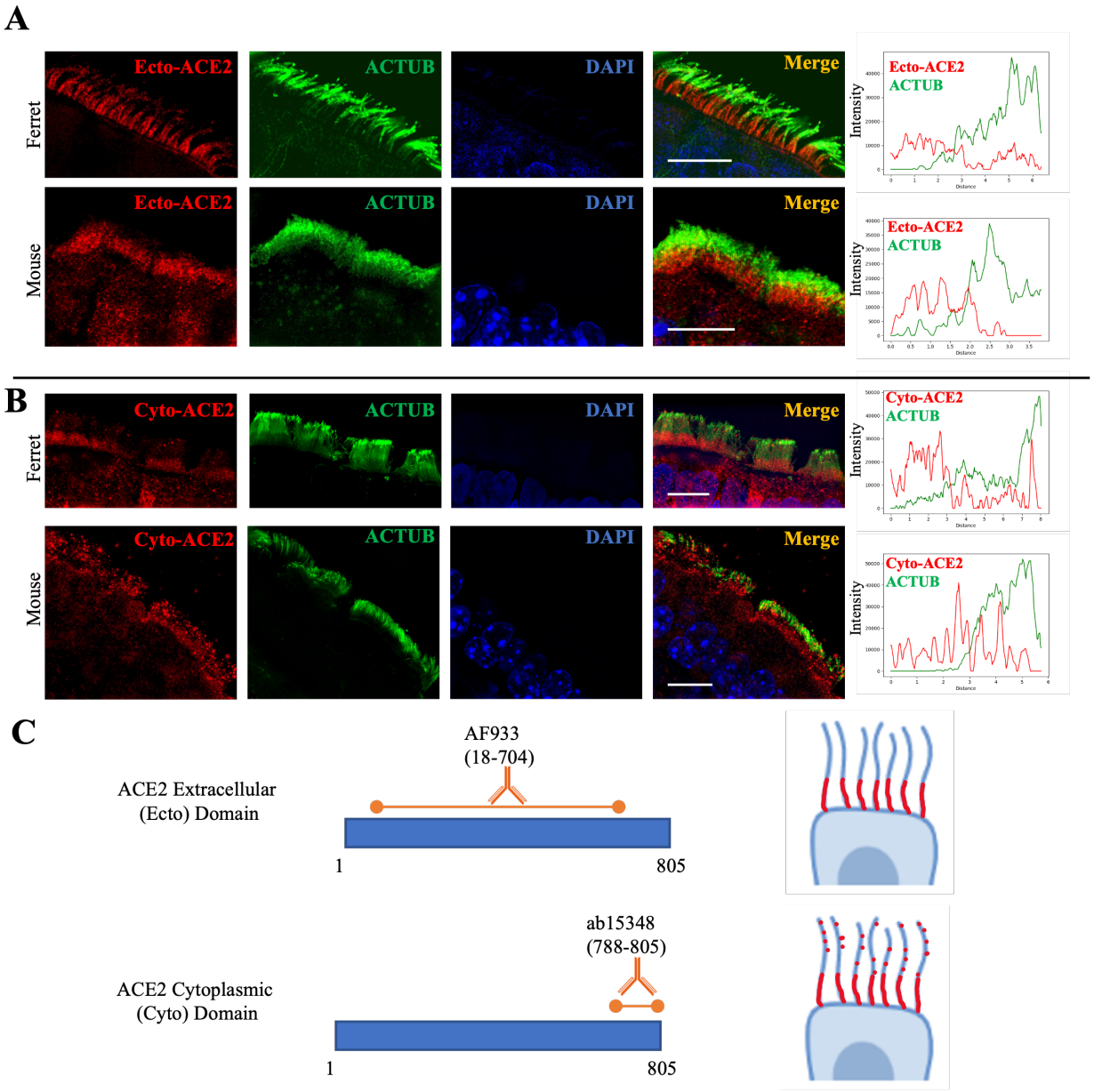

Figure 3.1: Representative immunofluorescence staining of ACE2 and cilia marker acetylated α-tubulin (ACTUB) in ferret and mouse trachea. Panel (**A**) shows the location of extracellular domain (Ecto) of ACE2 recognized by goat anti-ACE2 (RD, AF933) on ferret and mouse trachea. Panel (**B**) shows the fluorescent staining of cytoplasmic domain (Cyto) of ACE2 recognized by rabbit anti-ACE2 antibody (abcam, ab15348) on ferret and mouse trachea. Scale bars: 10 μm. (**C**) Schematic representation of anti-ACE2 antibodies and their staining patterns.

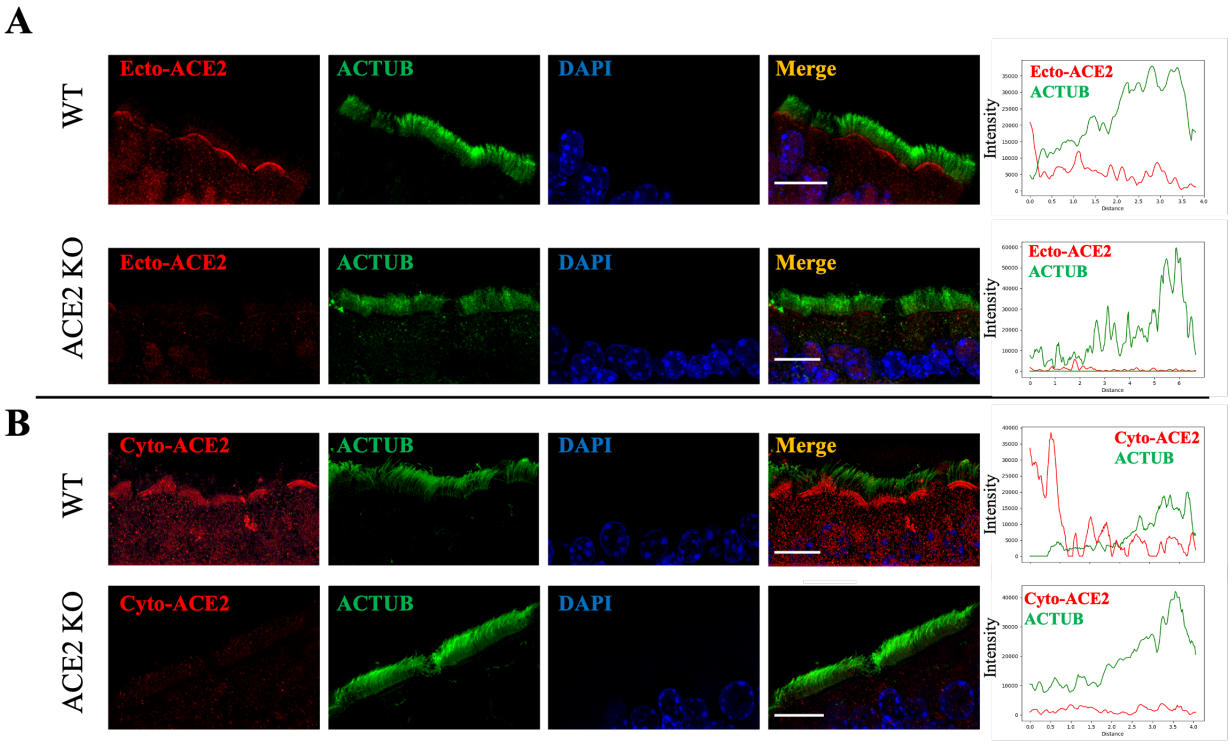

Figure 3.2: Immunofluorescence analysis of ACE2 in the trachea from WT and ACE2 KO mice. Panel **A** shows the localization of ACE2 recognized by the Ecto-ACE2 antibody (AF933) in respiratory cilia from WT and ACE2 KO mice. Staining for Ecto-ACE2 antibody is negative in ACE2 KO mouse. Panel **B** shows the location of ACE2 recognized by the Cyto-ACE2 antibody (ab15348) in respiratory cilia from WT and ACE2 KO mice. The IF staining for Cyto-ACE2 is negative in ACE2 KO mouse. Scale bars, 10 μm.

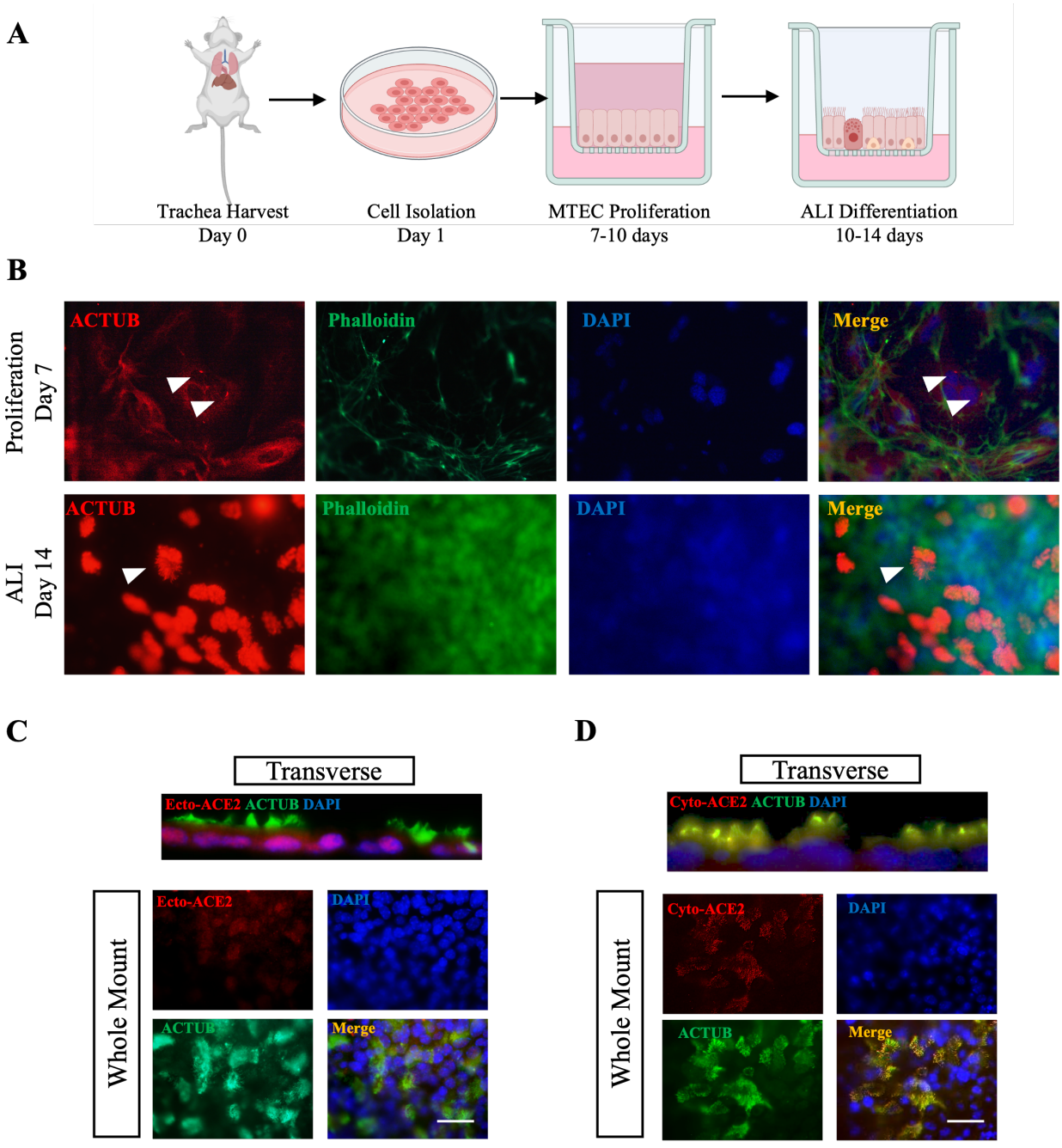

Figure 3.3: ACE2 localizes to cilia in mouse tracheal epithelial cells (MTECs) at an air-liquid interface (ALI). **A** Schematic diagram showing the differentiation of MTECs cultured at the ALI. **B** Double immunofluorescence staining using ACTUB as a cilia marker and phalloidin as an actin marker in MTECs during the differentiation process. Arrows indicate cilia. **C** Immunofluorescence staining for Ecto-ACE2 (AF933) and ACTUB in differentiated MTECs. Ecto-ACE2 was found to be localized to the proximal region of cilia and the cell surface of MTECs. **D** Immunofluorescence antibody labeling against Cyto-ACE2 (ab15348) and ACTUB. Cyto-ACE2 was found to be localized to the whole cilia from MTECs. Scale bars, 50 μm.

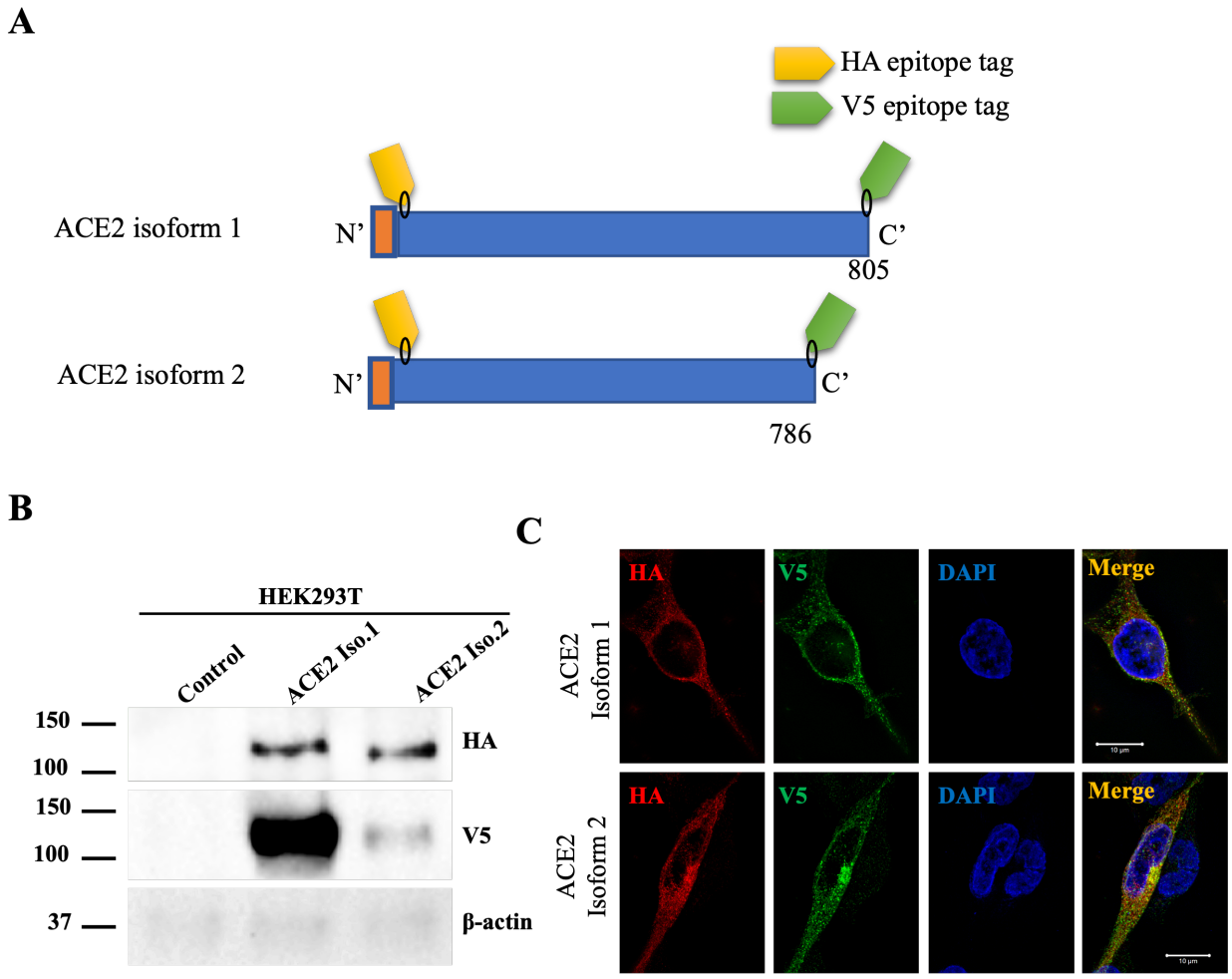

Figure 3.4: Epitope-tagged forms of ACE2 lentivirus packing. **A** diagram of ACE2 isoform 1 with HA at the N-terminus and V5 at the N-terminus. ACE2 isoform 2 with an HA tag at the N-terminus and V5 tag at aa 786. **B** illustrates western blot analysis of epitope-tagged ACE2 in HEK 293T cells. C Immunofluorescence staining of epitope-tagged forms of ACE2 on HEK293T cells. Scale bars, 10 μm.

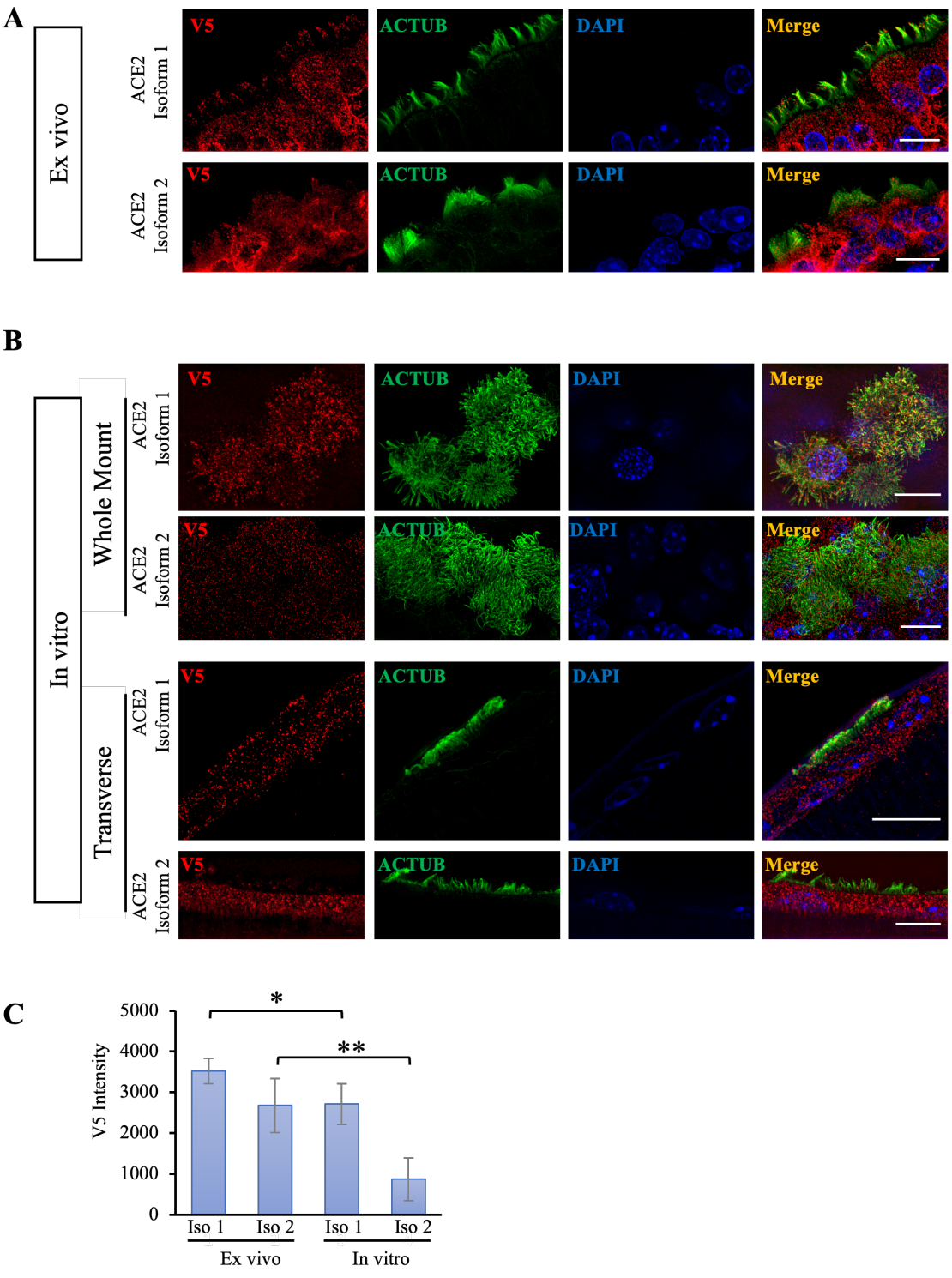

Figure 3.5: Immunofluorescence analysis of V5-tagged (C-terminus) forms of ACE2 on cilia. Panel **A** shows the localization of V5-tagged ACE2 on cilia from mouse tracheal explants. Panel **B** shows the representative IF images of V5 and ACTUB expression in cilia from MTECs. Scale bars, 10 μm. **C**, quantification of V5 expression on cilia. Error bars represent mean ± SD. Student's T-Test was used to assess statistical significance. * $P < 0.05$, ** $P < 0.01$.

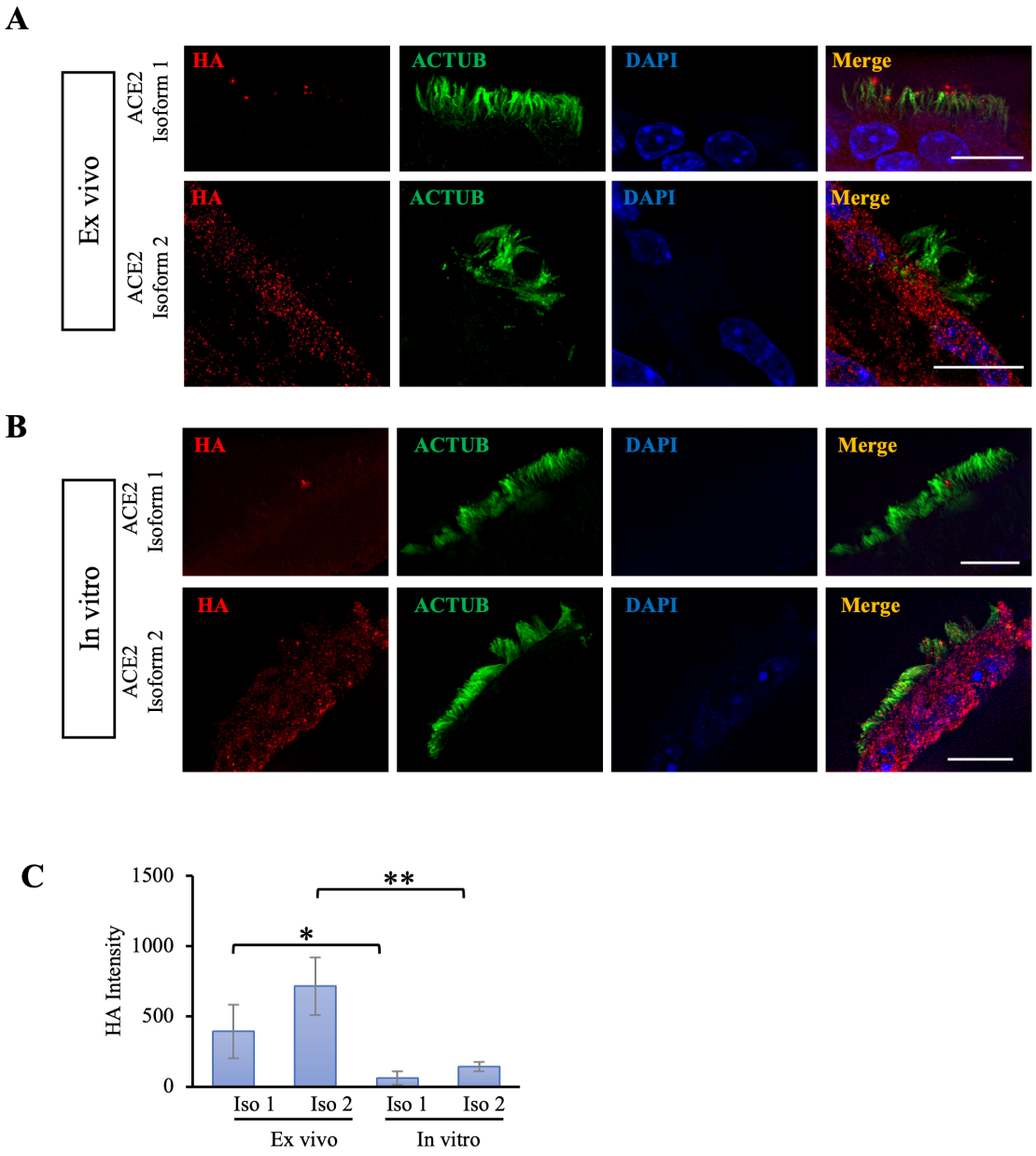

Figure 3.6: Immunofluorescence analysis of HA-tagged forms of ACE2 on cilia from mouse epithelial cells *ex vivo* and *in vitro*. **A**, representative double IF staining of HA (N-terminus tag) and ACTUB in mouse tracheal explants *ex vivo*. **B**, representative double IF staining of HA (N-terminus tag) and ACTUB in ALI-cultured MTECs. Scale bars, 10 μm. **C**, quantification of the expression of HA in cilia from *ex vivo* and *in vitro* samples. Error bars represent mean ± SD. Student's T-Test was used to assess statistical significance. * $P < 0.05$, ** $P < 0.01$.

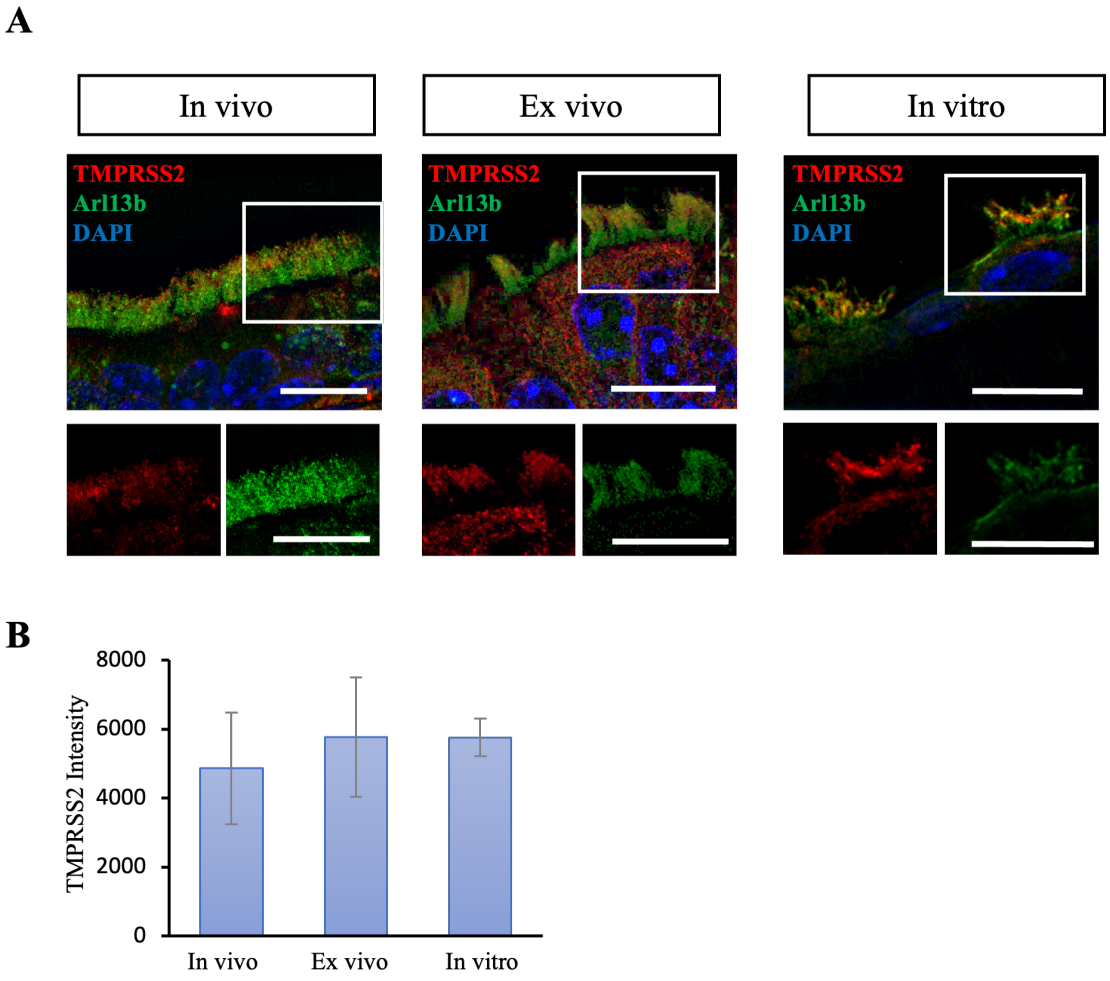

Figure 3.7: TMPRSS2 localizes to the distal region of cilia. **A** Representative immunofluorescence staining of TMPRSS2 and Arl13b in cilia from *in vivo*, *ex vivo*, and *in vitro* samples. Scale bars, 10 μm. **B** Quantification of the expression of TMPRSS2 in cilia. Error bars represent mean ± SD. Student's T-Test was used to assess statistical significance.

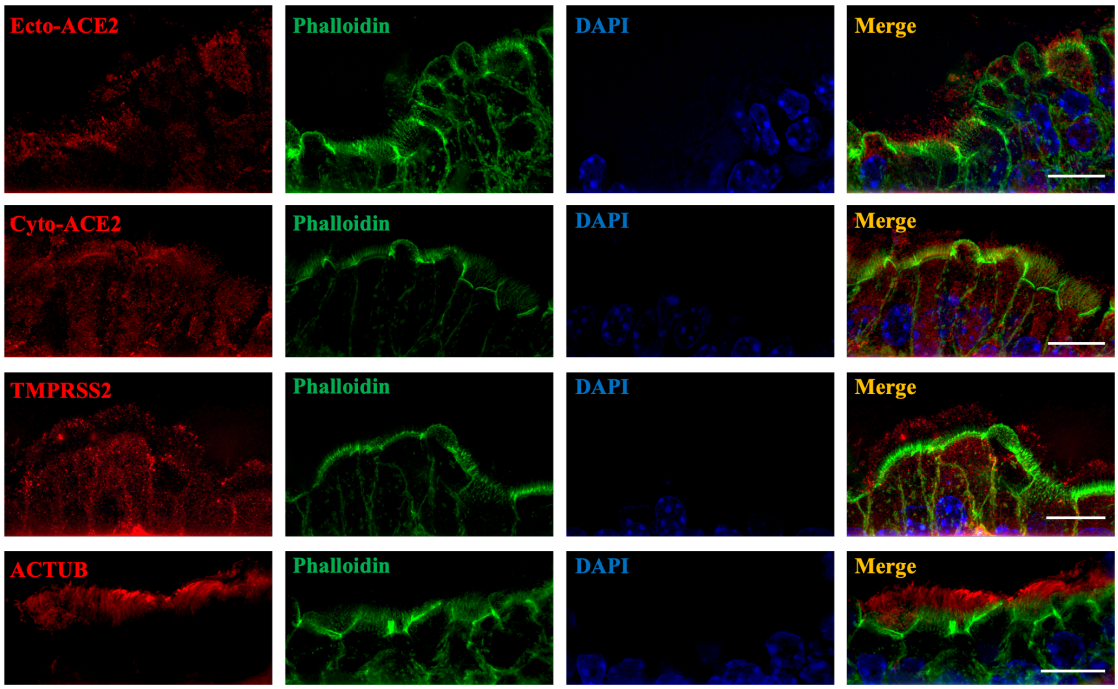

Figure 3.8: ACE2 and TMPRSS2 localizes to cilia and extends through microvilli. Representative images of Ecto-ACE2, Cyto-ACE2, TMPRSS2, ACTUB and phalloidin in mouse trachea. Scale bars, 10 μm.

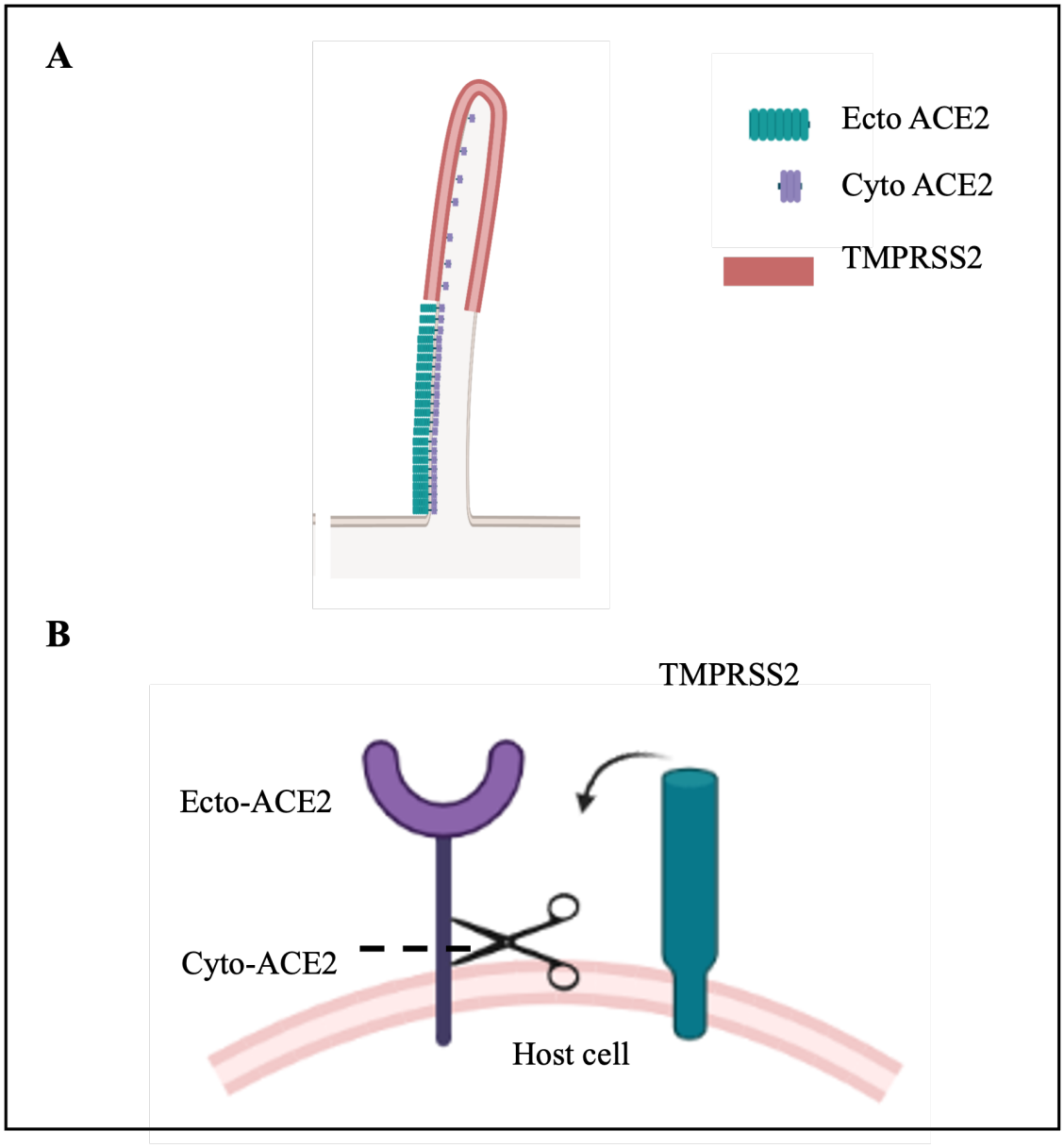

Figure 3.9: Model for ACE2 localization in cilia. **A** Model illustrates that Cyto-ACE2 localizes to distal cilia, Ecto-ACE2 localizes to proximal cilia, while TMPRSS2 localizes to distal cilia. **B** illustrates Ecto-ACE2 is cleaved off by TMPRSS2.

Chapter 4

Constructing a Validation Dataset of Ciliary Motion Phenotypes

4.1 Introduction

Cilia are hair-like structure found on the surface of almost all mammalian cell types. Cilia beat in a coordinated and synchronized manner to propel foreign objects out of the way. The motile cilia on the surface of respiratory epithelia are one of the major components of mucociliary clearance (MCC), which is the primary defense mechanism of the lung (12). The malfunction of cilia can cause diseases known as ciliopathies, a group of genetic disorders associated with cilia (76; 229). Primary ciliary dyskinesia (PCD) is an autosomal recessive genetic ciliopathy, characterized by impaired MCC and chronic respiratory infections (230; 231). Currently, the diagnosis of PCD relies on a combination of tests including ciliary ultrastructural analysis and genetic testing. However, 30% of PCD patients have normal or near-normal ciliary ultrastructure but abnormal ciliary function (232; 233). For example, PCD patients with DNAH11 mutations showed reduced waveform amplitude in cilia and a hyperkinetic beating pattern (234; 235).

Therefore, robust ciliary motion phenotype analysis is of great importance in diagnosing PCD. Currently, there is no standard way to quantify cilia motion phenotypes; researchers have to analyze the ciliary motion pattern manually by playing the video in slow motion back and forth, which is time-consuming and labor intensive. The analysis of cilia motion waveforms is still heavily subjective (107). Precise quantification of cilia motion waveform is a challenging task. Current computer vision algorithms for recognizing ciliary area and analyzing ciliary motion are still under development and rely on a large-scale validation dataset for model evaluation. Therefore, we propose to build this validation dataset of ciliary motion phenotypes to address this.

The beating of respiratory cilia consists of a forward power stroke and a backward recovery stroke in the same plane (107). The airway ciliary beat frequency (CBF) is estimated to vary from 3 to 16 Hz (14; 150). CBF can be modulated by various stimuli such as temperature and drugs (236; 237; 164). To analyze cilia motion, images are recorded at over 200 frames per second with a high-speed video microscope. Many clinicians and researchers still analyze cilia motion by manual counting and visualization (238; 239). However, this is labor-intensive and time-consuming. In recent years, efforts have been invested toward developing computational tools utilizing conventional or deep learning-based methods to help analyse cilia motion in a semi- or fully automated way (211; 17; 111; 207; 16; 209). Quinn *et al.* built a computational pipeline using computer vision and machine learning algorithms to classify cilia motion into normal and abnormal with over 90% accuracy (17). This method was trained on an in-house dataset consisting of 325 videos and relied on expert's evaluation as ground truth regarding whether the sample is normal or abnormal. In a follow-up study, Lu *et al*. generated manual masks and combined DenseNet for segmentation and convolutional LSTM for cilia motion classification (112). This framework achieved an accuracy of 86.2% in segmentation and over 90% accuracy in classification. For the segmentation task, Zain *et al.* proposed deep learning pipelines utilizing Fully Convolutional DenseNet (FC-DenseNet), U-Net with low-level feature extraction to analyze the same ciliary dataset (18; 113). The composite model achieved an accuracy of 77% and an Interaction of Union (IoU) score of 44%. However, the segmentation results are still not satisfactory. There's an urgent need for a large-scale validation dataset of ciliary motion.

To access the ciliary beat pattern, the first step is to segment cilia, which is to detect and separate ciliary areas from images. Cilia segmentation depends on a large-scale video dataset for evaluating the deep learning pipeline. Currently, there is no shared video dataset of cilia motion. Therefore, we propose to address this need by building a dataset of cilia motion phenotypes under several categories including temperature, drug and genetic manipulations. In addition, we will provide the mean CBF as a baseline metric. By building this dataset, we hope to provide the clinicians and researchers a validation dataset of various cilia motion phenotypes. Also, we aim to provide the computer science community with a video dataset to help with model development and evaluation.

Ciliary activity is dependent on temperature. There is a linear correlation between CBF and temperature (240; 241; 237; 242). Clary-Meinesz *et al.* studied CBF of human nasal and tracheal epithelial cells at different temperatures from 5°C to 50°C and found that CBF increased with temperature from 9°C to 20°C but levelled between 20°C to 45°C (237). Nikolaizik and colleagues compared CBF of nasal brushings from young adults at 25°C 32°C and 37°C. They found that CBF was significantly increased when measured at a higher temperature (242).

Cilia motion is affected by many pharmacologic substances (164; 243; 244). In the current study, we investigated cilia motion phenotypes affected by seven drugs: Adenosine 5-triphosphate (ATP), Amphotericin B, azelastine, calcium inonphore A23187, N-acetylcysteine amide (NAC), terbutaline, and trifluoperazine. ATP can increase CBF via inducing intracellular Ca^{2+} (245). Amphotericin B is an antifungal medicine used for treating life-threatening fungal infections and leishmaniasis. Hofer *et al.* reported that amphotericin B diluted in distilled water reduced CBF by 50%. However, amphotericin B diluted in saline had no effect on CBF (246). Azelastine is a commonly used anti-allergy intranasal formulation, which is introduced for topical intranasal therapy of perennial or seasonal allergic rhinitis (247). In an early study, researchers found the azelastine had no effect on CBF neither *in vitro* or *in vivo* (248). However, Alberty and colleagues reported that azelastine slightly reduced CBF (249). Calcium ionophore can stimulate CBF in human respiratory epithelia *in vitro* through mediating a calmodulin-sensitive system (250). In an early study, however, Satir observed ciliary arrest of freshwater mussel gills by perfusion with 10^{-5}M calcium

ionophore (251). The pharmacological effects of NAC on cilia is conflicting. Early studies reported that NAC reduced CBF of human nasal samples in a dose- and time-dependent manner (252; 253). Gancer and colleagues found that NAC stimulated ciliary function at 10 mg/ml concentration, and NAC can cause a total cessation of cilia movement at 200 mg/ml (254). Terbutaline is a β2-adrenergic agonist that can increase CBF and decrease the volume of ciliated cells. The cell shrinkeage induced by terbutaline stimulated CBF by increasing cAMP (255). Trifluoperazine is an inhibitor of calcium-dependent protein kinases that can decrease CBF (250). Previous studies on the effect of drugs on ciliary function were mostly focused on CBF, while few studies reported the effects on ciliary waveform. Conflicting results are seen in studies involving the same pharmacological drugs presumably due to different models, concentrations, and lab environments. Therefore, we propose to investigate the effects of the above mentioned seven drugs on ciliary motion and calculate the CBF as a baseline metric.

For genetic manipulation, we investigate the role of angiotensin-converting enzyme-2 (ACE2) on cilia motility. ACE2 is the SARS-CoV-2 receptor localized on respiratory cilia (7). Motile cilia play an important role in the replication of SARS-CoV-2 (8). Studies have reported that ACE2 KO mice exhibited worsened respiratory function after infection (68; 256), however, whether ACE2 plays a role in regulating cilia motility remains unknown. In the current study, we use several strategies, including ACE2 inhibitor (MLN-4760) and shRNA, to manipulate ACE2.

Cilia motion is usually captured *in vitro* with a high-speed video microscope. Previously, cilia motion was qualitatively measured as normal, abnormal, or stiff (257; 176). Chilvers *et al.* developed a ciliary dyskinesia scoring system (0 to 3) based on symptoms, cellular changes, and ciliary beat pattern (258). For quantitative measurement, Papon *et al.* described 12 quantitative parameters to characterize ciliary beat pattern (178). Those parameters include the cilia length, angle of beating, global frequency and so on. To estimate MCC, fluorescent microbeads are added to the media. MCC can be calculated by tracking the movement of the beads. In this study, we provide the methodology to analyze cilia parameters including CBF, ciliary beat amplitude, angle, and arclength.

Table 4.1: Drug list

Name	Catlog	Manufacturer
Adenosine 5'-triphosphate (ATP)	A26209-1G	Sigma-Aldrich
Amphotericin B	A2942	Sigma-Aldrich
Azelastine	A7611-10MG	Sigma-Aldrich
Calcium inonphore A23187	C7522-1MG	Simga-Aldrich
MLN-4760	5306160001	Simga-Aldrich
N-acetylcysteine amide	A0737-5MG	Simga-Aldrich
Terbutaline	PHR3246-250MG	Sigma-Aldrich
Trifluoperazine	T8516-5G	Sigma-Aldrich

We present a large-scale video validation dataset of ciliary motion phenotypes. Our validation dataset consists of 872 videos and their corresponding ground truth masks. This is the first open-source cilia video set to enable cilia video analysis and characterization of ciliary function under different stimuli.

4.2 Methods

4.2.1 Solutions and Chemicals

Leibovitz's L-15 medium (L-15) was purchased from Gibco (Cat: 11415064). L-15 was supplemented with 10% FBS and Penicillin-Streptomycin for trachea collection and imaging. ATP, Amphotericin B, azelastine, calcium ionophore A23187, N-acetylcysteine, terbutaline, trifluoperazine were obtained from Sigma-Aldrich (St Louis, MO). Dimethyl Sulfoxide (DMSO) was purchased from EMD Millipore Corp (Cat: 317275-500ML). Calcium ionophore, azelastine, terbutaline, trifluoperazine were dissolved in DMSO and diluted in L15 to the final working concentrations. A detailed table of drug information is listed below (Table 4.1).

4.2.2 Sample Preparation

Mouse tracheal pieces were prepared according to the protocol described previously (187). Briefly, BALB/C mice (6-10 week old) were euthanized with CO_2, as approved by the Institutional Animal Care and Use Committee (IACUC) of the University of Georgia. After euthanasia, mouse tracheas were collected. Tracheal samples were cut into 3-4 ring segments and maintained in L-15 supplemented with antibiotics at 4 °C. All the experiments were performed within 2 days of collection.

The samples were imaged at room temperature (22°C) except for when under temperature treatment. For temperature treatment, mouse tracheal samples were incubated at 18°C, 22°C, 24°C, 26°C and 29°C. In order to measure the CBF at different temperatures, we set the microscope room temperature control system to the target temperature overnight prior to imaging.

4.2.3 Drug Application

Mouse tracheal samples were mounted on a coverslip. Then we drew a circle surrounding the sample using Vaseline. A second coverslip was placed over the tissue to form the chamber. Drugs were added manually to the chamber by micropipette. All samples were maintained at the room temperature (22°C) during the evaluation. Medium solutions supplemented with drugs contained a final concentration of no more than 1 % of DMSO, a concentration known not to affect CBF (259).

After baseline videos, samples were perfused with L-15 medium containing drugs at different concentrations. Cilia videos were imaged after being incubated with the perfusion. After drug perfusion, the perfusate was replaced with L-15 medium and cilia were imaged to determine whether the effects of drugs are reversible. Table 4.2 summarizes the working concentrations and incubation time of each drug.

4.2.4 ACE2 Manipulation

Mouse ACE2 shRNA variants were purchased from VectorBuilder (Catalog #: VB010000-0001mty, VB900138- 0657mqd, VB900138-0321tyd, VB900138-0320wfm). ACE2 shRNA or scramble lentiviruses

Table 4.2: Working concentration and incubation time for drugs

Drug name	Stock Concentration	Working Concentration	Incubation Time
ATP	500 mM	1μM, 10μM, 100μM, 1mM	10 min
Amphotericin B	250 μg/mL	0.25 μg/mL, 2.5 μg/mL, 25ug/mL	20 min
Azelastine	10 mM	1μM, 10μM, 100μM	5 min
Calcium inonphore A23187	10 mg/mL	0.1 μM, 1μM, 10μM, 100μM	10 min
N-acetylcysteine amide	20 mg/mL	0.5 mg/mL, 1mg/mL	5 min
Terbutaline	100mM	0.5 μM, 10μM	3 min
Trifluoperazine	100mM	5μM, 10μM, 100μM	30 min

were produced by transfection of HEK293T cells with target vectors, and packaging vectors psPAX2 (addgene, #12260) and pMD2.G (addgene, #12259) using Lipofectamine™3000 Transfection Reagent (Cat: L3000015, ThermoFisher, USA). Lentivirus media were concentrated using Lenti-X Concentrator (Clontech, PT4421-2). For lentivirus infection, ciliated mouse tracheal epithelial cells or tracheal explants were treated with medium containing 8 μg/mL of polybrene and 1x10^6 units of the viruses. We also treated mouse tracheal explants with MLN-4760 (1 μM final), an ACE2 inhibitor, for 24 hours.

4.2.5 Imaging with High-Speed Video Microscopy

Tracheal samples were imaged with a TI2- U inverted microscope (Nikon) equipped with a 40x and an additional 2.5x DIC objectives. Images (800 x 800 pixels) of ciliary motion were recorded at 250 frames per second (fps) for 6 seconds using the Mikrotron high-speed camera and Core2 image acquisition software. Each pixel is 0.07987 μm. For each sample, we recorded at least 3 videos of independent ciliated edges from side view.

4.2.6 Ciliary Beating Analysis

Cilia beat frequency (CBF). CBF was estimated using Fast Fourier Transform (FFT) by calculating the variation of the mean gray level of the pixel. The cilia videos were analyzed for CBF using an in-house computational pipeline written in Python (17).

To characterize cilia beat pattern (CBP), a single cilium is manually tracked during a full beating cycle using napari, which is a multi-Dimensional Image Viewer written in Python (260). The contour of the positions before the active and the recovery strokes can be used to determine a series of ciliary characteristics such as cilium length, distance traveled by the tip, and curvature (178). Figure 4.1 shows an example of a manually labeled full cycle. P_0 indicates the base of the cilium. P_1 and P_2 label the coordinates of the tip of the cilium during the beginning and the end of the power stroke.

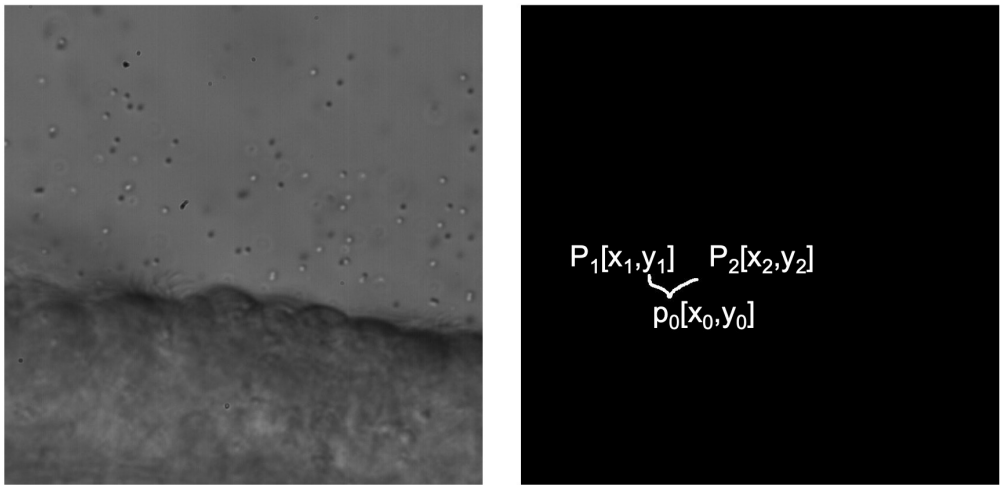

Figure 4.1: Example of tracking a full cycle of a cilium. **Left** shows a sample frame image of a cilia video. **Right** shows manual tracking of the beginning and end of a power stroke from a cilium. P_0 labels the base of the cilium. P_1 and P_2 label the coordinates of the tip of the cilium during the beginning and the end of the power stroke.

Several parameters can be determined using the acquired positions. The cilium **length** is estimated as the maximum value among the forward stroke line and the recovery stroke line. The angle of beating (θ) is calculated as following:

$$\theta = arccos(\frac{\overrightarrow{P_0P_1} \cdot \overrightarrow{P_0P_2}}{|P_0P_1| \cdot |P_0P_2|})$$

In addition, the **ciliary beating amplitude** is determined by $\overline{P_1P_2}$. **Cilia density** is estimated by comparing the pixel intensity of the cilia area with the mean pixel intensity of the background (163). A region of background and region of cilia are labeled using napari (Figure 4.2). We consider a homogeneous

distribution of cilia and, therefore, cilia density (ρ) can be calculated as follows in a ciliated region:

$$\rho = \frac{Number of Pixels \leq Mean Background}{Number of Pixels}$$

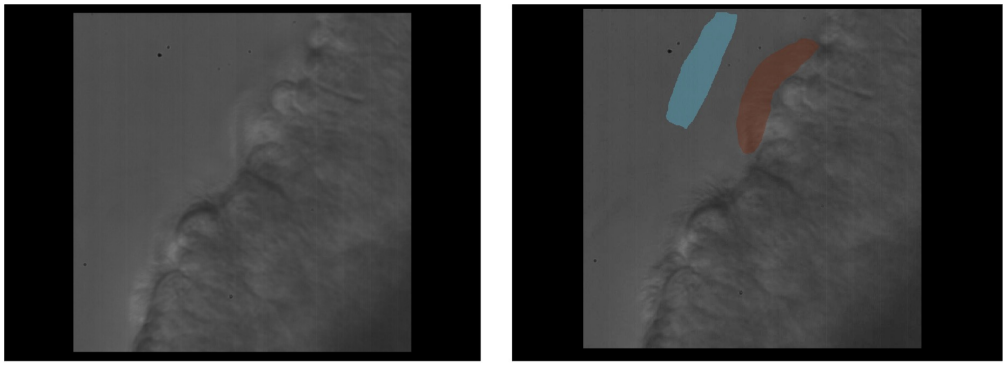

Figure 4.2: Example of cilia density determination. (Left) Original frame image. (Right) The blue block corresponds to the background. The brown block corresponds to the cilia area.

4.2.7 Manual Segmentation of Cilia

For each video, we used napari (261), an interactive image viewer for Python, for manual segmentation of cilia. First, we created a new label layer and adjusted the opacity. Then, a paint brush was activated to draw the contour of the cilia area. After filling the contour with the bucket, the label can be converted into a segmentation image.

4.2.8 Statistical Analysis

CBFs are presented as means $\pm$ standard deviation. Statistical analysis was assessed by ANOVA. Comparison of paired-data was done using a paired-samples t test. A value of $P < 0.05$ was considered statistically significant.

4.3 Results

4.3.1 Dataset Vocabulary

We built a validation dataset of 872 videos of cilia motion under four categories: drug, temperature, ACE2, and control. We also generated ground-truth masks labelling cilia areas, which can be used for evaluating segmentation performances. The truncated video dataset is available at: `https://doi.org/10.5281/zenodo.8135892`. Figure 4.3 showed sample videos and their ground-truth masks with cilia area labelled. Drug treatment accounts for the largest proportion (73.6%) of videos. Under drug category, we imaged cilia motion with seven different drugs under different concentrations (Table 4.2). The number of videos in each category is shown in the histograms (Figure 4.4).

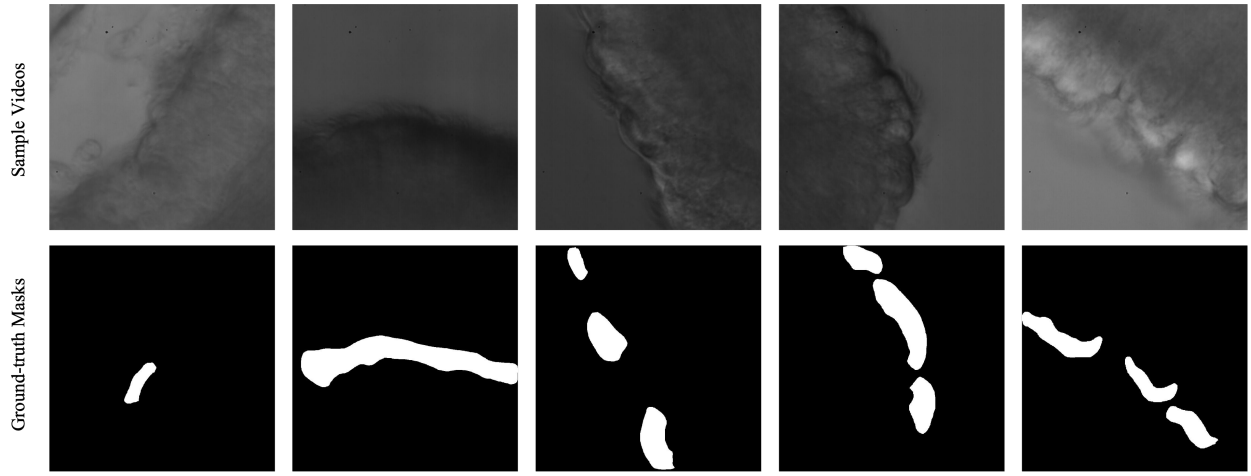

Figure 4.3: Sample videos of cilia motion and their ground-truth masks. Top row shows sample frame images of cilia videos. Bottom row shows their corresponding ground-truth masks with cilia area labelled.

4.3.2 Effects of Different Temperatures on Mouse Airway Ciliary Motility

Previous studies have shown that CBF can be affected by temperatures (211; 262; 237; 242). We recorded cilia motion at several temperatures (18°C, 22°C, 24°C, 26°C, 29°C). The mean CBF at room temperature (22°C) was 5.54Hz (SD 1.1). We found that at 4°C, cilia were almost immotile (data not shown). Figure

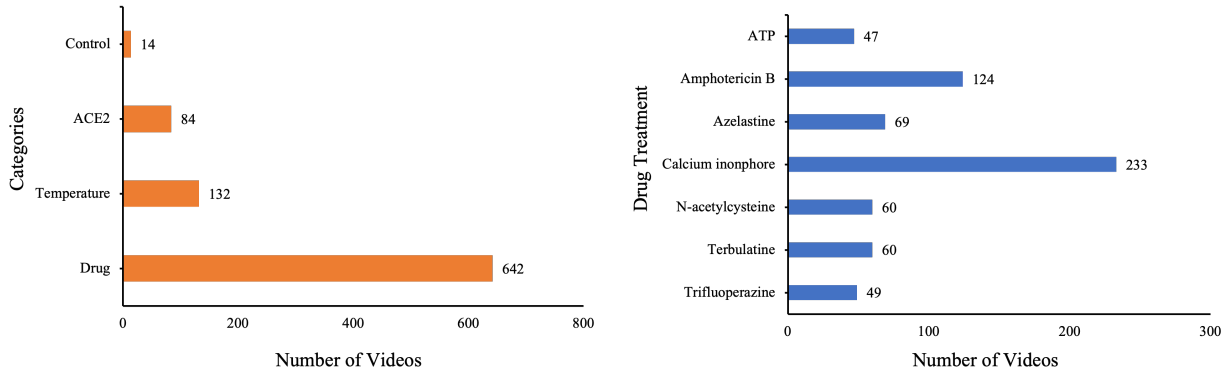

Figure 4.4: Cilia dataset statistics. (Left) Distribution of the number of videos under each category. (Right) Distribution of the number of videos that belong to each drug treatment under drug class.

4.5 shows the CBF at different temperatures. From 22°C to 29°C, CBF values increased with temperature, from 5.54 $\pm$ 1.11 Hz at 22°C to 7.60 $\pm$ 0.82 Hz at 29°C ($P < 0.001$). The beat pattern of mouse airway cilia showed normal forward and backward strokes within the same plane at different temperatures.

4.3.3 Effect of Drugs on CBF

Adenosine 5-triphosphate (ATP) is a purinergic agonist that stimulates CBF by increasing intracellular calcium concentration ($[Ca^{2+}]_i$) (263). Before ATP infusion, CBF was measured as 5.28 $\pm$ 0.67 Hz. We incubated the samples at different concentrations of ATP (1 μM, 10 μM, 100 μM, 1 mM) for 10 minutes before imaging. After ATP infusion, we replaced the media with normal L-15 media and recorded cilia motility. We found that ATP slightly increased the CBF values of mouse tracheal samples, although the difference was not significant (Figure 4.6A).

Amphotericin B is an antifungal agent commonly used to treat allergic fungal rhinosinusitis. At room temperature, the baseline of CBF before Amphotericin B perfusion was 6.97 $\pm$ 1.11 Hz. At 25 μg/mL, CBF was reduced to 5.44 $\pm$ 0.46 Hz ($P < 0.0001$). After re-perfusion with normal media, CBF

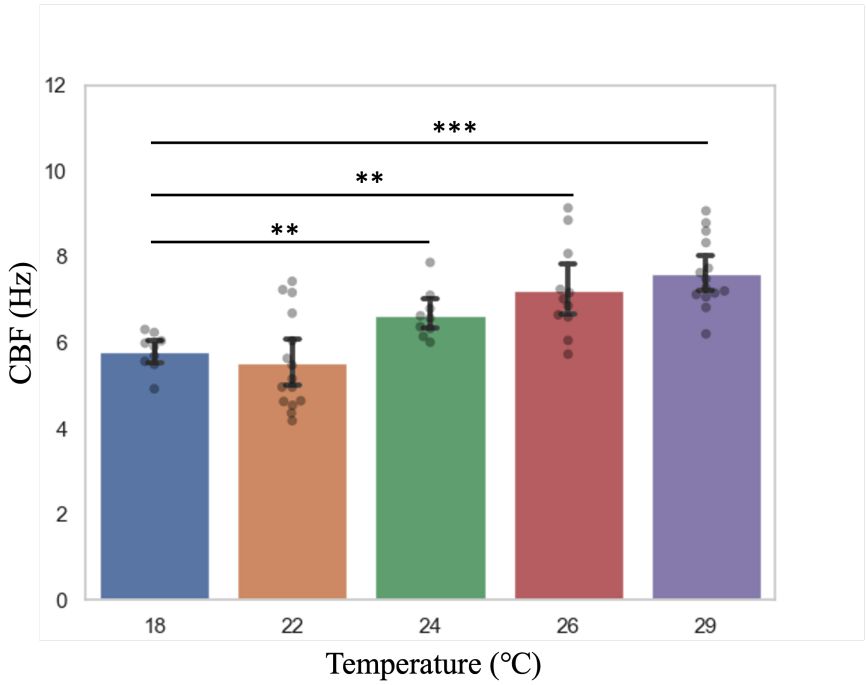

Figure 4.5: CBF analysis at different temperatures. Data are shown as mean ± SD. CBF is increased when measured at high temperatures. *, P < 0.05; **, P < 0.01; ***, P < 0.001.

value was elevated to 5.98 ± 0.87 Hz but still lower than baseline CBF (P < 0.01) (Figure 4.6B). Overall, Amphotericin B has an inhibitory effect on cilia motility.

Azelastine is an anti-allergy drug for intranasal use. Previous studies report inconsistent results on whether azelastine has an effect on CBF (264; 249). In the current study, we found that azelastine reduced CBF values at 10 μM (5.53 ± 0.5 Hz, P = 0.386) (Figure 4.6C). Calcium can regulate CBF by increasing $[Ca^{2+}]_i$ (250; 265). Di Benedetto and colleagues exposed human nasal epithelial cells with 4-bromo-calcium ionophore A23187 (4-Br-A23187) and found that 4-Br-A23187 increased CBF in a time-dependent manner (250). Sánchez-Cárdenas *et al.* treated spermatozoa with calcium ionophore A23187 and found that sperm were immobilized after 10 min (266). In the current study, we treated mouse tracheal samples with calcium ionophore A23187 and found that A23187 decreased CBF in a dose-dependent manner

Table 4.3: Effects of drugs on CBF

Drug Name	Effect
ATP	No effect
Amphotericin B	Decrease
Azelastine	Decrease
Calcium inonphore	Decrease
N-acetylcysteine	Decrease
Terbutaline	No effect
Trifluoperazine	Decrease

(Figure 4.6D), consistent with Sánchez-Cárdenas' results. Removing A23187 can partially restore the CBF.

N-acetylcysteine amide (NAC) is widely used as a mucolytic agent. At low concentration (0.5 mg/mL), NAC has no effect on CBF. At high concentration (1 mg/mL), NAC decreased CBF ($P < 0.001$). After its removal, CBF was not restored ($P < 0.01$) (Figure 4.6E). Terbutaline is a β2-adrenergic agonist known to increase CBF in a dose-dependent manner (255). We treated mouse tracheal samples with terbutaline at 0.5 μM and 10 μM. After terbutaline perfusion, CBF was only slightly increased compared to the baseline CBF, but the difference was not statistically significant ($P = 0.515$) (Figure 4.6F). Trifluoperazine (TFP) is an inhibitor of calmodulin-sensitive calcium-dependent protein kinases. TFP is known to decrease CBF (250). We treated mouse tracheal samples with TFP and found that TFP reduced CBF in a dose dependent manner (Figure 4.6G). The effects of these drugs on CBF is summarized in Table 4.3.

4.3.4 Effects of ACE2 manipulation on CBF

Under control conditions, the mean CBF of mouse tracheal explants was 5.54 $\pm$ 1.11 Hz (mean $\pm$ SD). The mean CBF of mouse tracheal explants was 5.75 $\pm$ 0.48 Hz (mean $\pm$ SD). There was no significant difference ($p > 0.05$) between control group and the ACE2 inhibitor group.

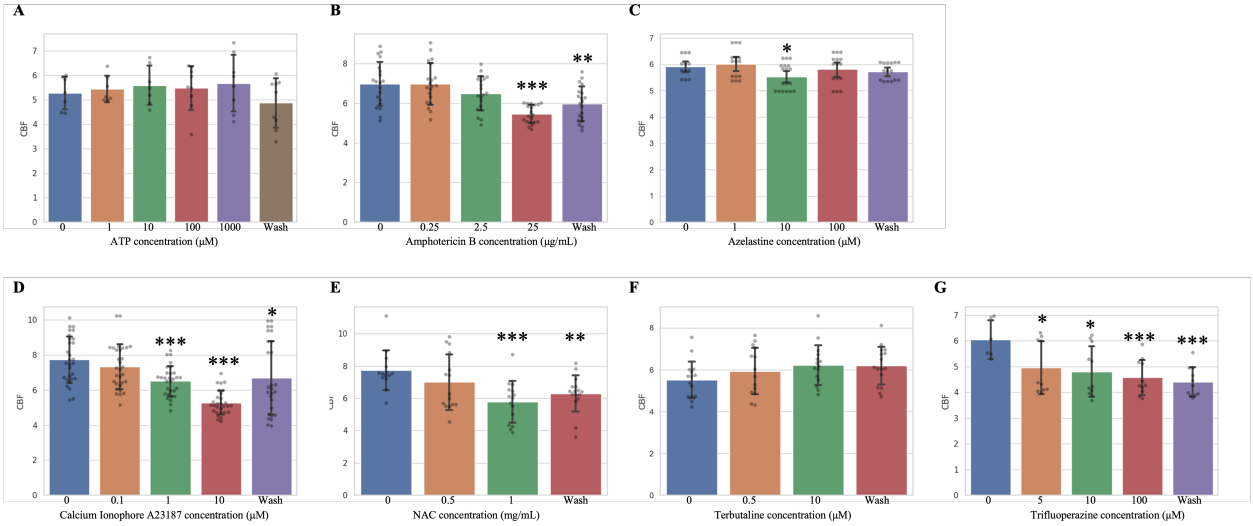

Figure 4.6: Analysis of the effects of selected drugs on CBF relative to control. Mean CBF after exposure to different concentrations of drugs at room temperature. The effects of ATP (**A**), Amphotericin B (**B**), azelastine (**C**), calcium inonphore A23187 (**D**), NAC (**E**), terbutaline (**F**), trifluoperazine (**G**) at different concentrations on CBF relative to control. *, $P < 0.05$; **, $P < 0.01$; ***, $P < 0.001$.

For ACE2 genetic manipulation, we treated mouse tracheal explants with scramble lentivirus and two ACE2 shRNA (Variant 1 and 3) variants. After 40 hours of incubation, the results of the mean CBF values of the treatment groups are given in Figure 4.7. ACE2 shRNA lentivirus slightly increased CBF compared to the control and scramble groups, but the difference was not statistically significant ($P > 0.05$).

4.4 Discussion

In the current study, we presented a large-scale validation dataset of ciliary motion phenotypes. Our dataset is comprised of over 800 videos (more than 1,200,000 frames). The ground-truth masks for segmenting ciliary area were provided using Napari, a Python library for image visualization and annotation (261). Ciliary motion of mouse tracheal samples after treatment with various drugs, temperatures, and gene

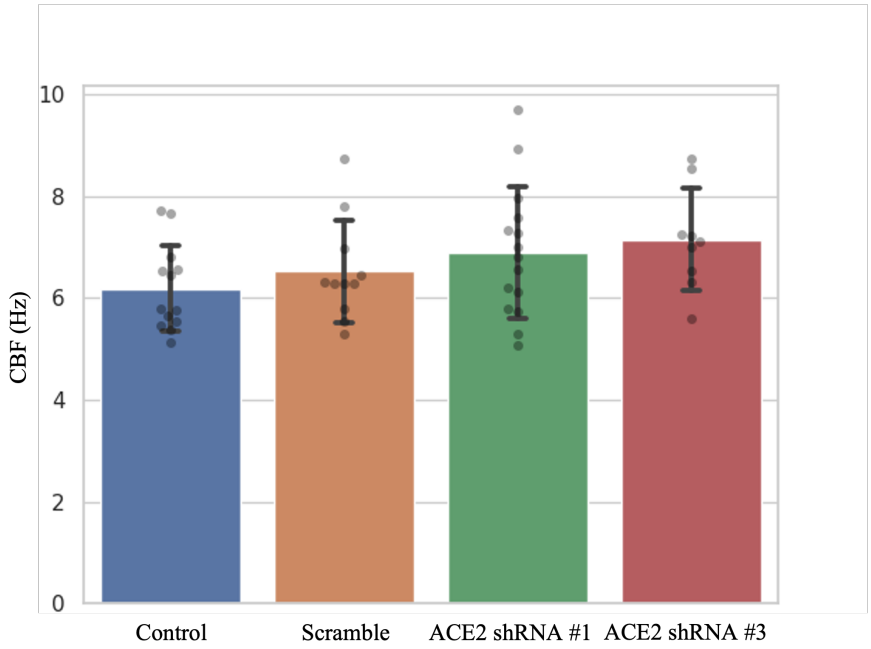

Figure 4.7: ACE2 shRNA effects on ciliary beat frequency. Mean CBF after exposure to scramble and ACE2 shRNA lentiviruses was measured.

manipulation (ACE2) were recorded at 250 frames per second using a high-speed CCD video microscope. The mean CBF $\pm$ SD was calculated using FFT as a baseline metric for characterizing ciliary function.

The CBF of airway epithelia in healthy individuals varies from 10 to 20 Hz (267; 268). In the present study, the videos were obtained at room temperature (22°C) except in the case of temperature treatments. The CBF values of our control samples are 5.3 $\pm$ 1.3 Hz, lower than those in in vivo condition. Jing *et al.* measured the CBF at 25°C as 5.1 Hz (150), consistent with our results. Christopher *et al.* reported that cilia-generated flow velocity declined with the decrease of temperature (240). Nikolaizik *et al.* analyzed nasal brushings from young adults and found no obvious changes in the beating pattern of cilia at the different temperatures (242). Future studies can involve high temperatures to mimic in vivo conditions such 32°C for nasal cilia and 37°C for tracheal cilia.

Many drugs and compounds have been found to affect cilia beat frequency (164). ATP stimulates CBF in cultured ciliated cells and tracheal explants through increasing $[Ca^{2+}]_i$ (269). Amphotericin B is often

used as an antifungal treatment for diseases such as allergic fungal rhinosinusitis. Hofer *et al.* reported that amphotericin B (0.1 mg/mL) in distilled water caused a reduction of CBF after a 20 min incubation (246). Azelastine is a drug commonly used for treating allergic rhinitis. Previous studies have found that azelastine can reduce CBF (249; 270). Previous literature showed controversial results regarding the effect of azelastine on CBF (249; 264). We evaluated the effect of azelastine on mouse tracheal explants and found that azlestine at 10 μM can reduce CBF. Calcium plays an important role in regulating ciliary activity (271). We found that mouse airway cilia treated with the calcium ionophore A23187 exhibited reduced CBF in a dose dependent manner. Di Benedetto and colleagues reported that 10 μM calcium ionophore 4-Br-A23187 increased the CBF values of human respiratory epithelial cells (250). However, A23187 can immobilize spermatozoa while induce the acrosome reaction (272). Sánchez-Cárdenas *et al.* also found that A23187 at 5–10 μM can elevate $[Ca^{2+}]_i$ and immobilize spermatozoa. However, high concentrations of A23187 can increase flagellar beat frequency (266). Future studies should involve higher concentrations (>10 μM) of A23187 to examine the effects of calcium ionophores on ciliary function. NAC is extensively used for the treatment of cystic fibrosis (CF). Orally administered NAC in CF patients can significantly improve their lung function (273). We found that NAC reduced CBF, which is consistent with previous studies (253; 252).

One limitation of the study is that we only provided CBF as baseline metrics for all the videos. CBF can provide basic information of ciliary function, but it cannot provide the synchronicity and pattern of beating cilia. Although we developed computational methods to analyze CBF metrics including length, density, ciliary beating angle, and amplitude, this pipeline still requires user input to manually track the beating cycle of a cilium. Studies analyzing the beating pattern of respiratory motile cilia rely heavily on expert interpretation or manual tracking (178; 163; 156; 180; 274; 275). Currently, automated tracking of flagella, in which individual particles (or cells) can be easily detected without overlapping, has achieved great success (276; 277; 179). For future work, automated computational tools should be developed to calculate the metrics that characterize ciliary beating waveforms.

In conclusion, we present a large-scale video validation dataset of ciliary motion phenotypes under several categories (drug, temperature, ACE2 manipulation). This dataset consists of 872 videos at 200 frames/sec obtained using a high-speed video microscope. The CBF values of each video are provided as baseline metrics. This is the first open-source video dataset of ciliary motion that can serve as a resource for the CS community and researchers to develop models for image segmentation and characterizing ciliary motion.

Chapter 5

Gabor Filter Incorporated U-Net for Cilia Segmentation

[1]

5.1 Introduction

Cilia are hair-like structures found on the surface of nearly all eukaryotic cells in vertebrates and play an important role in many biological processes such as fluid movement and cell locomotion. Motile cilia beat in a coordinated manner to propel the pathogens and debris out of the airway. The coordinated beating of cilia plays a key role in maintaining effective mucociliary clearance (MCC), which is the primary innate defense mechanism of the lung (12). Dysfunction of cilia causes severe diseases known as ciliopathies, including primary ciliary dyskinesia (PCD) and polycystic kidney disease (PKD), which lead to chronic lung infections and fluid-filled cysts, respectively (77; 76). Therefore, the effective analysis of ciliary function is critical in the diagnosis of cilia-related diseases. Currently, the assessment of ciliary function and characteristics remains challenging, and a fundamental part of overcoming this challenge is effective cilia segmentation, which is to identify and label ciliary area from images.

[1] Content of this section is based in part on my master thesis (108)

Image segmentation is a computer vision technique of splitting image data into multiple segments, which reduces the data complexity and allows for further processing and analysis. Cilia segmentation can help to reduce background information and filter useful information for future quantitative cilia analysis or cilia motion phenotyping. Cilia are tiny structures compared to the other cellular compartments; therefore, it is difficult to segment cilia from differential interference contrast (DIC) images. Figure 5.1 shows an example of an original frame image and its corresponding ground-truth mask. To detect cilia, many approaches have been developed (e.g. ACDC (111), CiliaQ (16)); however, those tools either rely on the user's manual correction or fluorescent labels to identify cilia, and therefore, would not work on DIC images for cilia segmentation. Previous studies have used traditional image processing and deep learning-based methods for cilia segmentation of DIC images (17; 112; 18; 113). However, the model performances are not quite satisfactory.

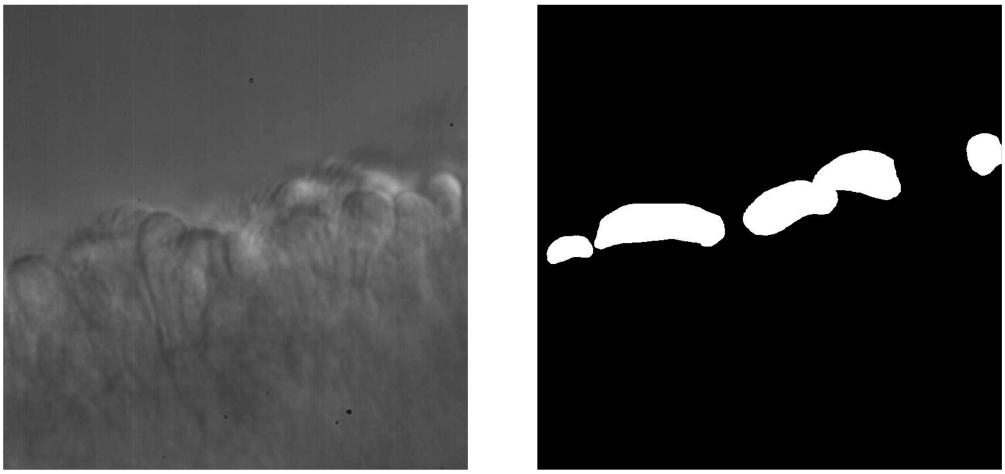

Figure 5.1: Example of a cilia image (left) and its ground-truth mask (right). Left, the cilia image is a 800x800 DIC image of mouse trachea. Right, the ground-truth mask generated with napari shows the cilia area in white.

Gabor filter (GF) is a linear filter widely used for recognizing patterns with different orientations and frequencies for texture analysis (278; 279; 280; 281); therefore, we proposed to use GF for highlighting and extracting cilia features. Since the performances of current deep learning-based approaches for cilia segmentation are not ideal, we proposed to combine GF with U-Net to improve model performances. Although U-Net itself can perform feature extraction and localization, U-Net architecture capability is

limited in localizing objects with non-standard shape (282). Additionally, modifying the architecture or layer is an intricate task.

To improve the performance of the U-Net model in cilia segmentation, we proposed to use GFs for feature extraction and combine them with the U-Net framework for generating cilia segmentation maps. We generated a set of GFs and used random forest to select GFs with high feature importance based on permutation importance. Then, the Gabor filtered feature maps are concatenated to the original image as an additional channel to train the U-Net model. The addition of features extracted by our selected GFs improved the performances of the base model.

5.2 Related Work

5.2.1 Image Segmentation

There are two types of image segmentation: semantic segmentation, which detects multiple objects within a category as one entity, and instance segmentation, which distinguishes between different instances of the same category. Semantic image segmentation is important for image analysis in removing background noises, improving precision, and area detection. It is also a difficult task in computer vision and digital image processing. Traditional approaches, such as thresholding and watershed, compare pixel values in order to achieve the segment map. With the development of deep learning and neural networks, there are many tools and architectures developed for image segmentation (1; 283; 284; 285; 286). For cell segmentation, several bio-image segmentation tools, including StarDist (120), PlantSeg (121), Cellpose (110), and LABKIT (122), have achieved great performances. However, most state-of-the art segmentation methods require a large dataset with human-labelled ground-truth data for training. Fully Convolutional network (FCN) was first introduced by Long and colleagues (123). FCN can train end-to-end and use skip connections to enhance image segmentation. U-Net (1) is a U-shape convolutional network architecture containing encoder layers and decoder layers. The encoder block reduces the spatial dimensions of the image, while the decoder repairs the details in the spatial dimension of the image. However, the drawback of U-Net

is that it fails to separate objects when they are crowded or overlapped. The usage of skip connections would need redundant information, causing training overhead.

For the cilia segmentation task, Quinn *et al.* developed a computational pipeline to classify cilia motion (17). In this framework, the authors used intensity-based thresholding to segment cilia area from frame images. The authors calculated the standard deviation of the time-varying intensity changes at each pixel value and constructed a histogram. The distribution peak is set as the pruning threshold value to segment cilia. This method achieves a simple and fast segmenting map; however, the threshold value is specific to each experimental setting. Lu *et al.* developed an end-to-end pipeline utilizing a densely-connected convolutional network (DenseNet) with 74 layers to automatically recognize cilia area (112). This proposed framework achieved an accuracy of 86.2% in cilia segmentation. Zain *et al.* modified Lu's model and built a fully Connected DenseNet with 103 layers. This model achieved a IoU score of 33.06% and a accuracy of 88.3% (18). In a most recent work, Zain and Miller combined zero-phase PCA sphering (ZCA) and Sparse Autoencoders (SEA), which served as low-level feature extraction, with U-Net (113). This new model achieved a 10% improvement with an IoU of 0.441 and an accuracy of 77%. However, parameter selection and hypertuning for the composite models is computationally expensive and labor intensive.

5.2.2 Gabor Filter

Gabor filter (GF), named after Dennis Gabor, is a linear filter commonly used for feature extraction, texture analysis, edge detection, etc. The Gabor wavelets are defined as follows:

$$g(x, y; \lambda, \theta, \psi, \sigma, \gamma) = exp([-\frac{x'^2 + \gamma^2 y'^2}{2\sigma^2})exp[i(2\pi\frac{x'}{\lambda} + \psi)]$$

$$x' = x\cos\theta + y\sin\theta$$

$$y' = -x\sin\theta + y\cos\theta$$

where λ represents the wavelength of the sinusoidal component, θ represents the orientation from normal to the parallel stripes of the Gabor function, ϕ represents the phase offset, σ is the standard deviation of the Gaussian envelope, and γ is the spatial aspect ratio specifying the ellipticity of the support of the Gabor function.

A response matrix can be obtained by convolving the original image I(x,y) with the GF as follows:

$$R(x, y; \lambda, \theta, \psi, \sigma, \gamma) = \sum_{x'} \sum_{y'} I(x - x', y - y') g(x', y'; \lambda, \theta, \psi, \sigma, \gamma)$$

By manipulating the parameters λ, θ, ψ, σ, and γ, a GF bank can be generated with a set of different GFs.

To improve the performances of deep learning models, several studies incorporate low-level feature extraction to aid deep learning frameworks (127; 128; 113). Luan *et al.* proposed to incorporate Gabor filters into the deep convolutional neural networks (DCNNs) (127). This framework effectively reduced the training complexity and improved performances over several benchmarks. Reyes and colleagues proposed an approach combining GF with U-Net for image segmentation (128). The proposed framework outperformed U-Net and other state-of-the-art architectures in mIoU and Dice scores on two benchmark datasets (the ISLES 2018 dataset and the 2018 Atrial Segmentation Challenge dataset). However, this work is relatively computationally expensive and inefficient because the input contains the original dataset plus additional features extracted by a whole set of GFs. Some of the filters extract meaningless feature information compared to the other filters in the bank. Therefore, an optimized GF bank with selected parameters is critical in the performance of the GF-embedded U-Net architecture for specific segmentation tasks.

5.3 Methodology

5.3.1 Cilia Dataset

The cilia dataset is from the previous study (Chapter 4). Briefly, we built a large-scale video dataset of ciliary motions containing 872 videos and 872 ground truth masks of ciliary area. The cilia videos are

recorded at 250 frames per second (fps) for 6 seconds in Differential Interference Contrast (DIC) setting. Each frame is 800 x 800 pixels. For the segmentation task, we took the first frame of each video as the image data. For image preprocessing, we cropped the original images and their corresponding masks into small patches of 128 x 128. After cropping, we removed the patches containing less than 5% cilia area. Finally, the cilia dataset consists of 7221 image patches and 7221 mask patches. In addition, we split the cilia dataset in a ratio of 8:2 for training and testing sets. During the training process, 20% of the data is split for validation purpose. Table 5.1 shows the number of images and masks for training, validation, and test.

Table 5.1: The number of images and masks for training, validation, and testing

Type	Training (# of images)	Validation (# of images)	Test (# of images)	Total (# of images)
Images	4620	1156	1445	7221
Masks	4620	1156	1445	7221

5.3.2 Gabor Filter Bank

In this study, we generated a GF bank consisting of 54 GFs with various parameters for cilia images so that the outputs highlight cilia patterns and edges (Figure 5.2). This GF bank is achieved with the following parameters: θ: {π/4, π/2, π*3/4}; σ: {1,3}; λ: {π/4, π/2, π*3/4}; γ: {0.05, 0.25, 0.5}; ϕ: {0}. The kernel size is set as 9.

By applying the GF bank to a cilia image, we achieved a set of convoluted outputs. Figure 5.3 shows a visual example of the GF bank applied to a sample cilia patch image. The output figures showed a variety of highlighted patterns and edges based on the orientation of GFs. Some of the filtered images present highlighted cilia textures. There are also meaningless filtered outputs with all 0-value pixels.

5.3.3 Random Forest

To select the Gabor filters with the highest importance, we use the Random Forest (RF) algorithm to compute feature importance. We train the RF model with the 54 Gabor filtered vectors and the original

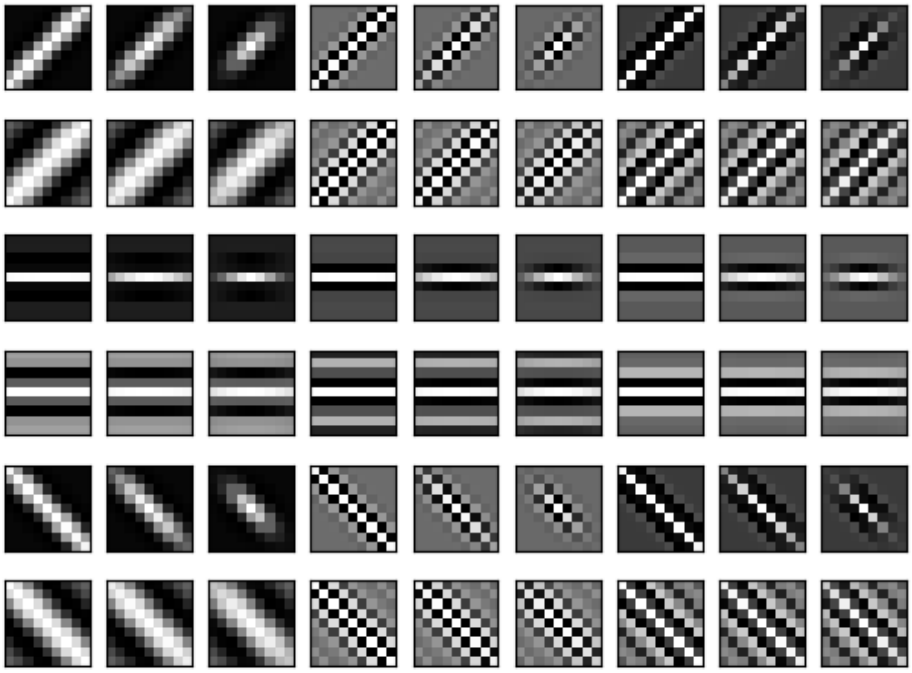

Figure 5.2: Gabor filter bank. Different Gabor filters with different parameter values for θ, σ, λ, and γ will change filter properties.

image vector for image classification (0 for non-cilia and 1 for cilia). After training and prediction, the permutation-based importance is implemented using permutation_importance method with scikit-learn.

5.3.4 Experimental Setup

For the U-Net and composite models, we run the experiments for a total of 250 epochs with a batch size of 16. We use Adam optimizer and binary cross-entropy (BCE) loss function. For learning rate, we use learning rate monitor from PyTorch Lightning, which automatically monitors and logs learning rate for learning rate schedulers with a log rate of 10 during training. We train our models on 2x NVIDIA TITAN X GPU cards and NVIDIA Quadro RTX 5000.

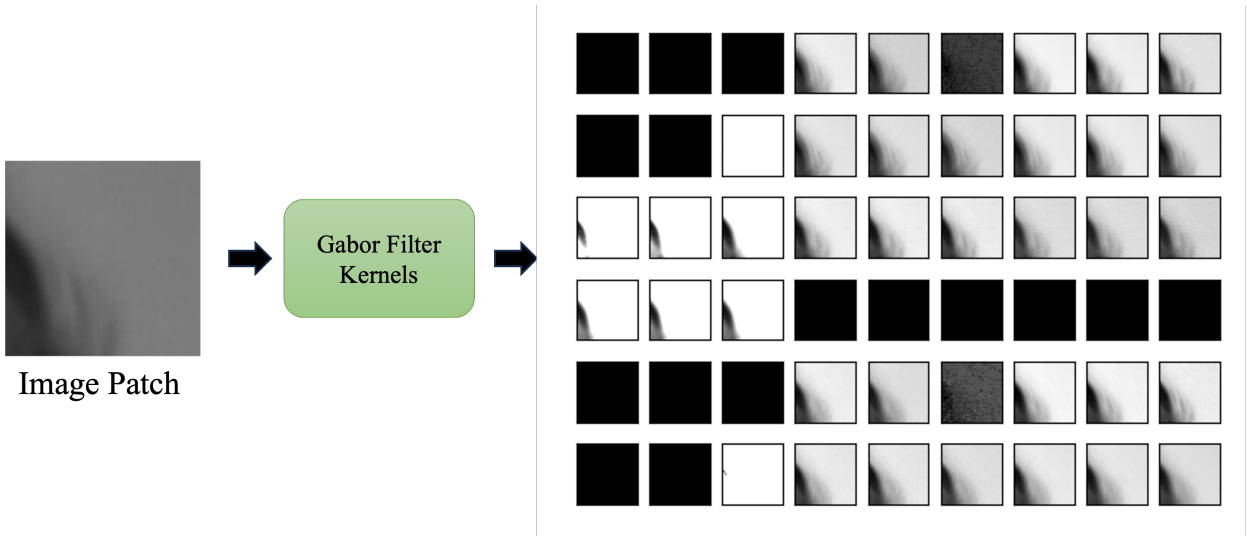

Figure 5.3: Illustration of GFs applied to a sample cilia patch. When an image patch is convolved with the GF bank kernels, the resultant images show a variety of highlighted edges and patterns according to the orientation and frequency of different GFs.

5.3.5 Evaluation Metrics

For image segmentation tasks, we use metrics including Intersection over union (IoU), accuracy, precision, recall, and F1 to evaluate our model performances of cilia segmentation.

IoU, also referred to as Jaccard similarity, can evaluate how similar a predicted mask is to the ground-truth mask. It measures the number of pixels common between the target and prediction masks divided by the total number of pixels present across both masks. IoU score ranges between 0 to 1, where 0 means no overlap and 1 indicates perfect overlap. IoU can be calculated as following:

$$IoU = \frac{\text{Area of Overlap}}{\text{Area of Union}}$$

Pixel accuracy is simple to report and commonly used for semantic segmentation. It is a metric to compare each pixel with the ground-truth mask. There are two drawbacks of accuracy for semantic

segmentation. First, it can provide misleading results when there is a class imbalance. Second, pixel accuracy is informative as a standalone metric.

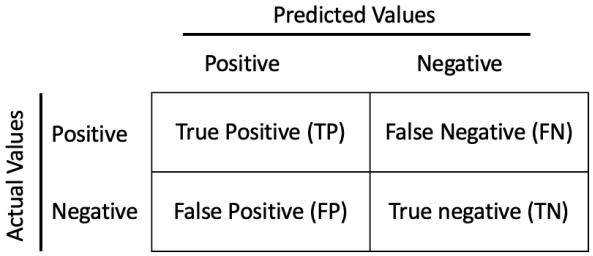

Figure 5.4: Confusion matrix

We also use the confusion matrix to evaluate the accuracy of the model's performance. A confusion matrix is generated using scikit-learn and presents four numbers: true negative (TN), false negative (FN), false positive (FP), and true positive (TP) (Figure 5.4). From the confusion matrix, we can calculate metrics including precision, recall, and F1. Precision is a measure of quality, indicating how precise the model is. Recall is a measure of quantity, indicating how many times the model returns truly relevant results. F1 score, or Dice similarity coefficient, is a harmonious mean of precision and recall. The accuracy, precision, recall, and F1 scores are computed as follows:

$$Accuracy = \frac{TP + TN}{TP + FP + FN + TN}$$

$$Precision = \frac{TP}{TP + FP}$$

$$Recall = \frac{TP}{TP + FN}$$

$$F1 = \frac{2 * Precision * Recall}{Precision + Recall}$$

5.4 Experiments

We extracted features through the bank of 54 GFs with various parameters, and then we trained RF with the original image vector and 54 feature vectors. The most relevant features and their GFs that contributed most to the segmentation accuracy were selected for training the U-Net model. Table 5.2 shows the list of GFs and their parameters selected by RF.

Table 5.2: Selected Gabor filters

Gabor filter names	θ	σ	λ	γ	ϕ
Gabor 4	$\pi/4$	1	$\pi/2$	0.05	0
Gabor 22	$\pi/2$	1	$\pi/2$	0.05	0
Gabor 24	$\pi/2$	1	$\pi/2$	0.5	0
Gabor 25	$\pi/2$	1	$\pi^*3/4$	0.05	0
Gabor 26	$\pi/2$	1	$\pi^*3/4$	0.25	0
Gabor 49	$\pi^*3/4$	3	$\pi/2$	0.05	0

For cilia segmentation, we trained the U-Net model with the image patches as a baseline, then we trained the U-Net model with the original image concatenated with an additional Gabor-filtered image. Figure 5.5 illustrates sample images filtered by the selected six GFs. The models were trained for 250 epochs with a batch size of 16. All networks were imported in PyTorch, a Python library for building deep learning models. We evaluated the models with five metrics: Intersection over Union (IoU), accuracy, F1 score, precision, and recall.

Table 5.3 provides a summary of experiments performed with selected GFs. The U-Net base model trained with the original image as a single channel achieved an IoU of 0.4386, accuracy of 0.7667, F1 of 0.5622, precision of 0.5730, and recall of 0.6415. Gabor 22 composite model achieved the highest IoU score (0.4450) and F1 score (0.5658). Several of our GF composite models (e.g, Gabor 22, 24, 25, 26, 49) improved the model performance with a higher accuracy score. Gabor 25 composite model achieved the highest precision (0.6190). The U-Net base model achieved the highest recall score of 0.6415. Overall, the

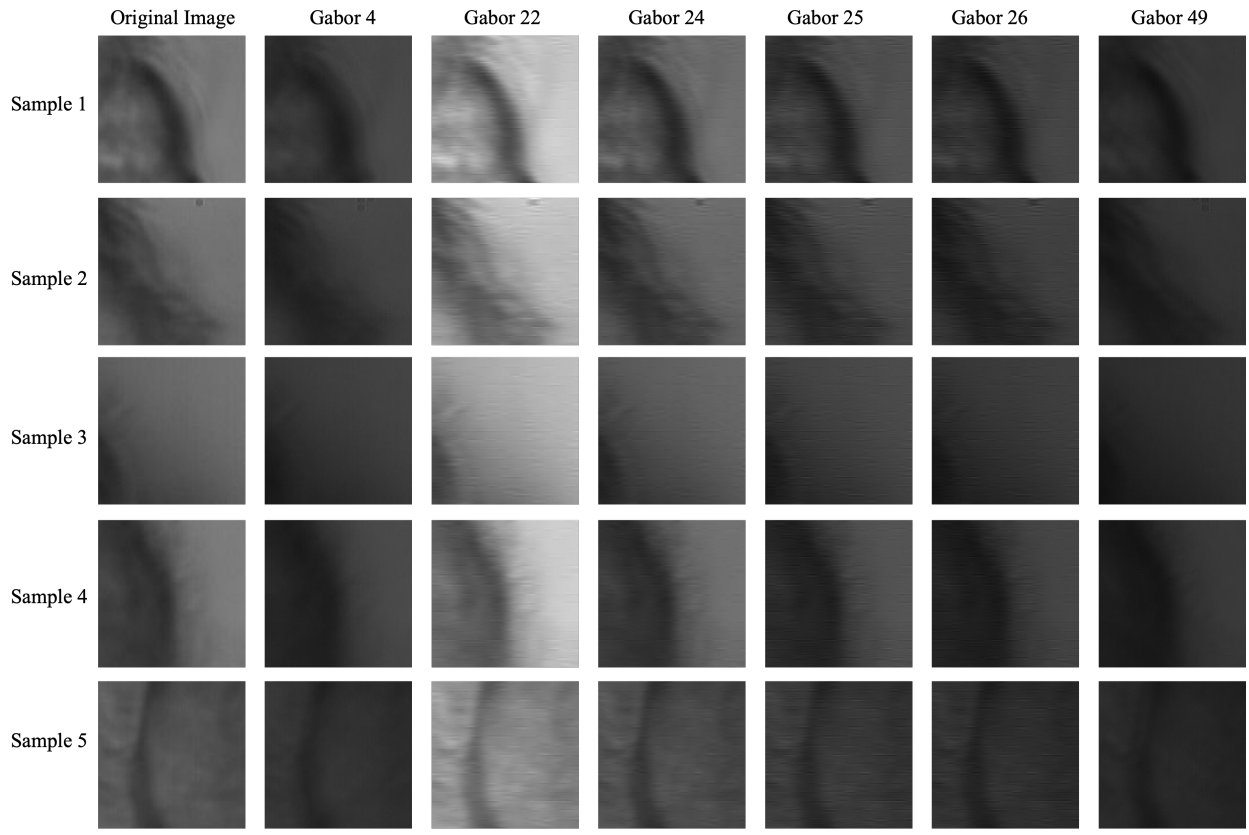

Figure 5.5: The visual illustration of filtered outputs of cilia images. The original image patches are 128x128 DIC images of mouse trachea. After passing them through the selected Gabor filters, cilia patterns are highlighted.

Gabor composite models improved the performances of the base model in terms of IoU, accuracy, F1, and precision.

Figure 5.6 shows a qualitative comparison of cilia segmentation results. The U-Net base model predicted the cilia area that is indicated in the ground-truth masks. For sample 2 and 3, the U-Net-segmented maps shrank the cilia area compared to the ground-truth masks. However, the outputs from Gabor 22 and Gabor 24 composite models retained or enlarged the cilia area, which is beneficial for further video analysis. For sample 4 and 5, Gabor 49 composite models included false positives. Overall, the composite

Table 5.3: Performances of Gabor U-Net models over the cilia dataset

Model	Evaluation Metrics				
	IoU	Accuracy	F1	Precision	Recall
U-Net	0.4386	0.7667	0.5622	0.5730	**0.6415**
Gabor 4+U-Net	0.4328	0.7639	0.5546	0.5744	0.6302
Gabor 22+U-Net	**0.4450**	0.7808	**0.5658**	0.6027	0.6248
Gabor 24+U-Net	0.4214	0.7774	0.5347	0.5814	0.5782
Gabor 25+U-Net	0.4202	**0.7920**	0.5331	**0.6190**	0.5438
Gabor 26+U-Net	0.4346	0.7760	0.5510	0.5937	0.6034
Gabor 49+U-Net	0.4356	0.7670	0.5573	0.5948	0.6151

models with the selected GFs tend to be more accurate in recognizing cilia with fewer false negative cilia areas in comparison with the base U-Net model.

5.5 Discussion

In this study, we proposed to use GF to extract features and then train the U-Net model with the large-scale cilia dataset for cilia segmentation. Overall, five out of six of the Gabor composite models achieved better performances in terms of the pixel accuracy than the U-Net baseline model. Gabor 22 composite achieved the highest IoU score (0.4450) and F1 score (0.5658). Some of the composite models with GF extracted features predicted more accurate segmentation masks with fewer false negative cilia areas than the U-Net base model. The Gabor composite models improved the performance of the base model by up to 8% in terms of precision. Cilia segmentation is the fundamental step in the study of ciliogenesis and ciliopathies. Cilia are small hair-like structures which only appear in a small percentage of the image. This increases difficulties for both manual and generated masks. Successful segmentation can detect cilia from background or cells. After segmentation, quantitative cilia analysis, such as cilia length, density and cilia beat pattern, can be estimated.

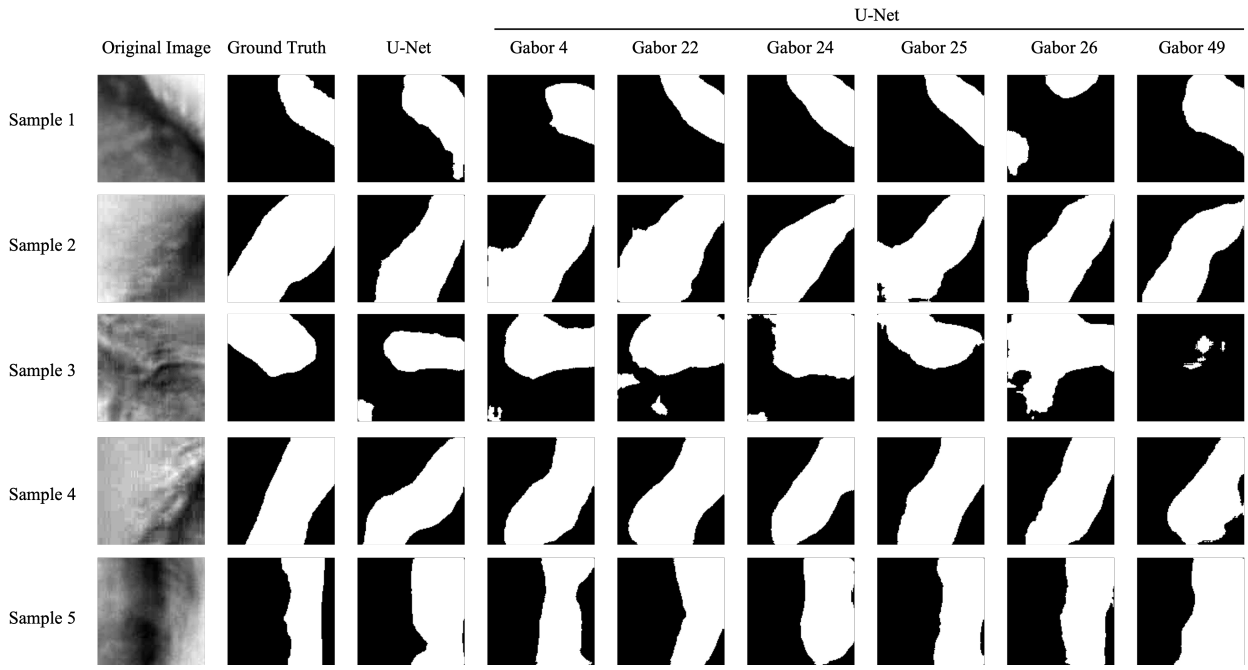

Figure 5.6: The visual comparison of cilia segmentation outputs. The original images are 128x128 DIC images of mouse trachea. The ground-truth masks represent the manual segmentation of cilia area. The output from the U-Net base model and Gabor composite models reveal the cilia segmentation results.

During the training process, overfitting can happen if the model learns the training dataset too well and performs well on the training set, but it does not perform well on the data outside of the training set. We trained for 250 epochs for all our models. To avoid overfitting, we used TensorBoard to monitor the learning rate, training, and validation loss. Figure 5.7 shows the generated masks on the validation dataset from the U-Net base model and Gabor 4 + U-Net after 20 epochs. The U-Net model did not produce reliable masks until after 50 epochs, while the Gabor composites models generate masks that are close to the ground-truth masks after 20 epochs.

Cilia constitute a small portion of the video images, which can cause an unbalanced data issue when applied to machine learning. Cilia segmentation is used to classify video images into cilia class and non-cilia class. To examine the balance of our data, we calculated the ratio between the two classes: cilia and non-cilia areas. In the original cilia dataset, cilia only account for 7% while 93% of the pixels are non-cilia

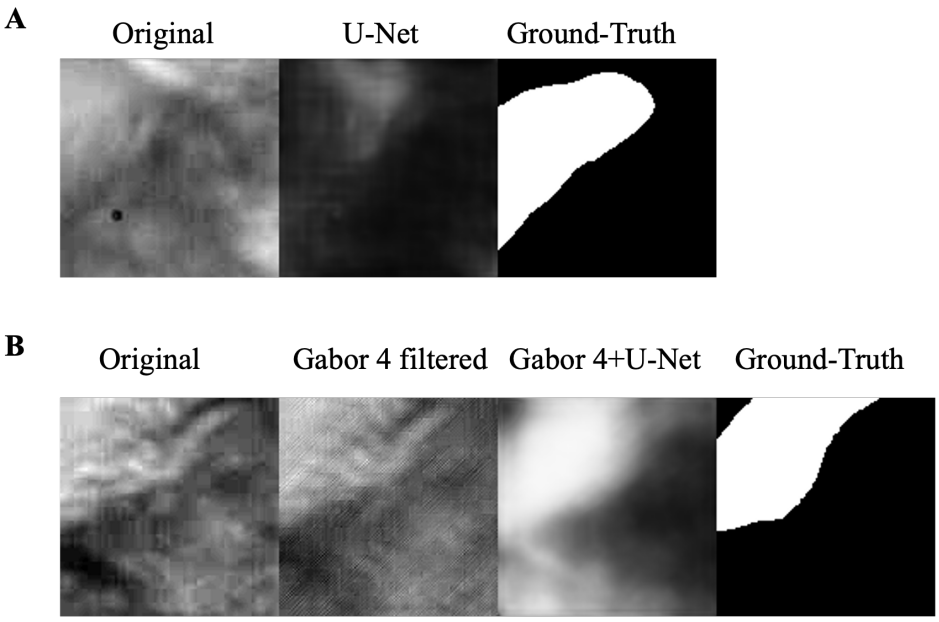

Figure 5.7: Segmentation results during the training process. **A**, representative segmentation output during the training of the U-Net model. **B**, representative segmentation result during the training of the Gabor 4 composite model.

background. After selecting image patches with more than 5% ciliary area, the new dataset consists of 30% cilia and 70% non-cilia. Figure 5.8 shows the distribution of cilia and non-cilia of the datasets before and after selection.

Random forest (RF) is a popular machine learning tool for regression and classification introduced by Amit and Geman (287). RF consists of a multitude of decision trees that operate as an ensemble, thus handling a variety of visual features. RF has high computational efficiency in training and classification, and avoids overfitting. During the training process, each tree randomly picks the features, which provides the opportunity to find the feature that influences the majority of trees. Therefore, we used RF to find the features and their corresponding GFs with maximum importance. Due to high computational cost, we did not apply all filtered images as input for the U-Net model. Instead, we used RF for classifying the generated feature vectors and selecting the GFs that give us the distinguishing features of cilia at the spatial location.

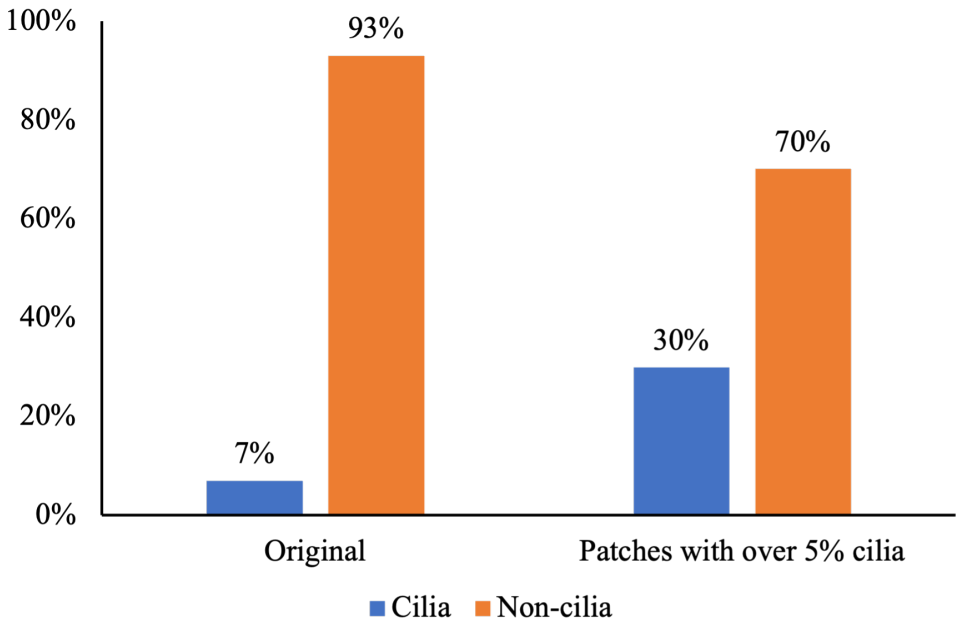

Figure 5.8: Cilia and non-cilia distribution. In the original dataset, cilia only take 7%. After removing image patches with less than 5% cilia area, cilia area is increased to 30%.

In this study, we generated a set of 54 GFs and used random forest to select meaningful GFs with high importance. We picked six selected GFs for feature extraction to aid the U-Net model, instead of embedding GFs into the U-Net encoder, because modifying the U-Net architecture is an intricate task. For future work, we will explore the GF-embedded U-Net for cilia segmentation. We will also focus on developing an optimized GF bank with automatic variation of GF parameters.

5.6 Supplementary Information

5.6.1 Gabor filter bank list

Gabor Filter No.	θ	σ	λ	γ	ϕ
1	$\pi/4$	1	$\pi/4$	0.05	0

2	π/4	1	π/4	0.25	0
3	π/4	1	π/4	0.5	0
4	π/4	1	π/2	0.05	0
5	π/4	1	π/2	0.25	0
6	π/4	1	π/2	0.5	0
7	π/2	1	π*3/4	0.05	0
8	π/2	1	π*3/4	0.25	0
9	π/2	1	π*3/4	0.5	0
10	π/4	3	π/4	0.05	0
11	π/4	3	π/4	0.25	0
12	π/4	3	π/4	0.5	0
13	π/4	3	π/2	0.05	0
14	π/4	3	π/2	0.25	0
15	π/4	3	π/2	0.5	0
16	π/4	3	π*3/4	0.05	0
17	π/4	3	π*3/4	0.25	0
18	π/4	3	π*3/4	0.5	0
19	π/2	1	π/4	0.05	0
20	π/2	1	π/4	0.25	0
21	π/2	1	π/4	0.5	0
22	π/2	1	π/2	0.05	0
23	π/2	1	π/2	0.25	0
24	π/2	1	π/2	0.5	0
25	π/2	1	π*3/4	0.05	0
26	π/2	1	π*3/4	0.25	0

27	π/2	1	π*3/4	0.5	0
28	π/2	3	π/4	0.05	0
29	π/2	3	π/4	0.25	0
30	π/2	3	π/4	0.5	0
31	π/2	3	π/2	0.05	0
32	π/2	3	π/2	0.25	0
33	π/2	3	π/2	0.5	0
34	π/2	3	π*3/4	0.05	0
35	π/2	3	π*3/4	0.25	0
36	π/2	3	π*3/4	0.5	0
37	π*3/4	1	π/4	0.05	0
38	π*3/4	1	π/4	0.25	0
39	π*3/4	1	π/4	0.5	0
40	π*3/4	1	π/2	0.05	0
41	π*3/4	1	π/2	0.25	0
42	π*3/4	1	π/2	0.5	0
43	π*3/4	1	π*3/4	0.05	0
44	π*3/4	1	π*3/4	0.25	0
45	π*3/4	1	π*3/4	0.5	0
46	π*3/4	3	π/4	0.05	0
47	π*3/4	3	π/4	0.25	0
48	π*3/4	3	π/4	0.5	0
49	π*3/4	3	π/2	0.05	0
50	π*3/4	3	π/2	0.25	0
51	π*3/4	3	π/2	0.5	0

52	π*3/4	3	π*3/4	0.05	0
53	π*3/4	3	π*3/4	0.25	0
54	π*3/4	3	π*3/4	0.5	0

Chapter 6

Conclusions

Respiratory cilia are hair-like structures that play an important role in mucociliary clearance, which is the primary defense mechanism of the lung. SARS-CoV-2, the causative agent of COVID-19, utilizes the ACE2 receptor localized on cilia to enter host cells and motile cilia for replication. We report here that ACE2 has a specific localization pattern within airway cilia; Ecto ACE2 localizes to the proximal cilia, while Cyto ACE2 localizes to the whole cilia with proximal enrichment. We also observed that TMPRSS2, a sheddase of ACE2, localizes to the distal region of cilia, indicating that the Ecto ACE2 on the distal compartment of cilia might be removed due to sheddase activity.

Secondly, we constructed a large-scale validation dataset of ciliary motion phenotypes for characterizing ciliary function. We provide benchmark metrics including ciliary beat frequency, length, and density. We also generated ground truth masks labeling ciliary area for image segmentation. This validation dataset can serve as a benchmark for the computer vision community to develop models for characterizing ciliary motion.

Finally, we propose a deep learning pipeline for texture image segmentation using GFs and the U-Net model. We generated a set of 54 GFs and used random forest to select meaningful GFs with high feature importances. The Gabor filtered feature maps are concatenated to the original image input as an additional channel to train the U-Net model with the large-scale cilia dataset. The addition of features extracted by our selected GFs improved the performances of the base model.

Future Directions

For the localization of ACE2 in respiratory cilia, we investigated the localization of the Ecto- and Cyto-domain of ACE2 isoforms 1 and 2. Previous studies relied heavily on commercially-available ACE2 antibodies to study the localization pattern of ACE2 on cilia without identifying the specific ACE2 isoforms (7; 8; 52). Blume *et al.* examined the localization of full-length and short ACE2, and found that ACE2 recognized with antibodies against different domains of ACE2 exhibited slightly different localization but were mainly enriched in the cellular apical regions and motile cilia (9). The authors also noticed the ratio difference of full-length and short ACE2 in different areas including whole and deciliated cells, and cilia. For future directions, more extensive studies on the distribution of all ACE2 isoforms in cilia and cells are needed. Also, the localization of the ecto- and cyto-domain of each ACE2 isoform on ciliated cells should be investigated. Whether ACE2 plays a role in regulating the function of cilia remains unclear. Additional experiments are required to manipulate ACE2 using genetic or pharmacological strategies and analyze the cilia function changes.

We built a large-scale validation dataset of cilia motion phenotypes under different categories and generated ground-truth masks for image segmentation. In the future, an automated pipeline to characterize cilia beat pattern would be very helpful for researchers and clinicians to estimate the function of motile cilia. For cilia segmentation, the current deep learning architectures achieved an IoU score of 0.33-0.44 (112; 18; 113). Adding Gabor filters to the U-Net model can help improve the performances of the base model. Future experiments should focus on embedding Gabor filters to the encoder of the U-Net model.

Bibliography

[1] O. Ronneberger, P. Fischer, and T. Brox, "U-net: Convolutional networks for biomedical image segmentation," in *Medical Image Computing and Computer-Assisted Intervention–MICCAI 2015: 18th International Conference, Munich, Germany, October 5-9, 2015, Proceedings, Part III 18*, pp. 234–241, Springer, 2015.

[2] N. Zhu, D. Zhang, W. Wang, X. Li, B. Yang, J. Song, X. Zhao, B. Huang, W. Shi, R. Lu, *et al.*, "A novel coronavirus from patients with pneumonia in china, 2019," *New England journal of medicine*, 2020.

[3] M. Hoffmann, H. Kleine-Weber, S. Schroeder, N. Krüger, T. Herrler, S. Erichsen, T. S. Schiergens, G. Herrler, N.-H. Wu, A. Nitsche, *et al.*, "Sars-cov-2 cell entry depends on ace2 and tmprss2 and is blocked by a clinically proven protease inhibitor," *cell*, vol. 181, no. 2, pp. 271–280, 2020.

[4] I. Hamming, W. Timens, M. Bulthuis, A. Lely, G. v. Navis, and H. van Goor, "Tissue distribution of ace2 protein, the functional receptor for sars coronavirus. a first step in understanding sars pathogenesis," *The Journal of Pathology: A Journal of the Pathological Society of Great Britain and Ireland*, vol. 203, no. 2, pp. 631–637, 2004.

[5] H. P. Jia, D. C. Look, L. Shi, M. Hickey, L. Pewe, J. Netland, M. Farzan, C. Wohlford-Lenane, S. Perlman, and P. B. McCray Jr, "Ace2 receptor expression and severe acute respiratory syndrome coronavirus infection depend on differentiation of human airway epithelia," *Journal of virology*, vol. 79, no. 23, pp. 14614–14621, 2005.

[6] S. Badawi and B. R. Ali, "Ace2 nascence, trafficking, and sars-cov-2 pathogenesis: the saga continues," *Human genomics*, vol. 15, no. 1, pp. 1–14, 2021.

[7] I. T. Lee, T. Nakayama, C.-T. Wu, Y. Goltsev, S. Jiang, P. A. Gall, C.-K. Liao, L.-C. Shih, C. M. Schürch, D. R. McIlwain, *et al.*, "Ace2 localizes to the respiratory cilia and is not increased by ace inhibitors or arbs," *Nature communications*, vol. 11, no. 1, pp. 1–14, 2020.

[8] C.-T. Wu, P. V. Lidsky, Y. Xiao, R. Cheng, I. T. Lee, T. Nakayama, S. Jiang, W. He, J. Demeter, M. G. Knight, *et al.*, "Sars-cov-2 replication in airway epithelia requires motile cilia and microvillar reprogramming," *Cell*, 2022.

[9] C. Blume, C. L. Jackson, C. M. Spalluto, J. Legebeke, L. Nazlamova, F. Conforti, J.-M. Perotin, M. Frank, J. Butler, M. Crispin, *et al.*, "A novel ace2 isoform is expressed in human respiratory epithelia and is upregulated in response to interferons and rna respiratory virus infection," *Nature genetics*, vol. 53, no. 2, pp. 205–214, 2021.

[10] R. Robinot, M. Hubert, G. D. de Melo, F. Lazarini, T. Bruel, N. Smith, S. Levallois, F. Larrous, J. Fernandes, S. Gellenoncourt, *et al.*, "Sars-cov-2 infection induces the dedifferentiation of multiciliated cells and impairs mucociliary clearance," *Nature communications*, vol. 12, no. 1, pp. 1–16, 2021.

[11] L. Wang, C. Liu, B. Yang, H. Zhang, J. Jiao, R. Zhang, S. Liu, S. Xiao, Y. Chen, B. Liu, *et al.*, "Sars-cov-2 orf10 impairs cilia by enhancing cul2zyg11b activity," *Journal of Cell Biology*, vol. 221, no. 7, p. e202108015, 2022.

[12] X. M. Bustamante-Marin and L. E. Ostrowski, "Cilia and mucociliary clearance," *Cold Spring Harbor perspectives in biology*, vol. 9, no. 4, p. a028241, 2017.

[13] Z. Teff, Z. Priel, and L. A. Gheber, "Forces applied by cilia measured on explants from mucociliary tissue," *Biophysical journal*, vol. 92, no. 5, pp. 1813–1823, 2007.

[14] C. M. Smith, J. Djakow, R. C. Free, P. Djakow, R. Lonnen, G. Williams, P. Pohunek, R. A. Hirst, A. J. Easton, P. W. Andrew, *et al.*, "ciliafa: a research tool for automated, high-throughput measurement of ciliary beat frequency using freely available software," *Cilia*, vol. 1, no. 1, pp. 1–7, 2012.

[15] W. Kim, T. H. Han, H. J. Kim, M. Y. Park, K. S. Kim, and R. W. Park, "An automated measurement of ciliary beating frequency using a combined optical flow and peak detection," *Healthcare informatics research*, vol. 17, no. 2, pp. 111–119, 2011.

[16] J. N. Hansen, S. Rassmann, B. Stüven, N. Jurisch-Yaksi, and D. Wachten, "Ciliaq: a simple, open-source software for automated quantification of ciliary morphology and fluorescence in 2d, 3d, and 4d images," *The European Physical Journal E*, vol. 44, pp. 1–26, 2021.

[17] S. P. Quinn, M. J. Zahid, J. R. Durkin, R. J. Francis, C. W. Lo, and S. C. Chennubhotla, "Automated identification of abnormal respiratory ciliary motion in nasal biopsies," *Science translational medicine*, vol. 7, no. 299, pp. 299ra124–299ra124, 2015.

[18] M. Zain, S. Rao, N. Safir, Q. Wyner, I. Humphrey, A. Eldridge, C. Li, B. AlAila, and S. Quinn, "Towards an unsupervised spatiotemporal representation of cilia video using a modular generative pipeline," in *Proceedings of the Python in Science Conference*, 2020.

[19] C. Lu and S. Quinn, "Classification of ciliary motion with 3d convolutional neural networks," in *Proceedings of the SouthEast Conference*, pp. 235–238, 2017.

[20] A. Heurich, H. Hofmann-Winkler, S. Gierer, T. Liepold, O. Jahn, and S. Pöhlmann, "Tmprss2 and adam17 cleave ace2 differentially and only proteolysis by tmprss2 augments entry driven by the severe acute respiratory syndrome coronavirus spike protein," *Journal of virology*, vol. 88, no. 2, pp. 1293–1307, 2014.

[21] T. Nakayama, I. T. Lee, S. Jiang, M. S. Matter, C. H. Yan, J. B. Overdevest, C.-T. Wu, Y. Goltsev, L.-C. Shih, C.-K. Liao, *et al.*, "Determinants of sars-cov-2 entry and replication in airway mucosal tissue and susceptibility in smokers," *Cell Reports Medicine*, vol. 2, no. 10, p. 100421, 2021.

[22] H. P. Jia, D. C. Look, P. Tan, L. Shi, M. Hickey, L. Gakhar, M. C. Chappell, C. Wohlford-Lenane, and P. B. McCray Jr, "Ectodomain shedding of angiotensin converting enzyme 2 in human airway epithelia," *American Journal of Physiology-Lung Cellular and Molecular Physiology*, vol. 297, no. 1, pp. L84–L96, 2009.

[23] S. R. Tipnis, N. M. Hooper, R. Hyde, E. Karran, G. Christie, and A. J. Turner, "A human homolog of angiotensin-converting enzyme: cloning and functional expression as a captopril-insensitive carboxypeptidase," *Journal of Biological Chemistry*, vol. 275, no. 43, pp. 33238–33243, 2000.

[24] A. Marian, "The discovery of the ace2 gene," *Circulation research*, vol. 112, no. 10, pp. 1307–1309, 2013.

[25] M. A. Crackower, R. Sarao, G. Y. Oudit, C. Yagil, I. Kozieradzki, S. E. Scanga, A. J. Oliveira-dos Santos, J. da Costa, L. Zhang, Y. Pei, *et al.*, "Angiotensin-converting enzyme 2 is an essential regulator of heart function," *Nature*, vol. 417, no. 6891, pp. 822–828, 2002.

[26] Y. Li, W. Zhou, L. Yang, and R. You, "Physiological and pathological regulation of ace2, the sars-cov-2 receptor," *Pharmacological research*, vol. 157, p. 104833, 2020.

[27] D. W. Lambert, M. Yarski, F. J. Warner, P. Thornhill, E. T. Parkin, A. I. Smith, N. M. Hooper, and A. J. Turner, "Tumor necrosis factor-α convertase (adam17) mediates regulated ectodomain shedding of the severe-acute respiratory syndrome-coronavirus (sars-cov) receptor, angiotensin-converting enzyme-2 (ace2)," *Journal of Biological Chemistry*, vol. 280, no. 34, pp. 30113–30119, 2005.

[28] M. Iwata, J. E. Silva Enciso, and B. H. Greenberg, "Selective and specific regulation of ectodomain shedding of angiotensin-converting enzyme 2 by tumor necrosis factor α-converting enzyme," *American Journal of Physiology-Cell Physiology*, vol. 297, no. 5, pp. C1318–C1329, 2009.

[29] S. Matsuyama, N. Nagata, K. Shirato, M. Kawase, M. Takeda, and F. Taguchi, "Efficient activation of the severe acute respiratory syndrome coronavirus spike protein by the transmembrane protease tmprss2," *Journal of virology*, vol. 84, no. 24, pp. 12658–12664, 2010.

[30] M. I. Phillips and C. Sumners, "Angiotensin ii in central nervous system physiology.," *Regulatory peptides*, vol. 78, no. 1-3, pp. 1–11, 1998.

[31] M. I. Phillips and E. M. De Oliveira, "Brain renin angiotensin in disease," *Journal of molecular medicine*, vol. 86, pp. 715–722, 2008.

[32] E. SZCZEPAÑSKA-SADOWSKA, "Hypotensive function of the brain angiotensin-(1-7) in sprague dawley and renin transgenic rats," *Journal of physiology and pharmacology*, vol. 54, no. 3, pp. 371–381, 2003.

[33] C. Höcht, M. M. Gironacci, M. A. Mayer, M. Schuman, F. M. Bertera, and C. A. Taira, "Involvement of angiotensin-(1–7) in the hypothalamic hypotensive effect of captopril in sinoaortic denervated rats," *Regulatory peptides*, vol. 146, no. 1-3, pp. 58–66, 2008.

[34] S. B. Gurley, A. Allred, T. H. Le, R. Griffiths, L. Mao, N. Philip, T. A. Haystead, M. Donoghue, R. E. Breitbart, S. L. Acton, *et al.*, "Altered blood pressure responses and normal cardiac phenotype in ace2-null mice," *The Journal of clinical investigation*, vol. 116, no. 8, pp. 2218–2225, 2006.

[35] M. K. Raizada and A. J. Ferreira, "Ace2: a new target for cardiovascular disease therapeutics," *Journal of cardiovascular pharmacology*, vol. 50, no. 2, pp. 112–119, 2007.

[36] M. Donoghue, H. Wakimoto, C. T. Maguire, S. Acton, P. Hales, N. Stagliano, V. Fairchild-Huntress, J. Xu, J. N. Lorenz, V. Kadambi, *et al.*, "Heart block, ventricular tachycardia, and

sudden death in ace2 transgenic mice with downregulated connexins," *Journal of molecular and cellular cardiology*, vol. 35, no. 9, pp. 1043–1053, 2003.

[37] L. S. Zisman, R. S. Keller, B. Weaver, Q. Lin, R. Speth, M. R. Bristow, and C. C. Canver, "Increased angiotensin-(1-7)–forming activity in failing human heart ventricles: Evidence for upregulation of the angiotensin-converting enzyme homologue ace2," *Circulation*, vol. 108, no. 14, pp. 1707–1712, 2003.

[38] Y. Feng, H. Xia, R. A. Santos, R. Speth, and E. Lazartigues, "Angiotensin-converting enzyme 2: a new target for neurogenic hypertension," 2010.

[39] G. Y. Oudit, A. M. Herzenberg, Z. Kassiri, D. Wong, H. Reich, R. Khokha, M. A. Crackower, P. H. Backx, J. M. Penninger, and J. W. Scholey, "Loss of angiotensin-converting enzyme-2 leads to the late development of angiotensin ii-dependent glomerulosclerosis," *The American journal of pathology*, vol. 168, no. 6, pp. 1808–1820, 2006.

[40] D. W. Wong, G. Y. Oudit, H. Reich, Z. Kassiri, J. Zhou, Q. C. Liu, P. H. Backx, J. M. Penninger, A. M. Herzenberg, and J. W. Scholey, "Loss of angiotensin-converting enzyme-2 (ace2) accelerates diabetic kidney injury," *The American journal of pathology*, vol. 171, no. 2, pp. 438–451, 2007.

[41] J. Zhong, D. Guo, C. B. Chen, W. Wang, M. Schuster, H. Loibner, J. M. Penninger, J. W. Scholey, Z. Kassiri, and G. Y. Oudit, "Prevention of angiotensin ii–mediated renal oxidative stress, inflammation, and fibrosis by angiotensin-converting enzyme 2," *Hypertension*, vol. 57, no. 2, pp. 314–322, 2011.

[42] E. W. Sayers, J. Beck, E. E. Bolton, D. Bourexis, J. R. Brister, K. Canese, D. C. Comeau, K. Funk, S. Kim, W. Klimke, *et al.*, "Database resources of the national center for biotechnology information," *Nucleic acids research*, vol. 49, no. D1, p. D10, 2021.

[43] V. J. Manna, H. Choi, S. M. Rotoli, and S. J. Caradonna, "The dynamic nature of the coronavirus receptor, angiotensin-converting enzyme 2 (ace2) in differentiating airway epithelia," *Bba Advances*, vol. 2, p. 100044, 2022.

[44] M. Ye, J. Wysocki, P. Naaz, M. R. Salabat, M. S. LaPointe, and D. Batlle, "Increased ace 2 and decreased ace protein in renal tubules from diabetic mice: a renoprotective combination?," *Hypertension*, vol. 43, no. 5, pp. 1120–1125, 2004.

[45] N. Li, J. Zimpelmann, K. Cheng, J. A. Wilkins, and K. D. Burns, "The role of angiotensin converting enzyme 2 in the generation of angiotensin 1–7 by rat proximal tubules," *American Journal of Physiology-Renal Physiology*, vol. 288, no. 2, pp. F353–F362, 2005.

[46] D. Harmer, M. Gilbert, R. Borman, and K. L. Clark, "Quantitative mrna expression profiling of ace 2, a novel homologue of angiotensin converting enzyme," *FEBS letters*, vol. 532, no. 1-2, pp. 107–110, 2002.

[47] F. Hikmet, L. Méar, Å. Edvinsson, P. Micke, M. Uhlén, and C. Lindskog, "The protein expression profile of ace2 in human tissues," *Molecular systems biology*, vol. 16, no. 7, p. e9610, 2020.

[48] M. E. Ortiz, A. Thurman, A. A. Pezzulo, M. R. Leidinger, J. A. Klesney-Tait, P. H. Karp, P. Tan, C. Wohlford-Lenane, P. B. McCray, and D. K. Meyerholz, "Heterogeneous expression of the sars-coronavirus-2 receptor ace2 in the human respiratory tract," *EBioMedicine*, vol. 60, 2020.

[49] F. J. Warner, R. A. Lew, A. I. Smith, D. W. Lambert, N. M. Hooper, and A. J. Turner, "Angiotensin-converting enzyme 2 (ace2), but not ace, is preferentially localized to the apical surface of polarized kidney cells," *Journal of Biological Chemistry*, vol. 280, no. 47, pp. 39353–39362, 2005.

[50] Y. Wang, Y. Wang, W. Luo, L. Huang, J. Xiao, F. Li, S. Qin, X. Song, Y. Wu, Q. Zeng, *et al.*, "A comprehensive investigation of the mrna and protein level of ace2, the putative receptor of sars-cov-2, in human tissues and blood cells," *International journal of medical sciences*, vol. 17, no. 11, p. 1522, 2020.

[51] W. Sungnak, N. Huang, C. Bécavin, M. Berg, R. Queen, M. Litvinukova, C. Talavera-López, H. Maatz, D. Reichart, F. Sampaziotis, *et al.*, "Sars-cov-2 entry factors are highly expressed in nasal epithelial cells together with innate immune genes," *Nature medicine*, vol. 26, no. 5, pp. 681–687, 2020.

[52] J. H. Ahn, J. Kim, S. P. Hong, S. Y. Choi, M. J. Yang, Y. S. Ju, Y. T. Kim, H. M. Kim, M. T. Rahman, M. K. Chung, *et al.*, "Nasal ciliated cells are primary targets for sars-cov-2 replication in the early stage of covid-19," *The Journal of clinical investigation*, vol. 131, no. 13, 2021.

[53] A. L. Pinto, R. K. Rai, J. C. Brown, P. Griffin, J. R. Edgar, A. Shah, A. Singanayagam, C. Hogg, W. S. Barclay, C. E. Futter, *et al.*, "Ultrastructural insight into sars-cov-2 entry and budding in human airway epithelium," *Nature Communications*, vol. 13, no. 1, p. 1609, 2022.

[54] E. S. Brielle, D. Schneidman-Duhovny, and M. Linial, "The sars-cov-2 exerts a distinctive strategy for interacting with the ace2 human receptor," *Viruses*, vol. 12, no. 5, p. 497, 2020.

[55] Y. Imai, K. Kuba, and J. M. Penninger, "The discovery of angiotensin-converting enzyme 2 and its role in acute lung injury in mice," *Experimental physiology*, vol. 93, no. 5, pp. 543–548, 2008.

[56] L. Gutierrez-Chamorro, E. Riveira-Munoz, C. Barrios, V. Palau, M. Nevot, S. Pedreno-Lopez, J. Senserrich, M. Massanella, B. Clotet, C. Cabrera, *et al.*, "Sars-cov-2 infection modulates ace2 function and subsequent inflammatory responses in swabs and plasma of covid-19 patients," *Viruses*, vol. 13, no. 9, p. 1715, 2021.

[57] W. Ni, X. Yang, D. Yang, J. Bao, R. Li, Y. Xiao, C. Hou, H. Wang, J. Liu, D. Yang, *et al.*, "Role of angiotensin-converting enzyme 2 (ace2) in covid-19," *Critical Care*, vol. 24, no. 1, pp. 1–10, 2020.

[58] C. G. Ziegler, S. J. Allon, S. K. Nyquist, I. M. Mbano, V. N. Miao, C. N. Tzouanas, Y. Cao, A. S. Yousif, J. Bals, B. M. Hauser, *et al.*, "Sars-cov-2 receptor ace2 is an interferon-stimulated gene in human airway epithelial cells and is detected in specific cell subsets across tissues," *Cell*, vol. 181, no. 5, pp. 1016–1035, 2020.

[59] M.-W. Zhuang, Y. Cheng, J. Zhang, X.-M. Jiang, L. Wang, J. Deng, and P.-H. Wang, "Increasing host cellular receptor—angiotensin-converting enzyme 2 expression by coronavirus may facilitate 2019-ncov (or sars-cov-2) infection," *Journal of medical virology*, vol. 92, no. 11, pp. 2693–2701, 2020.

[60] M. L. Yeung, J. L. L. Teng, L. Jia, C. Zhang, C. Huang, J.-P. Cai, R. Zhou, K.-H. Chan, H. Zhao, L. Zhu, *et al.*, "Soluble ace2-mediated cell entry of sars-cov-2 via interaction with proteins related to the renin-angiotensin system," *Cell*, vol. 184, no. 8, pp. 2212–2228, 2021.

[61] H. Shuai, J. F.-W. Chan, T. T.-T. Yuen, C. Yoon, J.-C. Hu, L. Wen, B. Hu, D. Yang, Y. Wang, Y. Hou, *et al.*, "Emerging sars-cov-2 variants expand species tropism to murines," *EBioMedicine*, vol. 73, p. 103643, 2021.

[62] N. Zhu, W. Wang, Z. Liu, C. Liang, W. Wang, F. Ye, B. Huang, L. Zhao, H. Wang, W. Zhou, *et al.*, "Morphogenesis and cytopathic effect of sars-cov-2 infection in human airway epithelial cells," *Nature communications*, vol. 11, no. 1, pp. 1–8, 2020.

[63] B. N. Gomperts, L. J. Kim, S. A. Flaherty, and B. P. Hackett, "Il-13 regulates cilia loss and foxj1 expression in human airway epithelium," *American journal of respiratory cell and molecular biology*, vol. 37, no. 3, pp. 339–346, 2007.

[64] J. Hadjadj, N. Yatim, L. Barnabei, A. Corneau, J. Boussier, N. Smith, H. Péré, B. Charbit, V. Bondet, C. Chenevier-Gobeaux, *et al.*, "Impaired type i interferon activity and inflammatory responses in severe covid-19 patients," *Science*, vol. 369, no. 6504, pp. 718–724, 2020.

[65] C. Scagnolari, C. Bitossi, A. Viscido, F. Frasca, G. Oliveto, M. Scordio, L. Petrarca, E. Mancino, R. Nenna, E. Riva, *et al.*, "Ace2 expression is related to the interferon response in airway epithelial cells but is that functional for sars-cov-2 entry?," *Cytokine*, vol. 140, p. 155430, 2021.

[66] L. R. Bonser, W. L. Eckalbar, L. Rodriguez, J. Shen, K. D. Koh, K. Ghias, L. T. Zlock, S. Christenson, P. G. Woodruff, W. E. Finkbeiner, *et al.*, "The type 2 asthma mediator il-13 inhibits severe

acute respiratory syndrome coronavirus 2 infection of bronchial epithelium," *American Journal of Respiratory Cell and Molecular Biology*, vol. 66, no. 4, pp. 391–401, 2022.

[67] H. Kimura, D. Francisco, M. Conway, F. D. Martinez, D. Vercelli, F. Polverino, D. Billheimer, and M. Kraft, "Type 2 inflammation modulates ace2 and tmprss2 in airway epithelial cells," *Journal of Allergy and Clinical Immunology*, vol. 146, no. 1, pp. 80–88, 2020.

[68] Y. Imai, K. Kuba, S. Rao, Y. Huan, F. Guo, B. Guan, P. Yang, R. Sarao, T. Wada, H. Leong-Poi, *et al.*, "Angiotensin-converting enzyme 2 protects from severe acute lung failure," *Nature*, vol. 436, no. 7047, pp. 112–116, 2005.

[69] M. J. Huentelman, J. Zubcevic, J. A. Hernández Prada, X. Xiao, D. S. Dimitrov, M. K. Raizada, and D. A. Ostrov, "Structure-based discovery of a novel angiotensin-converting enzyme 2 inhibitor," *Hypertension*, vol. 44, no. 6, pp. 903–906, 2004.

[70] N. A. Dales, A. E. Gould, J. A. Brown, E. F. Calderwood, B. Guan, C. A. Minor, J. M. Gavin, P. Hales, V. K. Kaushik, M. Stewart, *et al.*, "Substrate-based design of the first class of angiotensin-converting enzyme-related carboxypeptidase (ace2) inhibitors," *Journal of the American Chemical Society*, vol. 124, no. 40, pp. 11852–11853, 2002.

[71] A. Berenyiova, I. Bernatova, A. Zemancikova, M. Drobna, M. Cebova, S. Golas, P. Balis, S. Liskova, Z. Valaskova, K. Krskova, *et al.*, "Vascular effects of low-dose ace2 inhibitor mln-4760—benefit or detriment in essential hypertension?," *Biomedicines*, vol. 10, no. 1, p. 38, 2021.

[72] C. M. Ferrario, J. Jessup, M. C. Chappell, D. B. Averill, K. B. Brosnihan, E. A. Tallant, D. I. Diz, and P. E. Gallagher, "Effect of angiotensin-converting enzyme inhibition and angiotensin ii receptor blockers on cardiac angiotensin-converting enzyme 2," *Circulation*, vol. 111, no. 20, pp. 2605–2610, 2005.

[73] J. Wysocki, E. Lores, M. Ye, M. J. Soler, and D. Batlle, "Kidney and lung ace2 expression after an ace inhibitor or an ang ii receptor blocker: implications for covid-19," *Journal of the American Society of Nephrology*, vol. 31, no. 9, pp. 1941–1943, 2020.

[74] M. Romaní-Pérez, V. Outeiriño-Iglesias, C. M. Moya, P. Santisteban, L. C. González-Matías, E. Vigo, and F. Mallo, "Activation of the glp-1 receptor by liraglutide increases ace2 expression, reversing right ventricle hypertrophy, and improving the production of sp-a and sp-b in the lungs of type 1 diabetes rats," *Endocrinology*, vol. 156, no. 10, pp. 3559–3569, 2015.

[75] F. Hildebrandt, T. Benzing, and N. Katsanis, "Ciliopathies," *New England Journal of Medicine*, vol. 364, no. 16, pp. 1533–1543, 2011.

[76] A. M. Waters and P. L. Beales, "Ciliopathies: an expanding disease spectrum," *Pediatric nephrology*, vol. 26, no. 7, pp. 1039–1056, 2011.

[77] D. J. McConnachie, J. L. Stow, and A. J. Mallett, "Ciliopathies and the kidney: a review," *American Journal of Kidney Diseases*, vol. 77, no. 3, pp. 410–419, 2021.

[78] M. W. Leigh, C. O'Callaghan, and M. R. Knowles, "The challenges of diagnosing primary ciliary dyskinesia," *Proceedings of the American Thoracic Society*, vol. 8, no. 5, pp. 434–437, 2011.

[79] M. A. Chilvers and C. O'Callaghan, "Analysis of ciliary beat pattern and beat frequency using digital high speed imaging: comparison with the photomultiplier and photodiode methods," *Thorax*, vol. 55, no. 4, pp. 314–317, 2000.

[80] M. A. Olm, J. E. Kögler Jr, M. Macchione, A. Shoemark, P. H. Saldiva, and J. C. Rodrigues, "Primary ciliary dyskinesia: evaluation using cilia beat frequency assessment via spectral analysis of digital microscopy images," *Journal of applied physiology*, vol. 111, no. 1, pp. 295–302, 2011.

[81] W. A. Stannard, M. A. Chilvers, A. R. Rutman, C. D. Williams, and C. O'Callaghan, "Diagnostic testing of patients suspected of primary ciliary dyskinesia," *American journal of respiratory and critical care medicine*, vol. 181, no. 4, pp. 307–314, 2010.

[82] K. K. Chu, C. Unglert, T. N. Ford, D. Cui, R. W. Carruth, K. Singh, L. Liu, S. E. Birket, G. M. Solomon, S. M. Rowe, *et al.*, "In vivo imaging of airway cilia and mucus clearance with micro-optical coherence tomography," *Biomedical optics express*, vol. 7, no. 7, pp. 2494–2505, 2016.

[83] Z. Carvalho-Santos, J. Azimzadeh, J. B. Pereira-Leal, and M. Bettencourt-Dias, "Evolution: Tracing the origins of centrioles, cilia, and flagella," *The Journal of cell biology*, vol. 194, no. 2, p. 165, 2011.

[84] C. Fisch and P. Dupuis-Williams, "Ultrastructure of cilia and flagella–back to the future!," *Biology of the Cell*, vol. 103, no. 6, pp. 249–270, 2011.

[85] A. Uzman, "Molecular cell biology -harvey lodish, arnold berk, s. lawrence zipursky, paul matsudaira, david baltimore and james darnell; freeman & co., new york, ny, 2000, 1084 pp., list price

102.25, isbn 0-7167-3136-3," *Biochemistry and Molecular Biology Education*, vol. 3, no. 29, pp. 126–128, 2001.

[86] C. Brokaw and R. Kamiya, "Bending patterns of chlamydomonas flagella: Iv. mutants with defects in inner and outer dynein arms indicate differences in dynein arm function," *Cell motility and the cytoskeleton*, vol. 8, no. 1, pp. 68–75, 1987.

[87] S. Huang, Y. Hirota, and K. Sawamoto, "Various facets of vertebrate cilia: motility, signaling, and role in adult neurogenesis," *Proceedings of the Japan Academy, Series B*, vol. 85, no. 8, pp. 324–336, 2009.

[88] H. M. Mitchison and E. M. Valente, "Motile and non-motile cilia in human pathology: From function to phenotypes," *The Journal of pathology*, vol. 241, no. 2, pp. 294–309, 2017.

[89] M. Fliegauf, T. Benzing, and H. Omran, "When cilia go bad: cilia defects and ciliopathies," *Nature reviews Molecular cell biology*, vol. 8, no. 11, pp. 880–893, 2007.

[90] A. G. Kramer-Zucker, F. Olale, C. J. Haycraft, B. K. Yoder, A. F. Schier, and I. A. Drummond, "Cilia-driven fluid flow in the zebrafish pronephros, brain and kupffer's vesicle is required for normal organogenesis," 2005.

[91] K. Shinohara, D. Chen, T. Nishida, K. Misaki, S. Yonemura, and H. Hamada, "Absence of radial spokes in mouse node cilia is required for rotational movement but confers ultrastructural instability as a trade-off," *Developmental cell*, vol. 35, no. 2, pp. 236–246, 2015.

[92] T. Kikuchi, T. Takasaka, A. Tonosaki, and H. Watanabe, "Fine structure of guinea pig vestibular kinocilium," *Acta oto-laryngologica*, vol. 108, no. 1-2, pp. 26–30, 1989.

[93] H. Sobkowicz, S. Slapnick, and B. August, "The kinocilium of auditory hair cells and evidence for its morphogenetic role during the regeneration of stereocilia and cuticular plates," *Journal of neurocytology*, vol. 24, pp. 633–653, 1995.

[94] S. C. Goetz and K. V. Anderson, "The primary cilium: a signalling centre during vertebrate development," *Nature Reviews Genetics*, vol. 11, no. 5, pp. 331–344, 2010.

[95] P. Jeffery and L. Reid, "New observations of rat airway epithelium: a quantitative and electron microscopic study.," *Journal of anatomy*, vol. 120, no. Pt 2, p. 295, 1975.

[96] M. Brightman and S. Palay, "The fine structure of ependyma in the brain of the rat," *The Journal of cell biology*, vol. 19, no. 2, pp. 415–439, 1963.

[97] E. R. Dirksen, "Centriole morphogenesis in developing ciliated epithelium of the mouse oviduct," *The Journal of cell biology*, vol. 51, no. 1, pp. 286–302, 1971.

[98] A. E. Tilley, M. S. Walters, R. Shaykhiev, and R. G. Crystal, "Cilia dysfunction in lung disease," *Annual review of physiology*, vol. 77, p. 379, 2015.

[99] M. Salathe, "Regulation of mammalian ciliary beating," *Annu. Rev. Physiol.*, vol. 69, pp. 401–422, 2007.

[100] N. Spassky and A. Meunier, "The development and functions of multiciliated epithelia," *Nature reviews Molecular cell biology*, vol. 18, no. 7, pp. 423–436, 2017.

[101] A. Wanner, M. Salathé, and T. G. O'Riordan, "Mucociliary clearance in the airways.," *American journal of respiratory and critical care medicine*, vol. 154, no. 6, pp. 1868–1902, 1996.

[102] M. R. Knowles, R. C. Boucher, *et al.*, "Mucus clearance as a primary innate defense mechanism for mammalian airways," *The Journal of clinical investigation*, vol. 109, no. 5, pp. 571–577, 2002.

[103] J. V. Fahy and B. F. Dickey, "Airway mucus function and dysfunction," *New England journal of medicine*, vol. 363, no. 23, pp. 2233–2247, 2010.

[104] M. Robinson and P. T. Bye, "Mucociliary clearance in cystic fibrosis," *Pediatric pulmonology*, vol. 33, no. 4, pp. 293–306, 2002.

[105] G. C. Smaldone, W. M. Foster, T. G. O'Riordan, M. S. Messina, R. J. Perry, and E. G. Langenback, "Regional impairment of mucociliary clearance in chronic obstructive pulmonary disease," *Chest*, vol. 103, no. 5, pp. 1390–1396, 1993.

[106] N. A. Cohen, "Sinonasal mucociliary clearance in health and disease," *Annals of Otology, Rhinology & Laryngology*, vol. 115, no. 9_suppl, pp. 20–26, 2006.

[107] J. Raidt, J. Wallmeier, R. Hjeij, J. G. Onnebrink, P. Pennekamp, N. T. Loges, H. Olbrich, K. Häffner, G. W. Dougherty, H. Omran, *et al.*, "Ciliary beat pattern and frequency in genetic variants of primary ciliary dyskinesia," *European Respiratory Journal*, vol. 44, no. 6, pp. 1579–1588, 2014.

[108] C. Li, *Cilia Segmentation Using U-Net with Gabor Filter*. PhD thesis, University of Georgia.

[109] A. Wang, Q. Zhang, Y. Han, S. Megason, S. Hormoz, K. R. Mosaliganti, J. C. Lam, and V. O. Li, "A novel deep learning-based 3d cell segmentation framework for future image-based disease detection," *Scientific Reports*, vol. 12, no. 1, pp. 1–15, 2022.

[110] C. Stringer, T. Wang, M. Michaelos, and M. Pachitariu, "Cellpose: a generalist algorithm for cellular segmentation," *Nature methods*, vol. 18, no. 1, pp. 100–106, 2021.

[111] M. C. Lauring, T. Zhu, W. Luo, W. Wu, F. Yu, and D. Toomre, "New software for automated cilia detection in cells (acdc)," *Cilia*, vol. 8, no. 1, pp. 1–21, 2019.

[112] C. Lu, M. Marx, M. Zahid, C. Lo, C. Chennubhotla, and S. P. Quinn, "Stacked neural networks for end-to-end ciliary motion analysis," *arXiv preprint arXiv:1803.07534*, 2018.

[113] M. Zain, E. Miller, S. Quinn, and C. Lo, "Low level feature extraction for cilia segmentation," in *Proceedings of the Python in Science Conference*, 2022.

[114] D. Gabor, "Theory of communication. part 1: The analysis of information," *Journal of the Institution of Electrical Engineers-part III: radio and communication engineering*, vol. 93, no. 26, pp. 429–441, 1946.

[115] N. Dalal and B. Triggs, "Histograms of oriented gradients for human detection," in *2005 IEEE computer society conference on computer vision and pattern recognition (CVPR'05)*, vol. 1, pp. 886–893, Ieee, 2005.

[116] D. G. Lowe, "Distinctive image features from scale-invariant keypoints," *International journal of computer vision*, vol. 60, pp. 91–110, 2004.

[117] P. Zhang, A. A. Kiseleva, V. Korobeynikov, H. Liu, M. B. Einarson, and E. A. Golemis, "Microscopy-based automated live cell screening for small molecules that affect ciliation," *Frontiers in genetics*, vol. 10, p. 75, 2019.

[118] V. Tadic, T. Loncar-Turukalo, A. Odry, Z. Trpovski, A. Toth, Z. Vizvari, and P. Odry, "A note on advantages of the fuzzy gabor filter in object and text detection," *Symmetry*, vol. 13, no. 4, p. 678, 2021.

[119] N. Nguyen-Thanh, T. Pham, and K. Ichikawa, "Automated detection and segmentation of mitochondrial images based on gradient enhancement and adaptive gabor filter," 2019.

[120] U. Schmidt, M. Weigert, C. Broaddus, and G. Myers, "Cell detection with star-convex polygons. medical image computing and computer assisted intervention—miccai 2018. 2018," 1806.

[121] A. Wolny, L. Cerrone, A. Vijayan, R. Tofanelli, A. V. Barro, M. Louveaux, C. Wenzl, S. Strauss, D. Wilson-Sánchez, R. Lymbouridou, *et al.*, "Accurate and versatile 3d segmentation of plant tissues at cellular resolution," *Elife*, vol. 9, p. e57613, 2020.

[122] M. Arzt, J. Deschamps, C. Schmied, T. Pietzsch, D. Schmidt, P. Tomancak, R. Haase, and F. Jug, "Labkit: labeling and segmentation toolkit for big image data," *Frontiers in computer science*, p. 10, 2022.

[123] J. Long, E. Shelhamer, and T. Darrell, "Fully convolutional networks for semantic segmentation," in *Proceedings of the IEEE conference on computer vision and pattern recognition*, pp. 3431–3440, 2015.

[124] S. Ram, M. S. Majdi, J. J. Rodríguez, Y. Gao, and H. L. Brooks, "Classification of primary cilia in microscopy images using convolutional neural random forests," in *2018 IEEE Southwest Symposium on Image Analysis and Interpretation (SSIAI)*, pp. 89–92, IEEE, 2018.

[125] A. Gupta, A. Suveer, J. Lindblad, A. Dragomir, I.-M. Sintorn, and N. Sladoje, "False positive reduction of cilia detected in low resolution tem images using a convolutional neural network," in *SWEDISH SYMPOSIUM ON IMAGE ANALYSIS 2017 (SSBA), 13-15 March 2017, Linköping, Sweden*, Swedish Society for Automated Image Analysis, 2017.

[126] M. Pachitariu and C. Stringer, "Cellpose 2.0: how to train your own model," *Nature Methods*, pp. 1–8, 2022.

[127] S. Luan, C. Chen, B. Zhang, J. Han, and J. Liu, "Gabor convolutional networks," *IEEE Transactions on Image Processing*, vol. 27, no. 9, pp. 4357–4366, 2018.

[128] A. A. Reyes, S. Paheding, M. Deo, and M. Audette, "Gabor filter-embedded u-net with transformer-based encoding for biomedical image segmentation," in *Multiscale Multimodal Medical Imaging: Third International Workshop, MMMI 2022, Held in Conjunction with MICCAI 2022, Singapore, September 22, 2022, Proceedings*, pp. 76–88, Springer, 2022.

[129] C. E. Kuehni and J. S. Lucas, "Diagnosis of primary ciliary dyskinesia: summary of the ers task force report," *Breathe*, vol. 13, no. 3, pp. 166–178, 2017.

[130] A. J. Shapiro, S. D. Davis, D. Polineni, M. Manion, M. Rosenfeld, S. D. Dell, M. A. Chilvers, T. W. Ferkol, M. A. Zariwala, S. D. Sagel, *et al.*, "Diagnosis of primary ciliary dyskinesia. an official american thoracic society clinical practice guideline," *American journal of respiratory and critical care medicine*, vol. 197, no. 12, pp. e24–e39, 2018.

[131] A. L. Oldenburg, R. K. Chhetri, D. B. Hill, and B. Button, "Monitoring airway mucus flow and ciliary activity with optical coherence tomography," *Biomedical optics express*, vol. 3, no. 9, pp. 1978–1992, 2012.

[132] X. Shi, G. Garcia III, J. C. Van De Weghe, R. McGorty, G. J. Pazour, D. Doherty, B. Huang, and J. F. Reiter, "Super-resolution microscopy reveals that disruption of ciliary transition-zone architecture causes joubert syndrome," *Nature cell biology*, vol. 19, no. 10, pp. 1178–1188, 2017.

[133] V. Mennella, B. Keszthelyi, K. McDonald, B. Chhun, F. Kan, G. C. Rogers, B. Huang, and D. Agard, "Subdiffraction-resolution fluorescence microscopy reveals a domain of the centrosome critical for pericentriolar material organization," *Nature cell biology*, vol. 14, no. 11, pp. 1159–1168, 2012.

[134] Y. Katoh, S. Chiba, and K. Nakayama, "Practical method for superresolution imaging of primary cilia and centrioles by expansion microscopy using an amplibody for fluorescence signal amplification," *Molecular biology of the cell*, vol. 31, no. 20, pp. 2195–2206, 2020.

[135] J. Papon, A. Coste, F. Roudot-Thoraval, M. Boucherat, G. Roger, A. Tamalet, A. Vojtek, S. Amselem, and E. Escudier, "A 20-year experience of electron microscopy in the diagnosis of primary ciliary dyskinesia," *European Respiratory Journal*, vol. 35, no. 5, pp. 1057–1063, 2010.

[136] T. Burgoyne, M. Dixon, P. Luther, C. Hogg, and A. Shoemark, "Generation of a three-dimensional ultrastructural model of human respiratory cilia," *American journal of respiratory cell and molecular biology*, vol. 47, no. 6, pp. 800–806, 2012.

[137] M. Ma, M. Stoyanova, G. Rademacher, S. K. Dutcher, A. Brown, and R. Zhang, "Structure of the decorated ciliary doublet microtubule," *Cell*, vol. 179, no. 4, pp. 909–922, 2019.

[138] M. Gui, H. Farley, P. Anujan, J. R. Anderson, D. W. Maxwell, J. B. Whitchurch, J. J. Botsch, T. Qiu, S. Meleppattu, S. K. Singh, *et al.*, "De novo identification of mammalian ciliary motility proteins using cryo-em," *Cell*, vol. 184, no. 23, pp. 5791–5806, 2021.

[139] J. Lin, W. Yin, M. C. Smith, K. Song, M. W. Leigh, M. A. Zariwala, M. R. Knowles, L. E. Ostrowski, and D. Nicastro, "Cryo-electron tomography reveals ciliary defects underlying human rsph1 primary ciliary dyskinesia," *Nature communications*, vol. 5, no. 1, p. 5727, 2014.

[140] M. A. Jordan, D. R. Diener, L. Stepanek, and G. Pigino, "The cryo-em structure of intraflagellar transport trains reveals how dynein is inactivated to ensure unidirectional anterograde movement in cilia," *Nature cell biology*, vol. 20, no. 11, pp. 1250–1255, 2018.

[141] J. Lin and D. Nicastro, "Asymmetric distribution and spatial switching of dynein activity generates ciliary motility," *Science*, vol. 360, no. 6387, p. eaar1968, 2018.

[142] P. Kiesel, G. Alvarez Viar, N. Tsoy, R. Maraspini, P. Gorilak, V. Varga, A. Honigmann, and G. Pigino, "The molecular structure of mammalian primary cilia revealed by cryo-electron tomography," *Nature structural & molecular biology*, vol. 27, no. 12, pp. 1115–1124, 2020.

[143] M. R. Knowles, M. Zariwala, and M. Leigh, "Primary ciliary dyskinesia," *Clinics in chest medicine*, vol. 37, no. 3, pp. 449–461, 2016.

[144] B. Rubbo, A. Shoemark, C. L. Jackson, R. Hirst, J. Thompson, J. Hayes, E. Frost, F. Copeland, C. Hogg, C. O'Callaghan, *et al.*, "Accuracy of high-speed video analysis to diagnose primary ciliary dyskinesia," *Chest*, vol. 155, no. 5, pp. 1008–1017, 2019.

[145] J. G. Fujimoto, C. Pitris, S. A. Boppart, and M. E. Brezinski, "Optical coherence tomography: an emerging technology for biomedical imaging and optical biopsy," *Neoplasia*, vol. 2, no. 1-2, pp. 9–25, 2000.

[146] S. Wang, J. C. Burton, R. R. Behringer, and I. V. Larina, "In vivo micro-scale tomography of ciliary behavior in the mammalian oviduct," *Scientific Reports*, vol. 5, no. 1, pp. 1–11, 2015.

[147] G. M. Solomon, R. Francis, K. K. Chu, S. E. Birket, G. Gabriel, J. E. Trombley, K. L. Lemke, N. Klena, B. Turner, G. J. Tearney, *et al.*, "Assessment of ciliary phenotype in primary ciliary dyskinesia by micro-optical coherence tomography," *JCI insight*, vol. 2, no. 5, 2017.

[148] D. Cui, K. K. Chu, B. Yin, T. N. Ford, C. Hyun, H. M. Leung, J. A. Gardecki, G. M. Solomon, S. E. Birket, L. Liu, *et al.*, "Flexible, high-resolution micro-optical coherence tomography endobronchial probe toward in vivo imaging of cilia," *Optics letters*, vol. 42, no. 4, pp. 867–870, 2017.

[149] B. T. Lemieux, J. J. Chen, J. Jing, Z. Chen, and B. J. Wong, "Measurement of ciliary beat frequency using doppler optical coherence tomography," in *International forum of allergy & rhinology*, vol. 5, pp. 1048–1054, Wiley Online Library, 2015.

[150] J. C. Jing, J. J. Chen, L. Chou, B. J. Wong, and Z. Chen, "Visualization and detection of ciliary beating pattern and frequency in the upper airway using phase resolved doppler optical coherence tomography," *Scientific reports*, vol. 7, no. 1, p. 8522, 2017.

[151] L. Liu, K. K. Chu, G. H. Houser, B. J. Diephuis, Y. Li, E. J. Wilsterman, S. Shastry, G. Dierksen, S. E. Birket, M. Mazur, *et al.*, "Method for quantitative study of airway functional microanatomy using micro-optical coherence tomography," *PloS one*, vol. 8, no. 1, p. e54473, 2013.

[152] K. E. Tipirneni, J. W. Grayson, S. Zhang, D.-Y. Cho, D. F. Skinner, D.-J. Lim, C. Mackey, G. J. Tearney, S. M. Rowe, and B. A. Woodworth, "Assessment of acquired mucociliary clearance defects using micro-optical coherence tomography," in *International forum of allergy & rhinology*, vol. 7, pp. 920–925, Wiley Online Library, 2017.

[153] Y. He, Y. Qu, J. C. Jing, and Z. Chen, "Characterization of oviduct ciliary beat frequency using real time phase resolved doppler spectrally encoded interferometric microscopy," *Biomedical Optics Express*, vol. 10, no. 11, pp. 5650–5659, 2019.

[154] T. Kohlfaerber, M. Pieper, M. Münter, C. Holzhausen, M. Ahrens, C. Idel, K.-L. Bruchhage, A. Leichtle, P. König, G. Hüttmann, *et al.*, "Dynamic microscopic optical coherence tomography to visualize the morphological and functional micro-anatomy of the airways," *Biomedical Optics Express*, vol. 13, no. 6, pp. 3211–3223, 2022.

[155] L. Gheber and Z. Priel, "Extraction of cilium beat parameters by the combined application of photoelectric measurements and computer simulation," *Biophysical journal*, vol. 72, no. 1, pp. 449–462, 1997.

[156] A. Oltean, A. J. Schaffer, P. V. Bayly, and S. L. Brody, "Quantifying ciliary dynamics during assembly reveals stepwise waveform maturation in airway cells," *American journal of respiratory cell and molecular biology*, vol. 59, no. 4, pp. 511–522, 2018.

[157] M. Bottier, K. A. Thomas, S. K. Dutcher, and P. V. Bayly, "How does cilium length affect beating?," *Biophysical journal*, vol. 116, no. 7, pp. 1292–1304, 2019.

[158] B. Button, R. C. Boucher, U. of North Carolina Virtual Lung Group, *et al.*, "Role of mechanical stress in regulating airway surface hydration and mucus clearance rates," *Respiratory physiology & neurobiology*, vol. 163, no. 1-3, pp. 189–201, 2008.

[159] B. Button, S. F. Okada, C. B. Frederick, W. R. Thelin, and R. C. Boucher, "Mechanosensitive atp release maintains proper mucus hydration of airways," *Science signaling*, vol. 6, no. 279, pp. ra46–ra46, 2013.

[160] K. Droguett, M. Rios, D. V. Carreño, C. Navarrete, C. Fuentes, M. Villalón, and N. P. Barrera, "An autocrine atp release mechanism regulates basal ciliary activity in airway epithelium," *The Journal of physiology*, vol. 595, no. 14, pp. 4755–4767, 2017.

[161] J. Gray, "The mechanism of ciliary movement.—vi. photographic and stroboscopic analysis of ciliary movement," *Proceedings of the Royal Society of London. Series B, Containing Papers of a Biological Character*, vol. 107, no. 751, pp. 313–332, 1930.

[162] S. A. Baba and Y. Hiramoto, "A quantitative analysis of ciliary movement by means of high-speed microcinematography," *Journal of Experimental Biology*, vol. 52, no. 3, pp. 675–690, 1970.

[163] M. Bottier, S. Blanchon, G. Pelle, E. Bequignon, D. Isabey, A. Coste, E. Escudier, J. B. Grotberg, J.-F. Papon, M. Filoche, *et al.*, "A new index for characterizing micro-bead motion in a flow induced by ciliary beating: Part i, experimental analysis," *PLoS computational biology*, vol. 13, no. 7, p. e1005605, 2017.

[164] A. D. Workman and N. A. Cohen, "The effect of drugs and other compounds on the ciliary beat frequency of human respiratory epithelium," *American journal of rhinology & allergy*, vol. 28, no. 6, pp. 454–464, 2014.

[165] R. Doyle, T. Moninger, N. Debavalya, and W. Hsu, "Use of confocal linescan to document ciliary beat frequency," *Journal of microscopy*, vol. 223, no. 2, pp. 159–164, 2006.

[166] O. Meste, F. Brau, and A. Guyon, "Robust estimation of the motile cilia beating frequency," *Medical & biological engineering & computing*, vol. 53, pp. 1025–1035, 2015.

[167] E. Puybareau, H. Talbot, G. Pelle, B. Louis, J.-F. Papon, A. Coste, and L. Najman, "A regionalized automated measurement of ciliary beating frequency," in *2015 IEEE 12th International Symposium on Biomedical Imaging (ISBI)*, pp. 528–531, IEEE, 2015.

[168] T. Straßer, S. Wagner, and E. Zrenner, "Review of the application of the open-source software ciloct for semi-automatic segmentation and analysis of the ciliary muscle in oct images," *PLoS One*, vol. 15, no. 6, p. e0234330, 2020.

[169] P. Sampaio, M. F. da Silva, I. Vale, M. Roxo-Rosa, A. Pinto, C. Constant, L. Pereira, C. M. Quintão, and S. S. Lopes, "Ciliarmove: new software for evaluating ciliary beat frequency helps find novel mutations by a portuguese multidisciplinary team on primary ciliary dyskinesia," *ERJ open research*, vol. 7, no. 1, 2021.

[170] O. Meste, F. Brau, and A. Guyon, "A new method for the robust estimation of the motile cilia beating frequency," 2013.

[171] J. J. Chen, B. T. Lemieux, and B. J. Wong, "A low-cost method of ciliary beat frequency measurement using iphone and matlab: rabbit study," *Otolaryngology–Head and Neck Surgery*, vol. 155, no. 2, pp. 252–256, 2016.

[172] Y. Okada, S. Takeda, Y. Tanaka, J.-C. I. Belmonte, and N. Hirokawa, "Mechanism of nodal flow: a conserved symmetry breaking event in left-right axis determination," *Cell*, vol. 121, no. 4, pp. 633–644, 2005.

[173] N. Hirokawa, Y. Tanaka, Y. Okada, and S. Takeda, "Nodal flow and the generation of left-right asymmetry," *Cell*, vol. 125, no. 1, pp. 33–45, 2006.

[174] M. A. Chilvers, A. Rutman, and C. O'Callaghan, "Ciliary beat pattern is associated with specific ultrastructural defects in primary ciliary dyskinesia," *Journal of Allergy and Clinical Immunology*, vol. 112, no. 3, pp. 518–524, 2003.

[175] M. Chilvers, A. Rutman, and C. O'Callaghan, "Functional analysis of cilia and ciliated epithelial ultrastructure in healthy children and young adults," *Thorax*, vol. 58, no. 4, pp. 333–338, 2003.

[176] B. Thomas, A. Rutman, and C. O'Callaghan, "Disrupted ciliated epithelium shows slower ciliary beat frequency and increased dyskinesia," *European Respiratory Journal*, vol. 34, no. 2, pp. 401–404, 2009.

[177] A. Reula, J. Pitarch-Fabregat, J. Milara, J. Cortijo, M. Mata-Roig, L. Milian, and M. Armengot, "High-speed video microscopy for primary ciliary dyskinesia diagnosis: A study of ciliary motility variations with time and temperature," *Diagnostics*, vol. 11, no. 7, p. 1301, 2021.

[178] J.-F. Papon, L. Bassinet, G. Cariou-Patron, F. Zerah-Lancner, A.-M. Vojtek, S. Blanchon, B. Crestani, S. Amselem, A. Coste, B. Housset, *et al.*, "Quantitative analysis of ciliary beating in primary ciliary dyskinesia: a pilot study," *Orphanet journal of rare diseases*, vol. 7, pp. 1–11, 2012.

[179] A. Nandagiri, A. S. Gaikwad, D. L. Potter, R. Nosrati, J. Soria, M. K. O'Bryan, S. Jadhav, and R. Prabhakar, "Flagellar energetics from high-resolution imaging of beating patterns in tethered mouse sperm," *Elife*, vol. 10, p. e62524, 2021.

[180] M. Chioccioli, L. Feriani, Q. Nguyen, J. Kotar, S. Dell, V. Mennella, I. Amirav, and P. Cicuta, "A how-to guide to: Quantitative high-speed video profiling to discriminate between variants of primary ciliary dyskinesia," *bioRxiv*, p. 614966, 2019.

[181] K. S. Wilson, O. Gonzalez, S. K. Dutcher, and P. V. Bayly, "Dynein-deficient flagella respond to increased viscosity with contrasting changes in power and recovery strokes," *Cytoskeleton*, vol. 72, no. 9, pp. 477–490, 2015.

[182] P. Bayly, B. Lewis, P. Kemp, R. Pless, and S. Dutcher, "Efficient spatiotemporal analysis of the flagellar waveform of chlamydomonas reinhardtii," *Cytoskeleton*, vol. 67, no. 1, pp. 56–69, 2010.

[183] D. R. Brumley, K. Y. Wan, M. Polin, and R. E. Goldstein, "Flagellar synchronization through direct hydrodynamic interactions," *elife*, vol. 3, p. e02750, 2014.

[184] M. Chilvers and C. O'callaghan, "Local mucociliary defence mechanisms," *Paediatric respiratory reviews*, vol. 1, no. 1, pp. 27–34, 2000.

[185] L. M. Kuyper, P. D. Paré, J. C. Hogg, R. K. Lambert, D. Ionescu, R. Woods, and T. R. Bai, "Characterization of airway plugging in fatal asthma," *The American journal of medicine*, vol. 115, no. 1, pp. 6–11, 2003.

[186] W. D. Bennett, B. L. Laube, T. Corcoran, K. Zeman, G. Sharpless, K. Thomas, J. Wu, P. J. Mogayzel Jr, J. Pilewski, and S. Donaldson, "Multisite comparison of mucociliary and cough clearance measures using standardized methods," *Journal of aerosol medicine and pulmonary drug delivery*, vol. 26, no. 3, pp. 157–164, 2013.

[187] R. Francis and C. Lo, "Ex vivo method for high resolution imaging of cilia motility in rodent airway epithelia," *JoVE (Journal of Visualized Experiments)*, no. 78, p. e50343, 2013.

[188] B. R. Grubb, A. Livraghi-Butrico, T. D. Rogers, W. Yin, B. Button, and L. E. Ostrowski, "Reduced mucociliary clearance in old mice is associated with a decrease in muc5b mucin," *American Journal of Physiology-Lung Cellular and Molecular Physiology*, vol. 310, no. 9, pp. L860–L867, 2016.

[189] A. Dummer, C. Poelma, M. C. DeRuiter, M.-J. T. Goumans, and B. P. Hierck, "Measuring the primary cilium length: improved method for unbiased high-throughput analysis," *Cilia*, vol. 5, no. 1, pp. 1–9, 2016.

[190] W. Wang, B. M. Jack, H. H. Wang, M. A. Kavanaugh, R. L. Maser, and P. V. Tran, "Intraflagellar transport proteins as regulators of primary cilia length," *Frontiers in Cell and Developmental Biology*, vol. 9, p. 661350, 2021.

[191] K. Miyoshi, K. Kasahara, I. Miyazaki, and M. Asanuma, "Factors that influence primary cilium length," *Acta Medica Okayama*, vol. 65, no. 5, pp. 279–285, 2011.

[192] D. Jin, T. T. Ni, J. Sun, H. Wan, J. D. Amack, G. Yu, J. Fleming, C. Chiang, W. Li, A. Papierniak, *et al.*, "Prostaglandin signalling regulates ciliogenesis by modulating intraflagellar transport," *Nature cell biology*, vol. 16, no. 9, pp. 841–851, 2014.

[193] E. Verghese, J. Zhuang, D. Saiti, S. D. Ricardo, and J. A. Deane, "In vitro investigation of renal epithelial injury suggests that primary cilium length is regulated by hypoxia-inducible mechanisms," *Cell biology international*, vol. 35, no. 9, pp. 909–913, 2011.

[194] P. L. Leopold, M. J. O'Mahony, X. J. Lian, A. E. Tilley, B.-G. Harvey, and R. G. Crystal, "Smoking is associated with shortened airway cilia," *PloS one*, vol. 4, no. 12, p. e8157, 2009.

[195] L. Rangel, M. Bernabé-Rubio, J. Fernández-Barrera, J. Casares-Arias, J. Millán, M. A. Alonso, and I. Correas, "Caveolin-1α regulates primary cilium length by controlling rhoa gtpase activity," *Scientific reports*, vol. 9, no. 1, pp. 1–16, 2019.

[196] R. T. Sherpa, A. M. Mohieldin, R. Pala, D. Wachten, R. S. Ostrom, and S. M. Nauli, "Sensory primary cilium is a responsive camp microdomain in renal epithelia," *Scientific Reports*, vol. 9, no. 1, pp. 1–16, 2019.

[197] P. Upadhyai, V. S. Guleria, and P. Udupa, "Characterization of primary cilia features reveal cell-type specific variability in in vitro models of osteogenic and chondrogenic differentiation," *PeerJ*, vol. 8, p. e9799, 2020.

[198] T. Saggese, A. A. Young, C. Huang, K. Braeckmans, and S. R. McGlashan, "Development of a method for the measurement of primary cilia length in 3d," *Cilia*, vol. 1, pp. 1–12, 2012.

[199] N. Pellicciotta, D. Das, J. Kotar, M. Faucourt, N. Spassky, E. Lauga, and P. Cicuta, "Cilia density and flow velocity affect alignment of motile cilia from brain cells," *Journal of Experimental Biology*, vol. 223, no. 24, p. jeb229310, 2020.

[200] M.-K. Khelloufi, E. Loiseau, M. Jaeger, N. Molinari, P. Chanez, D. Gras, and A. Viallat, "Spatiotemporal organization of cilia drives multiscale mucus swirls in model human bronchial epithelium," *Scientific reports*, vol. 8, no. 1, pp. 1–10, 2018.

[201] M. A. Sleigh, J. R. Blake, and N. Liron, "The propulsion of mucus by cilia," *American Review of Respiratory Disease*, vol. 137, no. 3, pp. 726–741, 1988.

[202] D. B. Hill, V. Swaminathan, A. Estes, J. Cribb, E. T. O'Brien, C. W. Davis, and R. Superfine, "Force generation and dynamics of individual cilia under external loading," *Biophysical journal*, vol. 98, no. 1, pp. 57–66, 2010.

[203] E. Loiseau, S. Gsell, A. Nommick, C. Jomard, D. Gras, P. Chanez, U. D'ortona, L. Kodjabachian, J. Favier, and A. Viallat, "Active mucus–cilia hydrodynamic coupling drives self-organization of human bronchial epithelium," *Nature Physics*, vol. 16, no. 11, pp. 1158–1164, 2020.

[204] R. R. Ferreira, A. Vilfan, F. Jülicher, W. Supatto, and J. Vermot, "Physical limits of flow sensing in the left-right organizer," *Elife*, vol. 6, p. e25078, 2017.

[205] R. Minkeviciene, I. Hlushchenko, A. Virenque, L. Lahti, P. Khanal, T. Rauramaa, A. Koistinen, V. Leinonen, F. M. Noe, and P. Hotulainen, "Mim-deficient mice exhibit anatomical changes in dendritic spines, cortex volume and brain ventricles, and functional changes in motor coordination and learning," *Frontiers in Molecular Neuroscience*, vol. 12, p. 276, 2019.

[206] E. Yusifov, A. Dumoulin, and E. T. Stoeckli, "Investigating primary cilia during peripheral nervous system formation," *International Journal of Molecular Sciences*, vol. 22, no. 6, p. 3176, 2021.

[207] V. Renò, M. Sciancalepore, G. Dimauro, R. Maglietta, M. Cassano, and M. Gelardi, "A novel approach for the automatic estimation of the ciliated cell beating frequency," *Electronics*, vol. 9, no. 6, p. 1002, 2020.

[208] C. Ringers, S. Bialonski, M. Ege, A. Solovev, J. N. Hansen, I. Jeong, B. M. Friedrich, and N. Jurisch-Yaksi, "Novel analytical tools reveal that local synchronization of cilia coincides with tissue-scale metachronal waves in zebrafish multiciliated epithelia," *Elife*, vol. 12, p. e77701, 2023.

[209] P. Cicuta, "The use of biophysical approaches to understand ciliary beating," *Biochemical Society Transactions*, vol. 48, no. 1, pp. 221–229, 2020.

[210] M. Chioccioli, L. Feriani, J. Kotar, P. Bratcher, and P. Cicuta, "Phenotyping ciliary dynamics and coordination in response to cftr-modulators in cystic fibrosis respiratory epithelial cells," *Nature communications*, vol. 10, no. 1, p. 1763, 2019.

[211] J. H. Sisson, J. Stoner, B. Ammons, and T. A. Wyatt, "All-digital image capture and whole-field analysis of ciliary beat frequency," *Journal of microscopy*, vol. 211, no. 2, pp. 103–111, 2003.

[212] M. Chioccioli, L. Feriani, Q. Nguyen, J. Kotar, S. D. Dell, V. Mennella, I. Amirav, and P. Cicuta, "Quantitative high-speed video profiling discriminates between dnah11 and hydin variants of primary ciliary dyskinesia," *American Journal of Respiratory and Critical Care Medicine*, vol. 199, no. 11, pp. 1436–1438, 2019.

[213] K. M. Trnh, M. T. Wayland, and S. Prabakaran, "Behavioural analysis of single-cell aneural ciliate, stentor roeseli, using machine," *Neural computation*, vol. 20, no. 3, pp. 709–737.

[214] Y. Almakady and S. Mahmoodi, "Texture-based region tracking using gaussian markov random fields for cilia motion analysis," in *2019 IEEE International Conference on Image Processing (ICIP)*, pp. 1292–1296, IEEE, 2019.

[215] W. Li, M. J. Moore, N. Vasilieva, J. Sui, S. K. Wong, M. A. Berne, M. Somasundaran, J. L. Sullivan, K. Luzuriaga, T. C. Greenough, *et al.*, "Angiotensin-converting enzyme 2 is a functional receptor for the sars coronavirus," *Nature*, vol. 426, no. 6965, pp. 450–454, 2003.

[216] P. Zhou, X.-L. Yang, X.-G. Wang, B. Hu, L. Zhang, W. Zhang, H.-R. Si, Y. Zhu, B. Li, C.-L. Huang, *et al.*, "A pneumonia outbreak associated with a new coronavirus of probable bat origin," *nature*, vol. 579, no. 7798, pp. 270–273, 2020.

[217] J. Lan, J. Ge, J. Yu, S. Shan, H. Zhou, S. Fan, Q. Zhang, X. Shi, Q. Wang, L. Zhang, *et al.*, "Structure of the sars-cov-2 spike receptor-binding domain bound to the ace2 receptor," *Nature*, vol. 581, no. 7807, pp. 215–220, 2020.

[218] R. A. S. Santos, W. O. Sampaio, A. C. Alzamora, D. Motta-Santos, N. Alenina, M. Bader, and M. J. Campagnole-Santos, "The ace2/angiotensin-(1–7)/mas axis of the renin-angiotensin system: focus on angiotensin-(1–7)," *Physiological reviews*, 2017.

[219] V. C. Cheng, S. K. Lau, P. C. Woo, and K. Y. Yuen, "Severe acute respiratory syndrome coronavirus as an agent of emerging and reemerging infection," *Clinical microbiology reviews*, vol. 20, no. 4, pp. 660–694, 2007.

[220] X. Zou, K. Chen, J. Zou, P. Han, J. Hao, and Z. Han, "Single-cell rna-seq data analysis on the receptor ace2 expression reveals the potential risk of different human organs vulnerable to 2019-ncov infection," *Frontiers of medicine*, vol. 14, no. 2, pp. 185–192, 2020.

[221] E. J. Sherman and B. T. Emmer, "Ace2 protein expression within isogenic cell lines is heterogeneous and associated with distinct transcriptomes," *Scientific reports*, vol. 11, no. 1, pp. 1–13, 2021.

[222] H. C. Lam, A. M. Choi, and S. W. Ryter, "Isolation of mouse respiratory epithelial cells and exposure to experimental cigarette smoke at air liquid interface," *JoVE (Journal of Visualized Experiments)*, no. 48, p. e2513, 2011.

[223] A. Horani, J. D. Dickinson, and S. L. Brody, "Applications of mouse airway epithelial cell culture for asthma research," in *Mouse Models of Allergic Disease*, pp. 91–107, Springer, 2013.

[224] S. Bertram, A. Heurich, H. Lavender, S. Gierer, S. Danisch, P. Perin, J. M. Lucas, P. S. Nelson, S. Pöhlmann, and E. J. Soilleux, "Influenza and sars-coronavirus activating proteases tmprss2 and

hat are expressed at multiple sites in human respiratory and gastrointestinal tracts," *PloS one*, vol. 7, no. 4, p. e35876, 2012.

[225] H. Limburg, A. Harbig, D. Bestle, D. A. Stein, H. M. Moulton, J. Jaeger, H. Janga, K. Hardes, J. Koepke, L. Schulte, *et al.*, "Tmprss2 is the major activating protease of influenza a virus in primary human airway cells and influenza b virus in human type ii pneumocytes," *Journal of virology*, vol. 93, no. 21, pp. e00649–19, 2019.

[226] G. Li, X. He, L. Zhang, Q. Ran, J. Wang, A. Xiong, D. Wu, F. Chen, J. Sun, and C. Chang, "Assessing ace2 expression patterns in lung tissues in the pathogenesis of covid-19," *Journal of autoimmunity*, vol. 112, p. 102463, 2020.

[227] N. Maksimowski, V. R. Williams, and J. W. Scholey, "Kidney ace2 expression: Implications for chronic kidney disease," *PLoS One*, vol. 15, no. 10, p. e0241534, 2020.

[228] V. S. Hernández, M. A. Zetter, E. C. Guerra, I. Hernández-Araiza, N. Karuzin, O. R. Hernández-Pérez, L. E. Eiden, and L. Zhang, "Ace2 expression in rat brain: Implications for covid-19 associated neurological manifestations," *Experimental Neurology*, vol. 345, p. 113837, 2021.

[229] J. E. Lee and J. G. Gleeson, "A systems-biology approach to understanding the ciliopathy disorders," *Genome medicine*, vol. 3, no. 9, pp. 1–9, 2011.

[230] B. A. Afzelius, "A human syndrome caused by immotile cilia," *Science*, vol. 193, no. 4250, pp. 317–319, 1976.

[231] T. Ferkol and M. W. Leigh, "Primary ciliary dyskinesia," in *Kendig's Disorders of the Respiratory Tract in Children*, pp. 1034–1043, Elsevier, 2019.

[232] M. Greenstone, A. Dewar, and P. Cole, "Ciliary dyskinesia with normal ultrastructure.," *Thorax*, vol. 38, no. 11, p. 875, 1983.

[233] M. R. Knowles, M. W. Leigh, J. L. Carson, S. D. Davis, S. D. Dell, T. W. Ferkol, K. N. Olivier, S. D. Sagel, M. Rosenfeld, K. A. Burns, *et al.*, "Mutations of dnahıı in patients with primary ciliary dyskinesia with normal ciliary ultrastructure," *Thorax*, vol. 67, no. 5, pp. 433–441, 2012.

[234] G. C. Schwabe, K. Hoffmann, N. T. Loges, D. Birker, C. Rossier, M. M. De Santi, H. Olbrich, M. Fliegauf, M. Failly, U. Liebers, *et al.*, "Primary ciliary dyskinesia associated with normal axoneme ultrastructure is caused by dnahıı mutations," *Human mutation*, vol. 29, no. 2, pp. 289–298, 2008.

[235] M. Pifferi, A. Michelucci, M. Conidi, A. Cangiotti, P. Simi, P. Macchia, and A. Boner, "New dnahıı mutations in primary ciliary dyskinesia with normal axonemal ultrastructure," *European Respiratory Journal*, vol. 35, no. 6, pp. 1413–1416, 2010.

[236] M. Joskova, J. Mokry, and S. Franova, "Respiratory cilia as a therapeutic target of phosphodiesterase inhibitors," *Frontiers in Pharmacology*, vol. 11, p. 609, 2020.

[237] C. Clary-Meinesz, J. Cosson, P. Huitorel, and B. Blaive, "Temperature effect on the ciliary beat frequency of human nasal and tracheal ciliated cells," *Biology of the Cell*, vol. 76, no. 3, pp. 335–338, 1992.

[238] L. Scopulovic, D. Francis, E. Pandzic, and R. Francis, "Quantifying cilia beat frequency using high-speed video microscopy: Assessing frame rate requirements when imaging different ciliated tissues," *Physiological Reports*, vol. 10, no. 11, p. e15349, 2022.

[239] C. O'Callaghan, K. Sikand, and M. A. Chilvers, "Analysis of ependymal ciliary beat pattern and beat frequency using high speed imaging: comparison with the photomultiplier and photodiode methods," *Cilia*, vol. 1, pp. 1–7, 2012.

[240] A. B. Christopher, S. Ochoa, E. Krushansky, R. Francis, X. Tian, M. Zahid, R. Muñoz, and C. W. Lo, "The effects of temperature and anesthetic agents on ciliary function in murine respiratory epithelia," *Frontiers in pediatrics*, vol. 2, p. 111, 2014.

[241] A. Green, L. Smallman, A. Logan, and A. Drake-Lee, "The effect of temperature on nasal ciliary beat frequency," *Clinical Otolaryngology & Allied Sciences*, vol. 20, no. 2, pp. 178–180, 1995.

[242] W. Nikolaizik, J. Hahn, M. Bauck, and S. Weber, "Comparison of ciliary beat frequencies at different temperatures in young adults," *ERJ Open Research*, vol. 6, no. 4, 2020.

[243] K. J. Ingels, M. R. Nijziel, K. Graamans, and E. H. Huizing, "Influence of cocaine and lidocaine on human nasal cilia: beat frequency and harmony in vitro," *Archives of Otolaryngology–Head & Neck Surgery*, vol. 120, no. 2, pp. 197–201, 1994.

[244] M. Katsumata, T. Fujisawa, Y. Kamiya, Y. Tanaka, C. Kamiya, Y. Inoue, H. Hozumi, M. Karayama, Y. Suzuki, K. Furuhashi, *et al.*, "Effects of long-acting muscarinic antagonists on promoting ciliary function in airway epithelium," *BMC Pulmonary Medicine*, vol. 22, no. 1, pp. 1–14, 2022.

[245] A. Korngreen and Z. Priel, "Purinergic stimulation of rabbit ciliated airway epithelia: control by multiple calcium sources.," *The Journal of Physiology*, vol. 497, no. 1, pp. 53–66, 1996.

[246] E. Hofer, A. Neher, A. Schrott-Fischer, and M. Nagl, "Influence of amphotericin b on the ciliary beat frequency of nasal mucosa," *The Laryngoscope*, vol. 114, no. 11, pp. 1964–1966, 2004.

[247] V. A. J. LUND, "Seasonal allergic rhinitis-a review of current therapy," *Allergy*, vol. 51, pp. 5–7, 1996.

[248] U. Achterrath-Tuckermann, V. Saano, E. Minker, F. Stroman, I. Arny, S. Joki, J. Nuutinen, and I. Szelenyi, "Influence of azelastine and some selected drugs on mucociliary clearance," *Lung*, vol. 170, pp. 201–209, 1992.

[249] J. Alberty and W. Stoll, "The effect of antiallergic intranasal formulations on ciliary beat frequency of human nasal epithelium in vitro," *Allergy*, vol. 53, no. 10, pp. 986–989, 1998.

[250] G. Di Benedetto, C. Magnus, P. Gray, and A. Mehta, "Calcium regulation of ciliary beat frequency in human respiratory epithelium in vitro.," *The Journal of Physiology*, vol. 439, no. 1, pp. 103–113, 1991.

[251] P. Satir, "Ionophore-mediated calcium entry induces mussel gill ciliary arrest," *Science*, vol. 190, no. 4214, pp. 586–588, 1975.

[252] G. Stafanger, H. Bisgaard, M. Pedersen, E. Mørkassel, and C. Koch, "Effect of n-acetylcysteine on the human nasal ciliary activity in vitro.," *European journal of respiratory diseases*, vol. 70, no. 3, pp. 157–162, 1987.

[253] P. Low, M. Dulfano, C. Luk, and P. Finch, "Effect of n-acetylcysteine on the ciliary beat frequency of human bronchial explants.," *Annals of allergy*, vol. 54, no. 4, pp. 273–275, 1985.

[254] Z. K. Gencer, L. Saydam, N. A. Cohen, and C. Cingi, "N-acetylcysteine effects on sinonasal cilia function," *ENT Updates*, vol. 5, no. 3, pp. 87–92, 2015.

[255] C. Shiima-Kinoshita, K.-Y. Min, T. Hanafusa, H. Mori, and T. Nakahari, "β2-adrenergic regulation of ciliary beat frequency in rat bronchiolar epithelium: potentiation by isosmotic cell shrinkage," *The Journal of physiology*, vol. 554, no. 2, pp. 403–416, 2004.

[256] C. P. Sodhi, J. Nguyen, Y. Yamaguchi, A. D. Werts, P. Lu, M. R. Ladd, W. B. Fulton, M. L. Kovler, S. Wang, T. Prindle, *et al.*, "A dynamic variation of pulmonary ace2 is required to modulate neutrophilic inflammation in response to pseudomonas aeruginosa lung infection in mice," *The Journal of Immunology*, vol. 203, no. 11, pp. 3000–3012, 2019.

[257] C. Kempeneers, C. Seaton, and M. A. Chilvers, "Variation of ciliary beat pattern in three different beating planes in healthy subjects," *Chest*, vol. 151, no. 5, pp. 993–1001, 2017.

[258] M. Chilvers, M. McKean, A. Rutman, B. Myint, M. Silverman, and C. O'Callaghan, "The effects of coronavirus on human nasal ciliated respiratory epithelium," *European Respiratory Journal*, vol. 18, no. 6, pp. 965–970, 2001.

[259] G. Di Benedetto, F. Manara-Shediac, and A. Mehta, "Inhibition of the cyclic amp-induced rise of ciliary activity by 1-(5-isoquinolinylsulphonyl)-2-methylpoperazine in human respiratory epithelium in vitro," *Journal of physiology*, vol. 426, 1990.

[260] C.-L. Chiu, N. Clack, *et al.*, "napari: a python multi-dimensional image viewer platform for the research community," *Microscopy and Microanalysis*, vol. 28, no. S1, pp. 1576–1577, 2022.

[261] N. Contributors, "napari: a multi-dimensional image viewer for python," *Zenodo https://doi.org/10.5281/zenodo*, vol. 3555620, 2019.

[262] C. O'Callaghan, M. Achaval, I. Forsythe, and P. W. Barry, "Brain and respiratory cilia: the effect of temperature," *Neonatology*, vol. 68, no. 6, pp. 394–397, 1995.

[263] T. Hayashi, M. Kawakami, S. Sasaki, T. Katsumata, H. Mori, H. Yoshida, and T. Nakahari, "Atp regulation of ciliary beat frequency in rat tracheal and distal airway epithelium," *Experimental physiology*, vol. 90, no. 4, pp. 535–544, 2005.

[264] J. Tamaoki, A. Chiyotani, N. Sakai, K. Takeyama, and K. Konno, "Effect of azelastine on sulphur dioxide induced impairment of ciliary motility in airway epithelium.," *Thorax*, vol. 48, no. 5, pp. 542–546, 1993.

[265] A. Schmid and M. Salathe, "Ciliary beat co-ordination by calcium," *Biology of the Cell*, vol. 103, no. 4, pp. 159–169, 2011.

[266] C. Sanchez-Cardenas, F. Montoya, F. Navarrete, A. Hernandez-Cruz, G. Corkidi, P. Visconti, and A. Darszon, "Intracellular ca2+ threshold reversibly switches flagellar beat off and on," *Biology of reproduction*, vol. 99, no. 5, pp. 1010–1021, 2018.

[267] P. Satir and M. A. Sleigh, "The physiology of cilia and mucociliary interactions," *Annual review of physiology*, vol. 52, no. 1, pp. 137–155, 1990.

[268] E. E. Davis, M. Brueckner, and N. Katsanis, "The emerging complexity of the vertebrate cilium: new functional roles for an ancient organelle," *Developmental cell*, vol. 11, no. 1, pp. 9–19, 2006.

[269] P. Delmotte and M. J. Sanderson, "Ciliary beat frequency is maintained at a maximal rate in the small airways of mouse lung slices," *American journal of respiratory cell and molecular biology*, vol. 35, no. 1, pp. 110–117, 2006.

[270] D. Häussler, J. Sommer, A. Nastev, C. Aderhold, A. Wenzel, B. Kramer, B. Stuck, and R. Birk, "Influence of mp 29-02 on ciliary beat frequency in human epithelial cells in vitro," *European Archives of Oto-Rhino-Laryngology*, vol. 275, no. 6, pp. 1483–1490, 2018.

[271] M. J. Sanderson and E. R. Dirksen, "Mechanosensitive and beta-adrenergic control of the ciliary beat frequency of mammalian respiratory tract cells in culture," *Am rev respir Dis*, vol. 139, no. 2, pp. 432–440, 1989.

[272] H. Tateno, D. Krapf, T. Hino, C. Sánchez-Cárdenas, A. Darszon, R. Yanagimachi, and P. E. Visconti, "Ca2+ ionophore a23187 can make mouse spermatozoa capable of fertilizing in vitro without activation of camp-dependent phosphorylation pathways," *Proceedings of the National Academy of Sciences*, vol. 110, no. 46, pp. 18543–18548, 2013.

[273] G. Stafanger, S. Garne, P. Howitz, E. Morkassel, and C. Koch, "The clinical effect and the effect on the ciliary motility of oral n-acetylcysteine in patients with cystic fibrosis and primary ciliary dyskinesia," *European Respiratory Journal*, vol. 1, no. 2, pp. 161–167, 1988.

[274] S.-L. Lee, C. O'Callaghan, Y.-L. Lau, and C.-W. D. Lee, "Functional analysis and evaluation of respiratory cilia in healthy chinese children," *Respiratory research*, vol. 21, no. 1, pp. 1–12, 2020.

[275] S. Blanchon, M. Legendre, M. Bottier, A. Tamalet, G. Montantin, N. Collot, C. Faucon, F. Dastot, B. Copin, A. Clement, *et al.*, "Deep phenotyping, including quantitative ciliary beating parameters, and extensive genotyping in primary ciliary dyskinesia," *Journal of medical genetics*, vol. 57, no. 4, pp. 237–244, 2020.

[276] A. M. Folcik, T. Haire, K. Cutshaw, M. Riddle, C. Shola, S. Nassani, P. Rice, B. Richardson, P. Shah, N. Nazamoddini-Kachouie, *et al.*, "Computer-assisted tracking of chlamydomonas species," *Frontiers in Plant Science*, vol. 10, p. 1616, 2020.

[277] M. T. Gallagher, G. Cupples, E. H. Ooi, J. Kirkman-Brown, and D. Smith, "Rapid sperm capture: high-throughput flagellar waveform analysis," *Human Reproduction*, vol. 34, no. 7, pp. 1173–1185, 2019.

[278] A. K. Jain and F. Farrokhnia, "Unsupervised texture segmentation using gabor filters," *Pattern recognition*, vol. 24, no. 12, pp. 1167–1186, 1991.

[279] X. Wang, X. Ding, and C. Liu, "Gabor filters-based feature extraction for character recognition," *Pattern recognition*, vol. 38, no. 3, pp. 369–379, 2005.

[280] W. K. Kong, D. Zhang, and W. Li, "Palmprint feature extraction using 2-d gabor filters," *Pattern recognition*, vol. 36, no. 10, pp. 2339–2347, 2003.

[281] E. Zalama, J. Gómez-García-Bermejo, R. Medina, and J. Llamas, "Road crack detection using visual features extracted by gabor filters," *Computer-Aided Civil and Infrastructure Engineering*, vol. 29, no. 5, pp. 342–358, 2014.

[282] M. Shahedi, A. Devi, J. Dormer, and B. Fei, "A study on u-net limitations in object localization and image segmentation," in *Society for Imaging Informatics in Medicine (SIIM), Virtual meeting*, 2020.

[283] V. Badrinarayanan, A. Kendall, and R. Cipolla, "Segnet: A deep convolutional encoder-decoder architecture for image segmentation," *IEEE transactions on pattern analysis and machine intelligence*, vol. 39, no. 12, pp. 2481–2495, 2017.

[284] K. He, G. Gkioxari, P. Dollár, and R. Girshick, "Mask r-cnn," in *Proceedings of the IEEE international conference on computer vision*, pp. 2961–2969, 2017.

[285] L.-C. Chen, G. Papandreou, I. Kokkinos, K. Murphy, and A. L. Yuille, "Deeplab: Semantic image segmentation with deep convolutional nets, atrous convolution, and fully connected crfs," *IEEE transactions on pattern analysis and machine intelligence*, vol. 40, no. 4, pp. 834–848, 2017.

[286] A. Kirillov, E. Mintun, N. Ravi, H. Mao, C. Rolland, L. Gustafson, T. Xiao, S. Whitehead, A. C. Berg, W.-Y. Lo, *et al.*, "Segment anything," *arXiv preprint arXiv:2304.02643*, 2023.

[287] Y. Amit and D. Geman, "Shape quantization and recognition with randomized trees," *Neural computation*, vol. 9, no. 7, pp. 1545–1588, 1997.